Lukas Köster

Application of a Novel Two-Stage Evaporator in Air-Conditioning Applications

Masteroppgave

NTNU
Norges teknisk-naturvitenskapelige universitet
Fakultet for ingeniørvitenskap
Institutt for energi- og prosessteknikk

NTNU
Kunnskap for en bedre verden

Lukas Köster

Application of a Novel Two-Stage Evaporator in Air-Conditioning Applications

NTNU
Kunnskap for en bedre verden

Abstract

The present work investigates the application of a novel two-stage evaporator in combination with an advanced hydronic sub-system to cover air conditioning demands. The proposed system architecture consists of the two-stage evaporator configuration implemented within a CO_2 heat pump, which is connected by a subsequent hydronic system to the air handling unit and thereby to the air volume. The hydronic system utilizes sensible and latent thermal energy storage by cold water storage and ice tanks. Due to the hydronic system architecture, the hydronic system can operate in 15 different operation modes, which are controlled by an adapted rule-based optimal control strategy. A model of the system is built in Modelica. Dynamic 24-h simulations are carried out to determine the system behaviour and performance characteristics. Based on exemplary data and component sizes, a load-shifting of 65% of the total on-peak load to off-peak periods could be achieved. Furthermore, the system achieved to limit the peak demand on the heat pump system and provides a basis for constant operating conditions of the heat pump during the on-peak period. The system setup has shown to provide great flexibility to adapt to specific applications and operating conditions. Additionally, preliminary experimental tests of the two-stage evaporator configuration are carried out.

Zusammenfassung

In der vorliegenden Arbeit wird die Anwendung eines neuartigen, zweistufigen Verdampfers in Kombination mit einem hydronischen Subsystem zur Deckung des Klimatisierungsbedarfs untersucht. Die Systemarchitektur besteht aus einer zweistufigen Verdampferkonfiguration, die in einer CO_2 -Wärmepumpe implementiert ist, welche über ein nachgeschaltetes Hydroniksystem mit dem Gebläsekonvektor und damit mit dem Luftvolumen verbunden ist. Das Hydroniksystem nutzt sensible und latente thermische Energiespeicher durch Kaltwasserspeicher und Eisspeicher. Aufgrund der Systemarchitektur kann das hydronische System in 15 verschiedenen Betriebsmodi arbeiten, die durch eine angepasste, regelbasierte Kontrollstrategie gesteuert werden. Ein Modell des Systems wurde in Modelica erstellt. Dynamische 24-Stunden-Simulationen wurden durchgeführt, um das Systemverhalten und die Leistungsmerkmale zu ermitteln. Basierend auf beispielhaften Daten und Komponentengrößen konnte eine Lastverschiebung von 65% des Bedarfs während Spitzenlastzeiten in Schwachlastzeiten erreicht werden. Darüber hinaus kann dass das System den Maximalbedarf der Wärmepumpenanlage begrenzen und eine Grundlage für konstante Betriebsbedingungen der Wärmepumpe während der Spitzenlastzeit schaffen. Der Systemaufbau bietet große Flexibilität zur Anpassung an die spezifischen Anwendungen und Betriebsbedingungen. Zusätzlich wurden erste experimentelle Tests der zweistufigen Verdampferkonfiguration durchgeführt.

Sammendrag

Det foreliggende arbeidet undersøker anvendelsen av en ny totrinns fordamper i kombinasjon med et avansert hydronisk delsystem for å dekke luftkondisjoneringsbehov. Den foreslåtte systemarkitekturen består av en totrinns fordamperkonfigurasjon implementert i en CO_2 varmepumpe, som er koblet med et påfølgende hydronisk system til luftbehandlingsenheten og dermed til luftvolumet. Det vannbårne systemet utnytter sensitiv og latent termisk energilagring ved hjelp av kaldtvannslagring og istanker. På grunn av den hydroniske systemarkitekturen kan det hydroniske systemet operere i 15 forskjellige driftsmoduser, som styres av en tilpasset regelbasert optimal kontrollstrategi. En modell av systemet er bygget i modelica. Dynamiske 24-timers simuleringer utføres for å bestemme systemets oppførsel og ytelsesegenskaper. Basert på eksemplariske data og komponentstørrelser kunne en lastforskyvning på 65 % av den totale toppbelastningen til lavlastperioder oppnås. Videre oppnådde systemet å begrense toppbelastningen på varmepumpesystemet og gir et grunnlag for konstante driftsforhold for varmepumpen i høylastperioden. Systemoppsettet har vist seg å gi stor fleksibilitet for å tilpasse seg de spesifikke bruksområdene og driftsbetingelsene. I tillegg er det utført innledende eksperimentelle tester av totrinns fordamperkonfigurasjonen.

Acknowledgements

Contents

Nomenclature

Latin Letters

Symbol	Explanation
A	Area [m^2]
c_p	Specific Heat Capacity [J kg^{-1} K^{-1}]
C_s	TES capacity [J]
d	Diameter [m]
g	Gravity constant 9.81 [m s^{-2}]
H	Height [m]
HX	Heat Exchanger
h	Specific Enthalpy [kJ kg^{-1}]
k	Thermal conductivity [W m^{-1} K^{-1}]
L	Length [m]
$\dot{m}$	Mass Flow [kg min^{-1}]
p	Pressure [Pa]
R	Reheating
T,t	Temperature [°C]
t	Thickness [m]
U	U-value [W m^{-2} K^{-1}]
V	Volume [m^3]
$\dot{V}$	Volume Flow [m^3 s^{-1}]
X	State of Charge of the Thermal Energy Storage [-]

Greek Letters

α	heat transfer coefficient
η_{ejec}	Ejector efficiency [-]
Π	Pressure ratio [-]
ρ	Density [kg m^{-3}]
$\dot{Q}$	Transferred Heat [kW]

Abbreviations

AC	Air Conditioning
CFC	Chlorofluorocarbons
COP	Coefficient of Performance [-]
CST	Cold Storage Tanks
DHW	Domestic Hot Water
ECR	Energy Cost Ratio
EFE	Ejector Fed Evaporator
ER	Entrainment Ratio of Ejector
GFE	Gravity Fed Evaporator

GHG	Greenhouse Gas
HSE	Health, Safety and Environment
IPCC	Intergovernmental Panel on Climate Change
IEA	International Energy Agency
KPI	Key Performance Indicators
R744	Carbon Dioxide
SH	Space Heating
SOC	State of Charge
SLHX	Suction Line Heat Exchanger
TES	Thermal Energy Storage
TSEV	Two-Stage Evaporator

Subscripts

a	approach
amb	ambient
bal	balance
$cool$	cooling
$crit$	critical point
dis	discharge, high pressure side
$evap$	evaporator
fus	fusion
in	inlet
l	liquid state
$lift$	lift by ejector
$LMTD$	Logarithmic mean temperature difference
m	mean
MF	ejector motive flow
MN	ejector motive nozzle
MP	Middle Plate
rec	(liquid) receiver
ris	riser diameter
SN	ejector suction nozzle
$trans$	transmission
$vent$	ventilation
w	water

List of Figures

List of Tables

1 Introduction

"Global warming, reaching 1.5°C in the near-term, would cause unavoidable increases in multiple climate hazards and present multiple risks to ecosystems and humans (very high confidence)." [1]

As the IPCC describes in the report *"Climate Change 2022: Impacts, Adaptation and Vulnerability"* [1], if the current trend in global warming continues, there will be an increase in environmental catastrophes and further irreversible changes [1]. Hence, actions to reduce GHG emissions and limit their impact onto the climate are required.

Dong et al. [2] reports that greenhouse gas emissions due to refrigeration and space cooling account for 10 % of the total GHG emissions [2]. This includes GHG emissions due to refrigerant leakages as well as due to energy consumption [2]. Furthermore, the emissions from space cooling are more than double of the emissions from refrigeration [2]. Within the space cooling sector, refrigerant leakage accounts to 30.7 % of the space cooling GHG emissions, and consequently accounts energy consumption to 69.7 % of the GHG emissions [2]. Hence, increasing the energy efficiency of space cooling systems can create significant contributions in the reduction of GHG emissions.

Nevertheless, the impact of refrigerant leakages should not be disregarded, as the publication by Dong et al. [2] shows. Hence, substituting synthetic refrigerants with a high global warming potential (GWP) with natural refrigerants with a low GWP decreases GHG emissions due to refrigerant leakages.

CO_2 is a natural refrigerant that features a global warming potential of $GWP = 1$ [3], low toxicity, and unique thermophysical properties [4]. CO_2 systems have already gained attention within *"vehicle air conditioning, building heating and hot water supply, drying industry, commercial cold chain, ice and snow sports and other cold and hot integrated supply fields."* [5]. The excellent heat transfer properties of CO_2 and the temperature glide during heat rejection makes CO_2 systems prone to be used within HVAC applications of buildings.

Therefore, the present work investigates an application of a two stage evaporator setup in a CO_2 heat pump into air conditioning applications. The system consists of an air handling unit, a CO_2 heat pump and a hydronic subsystem, which connects the CO_2 heat pump with the air handling unit. The hydronic system features sensible and latent thermal energy storage by cold water storage tanks and an ice tank. The proposed system design allows for flexibility within the operation of the thermal energy storage and a rule-

based controller to determine the operation strategy is integrated.

Besides the investigation of the two-stage evaporator application into air conditioning applications, preliminary experiments are carried out to assess the performance of the two-stage evaporator configuration within CO_2 systems.

1.1 Task Description

The task description of the master thesis reads as follows:

1. Literature review: Cold Thermal Energy Storage, ejectors, chiller systems, advanced CO2 heat pump systems

2. Develop a sustainable design for a CO2 heat pump and chiller system. Describe and develop the sub-systems for the energy distribution

3. Develop/apply an energy flow (hour by hour) simulation tool (Modelica) to evaluate the system. (Describe input parameter matrix for the evaluation tool)

4. Develop and perform experimental test campaign with various configurations in the laboratory

5. Master thesis should contain experimental and simulation results, as well as proposals for further work

6. Appendix: draft scientific paper of the main findings (10 pages)

1.2 Structure of the Thesis

The thesis contains the following structure:

Introduction: Introducing the aim and scope of the thesis. Parts of the introduction are, in accordance with the supervising professors, based and adapted from the previous project work.

Theory: Presenting relevant theory to the master thesis. The theory is, in accordance with the supervising professors, based and adapted from the previous project work.

System Design and Operation Modes: Description of the overall system design and its functionality. Furthermore, the general control of the system is presented.

Methodology: Within the chapter Methodology, the model created in Modelica is presented, with its sub-models, system hierarchy and information flows.

Preliminary System Results and System Optimization: The chapter presents results and discussions of the initial simulation. Furthermore, it presents improvements of the system based on the initial simulation and the evaluation of the im-

provements. The fusion of the different improvements results in the model for the concluding simulation.

Experimental Work: The chapter describes the experimental test setup located within the NTNU/SINTEF energy engineering laboratory.

Results: The results chapter presents the results obtained from the improved simulation and the preliminary, experimental work.

Discussion: The chapter includes the discussion of the gained results from the simulational and experimental work and develops ideas for further work.

Conclusion: The conclusion chapter provides a brief overview of the main findings of the thesis.

Further Work: The chapter further work presents the main work packages that should be continued.

2 Theory

The following chapter describes the underlying theory related to CO_2 as a refrigerant (chapter 2.1), selected CO_2 heat pump system configurations 2.2 and thermal energy storages within air conditioning applications (2.4).

2.1 Properties of CO2 as a Refrigerant

CO_2 has, compared to other refrigerants, unique fluid properties. The critical point of CO_2 is at $T_{crit} = 31.1°C$ and $p_{crit} = 73.7\ bar$[4]. Thereby, whenever the heat rejection temperature in the condenser is higher than $T_{crit} = 31.1°C$, the system has to run in a transcritical cycle, theoretically. In practice, the critical value for transcritical vs. subcritical operation is $T \approx 27°C$[3]. Since there is no condensation for transcritical operation within the change of state between compressor exit and expansion valve inlet, the heat of the supercritical CO_2 is rejected at gliding temperature levels by means of sensible heat rejection. Therefore, the condenser in transcritical CO_2 systems is named gas cooler. Austin et al.[4] state that because of the larger temperature glide compared to other refrigerants and sub-critical processes, a transcritical CO_2 system may be better suited for multiple heating loads[4], which can be distributed according to the temperature levels.

2.2 Selected CO_2 System Configurations

The following chapter presents firstly the basic refrigeration cycle in chapter 2.2.1. The basic refrigeration cycle can be improved depending on the application and existing standards. For CO_2 , the following chapters 2.2.2 - 2.3.1 build up and lead to the CO_2 heat pump utilized within this work and explain the corresponding benefits. The chapters cover benefits from a suction line heat exchanger, an ejector and different evaporator configurations.

2.2.1 Basic Refrigeration Vapor Compression Cycle

The theoretical heat pump / refrigeration cycle consists of a compressor, condenser, expansion valve and evaporator. Figure 2.1 shows a principal sketch of such a cycle.

For an ideal cycle, pressure drops within components and heat leakages into the pipes from the ambient are neglected. The compressor compresses the working fluid from low (evaporation) pressure to high (condenser) pressure and is thereby responsible for the fluid circulation. Within the condenser, the heat is rejected from the refrigerant to the ambient by means of a phase change from superheated gas to liquid. The flow is then throttled using an expansion valve. Within the evaporator, heat is transferred from the refrigerated space to the refrigerant, which leads to evaporation of the refrigerant. Afterwards, the
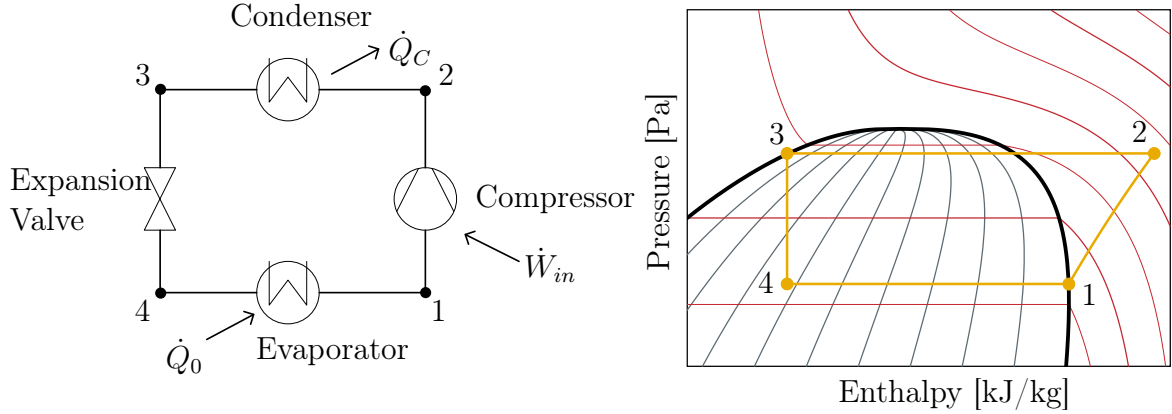
Figure 2.1: Simple Vapor Compression Refrigeration Cycle including log p-h Diagram

working fluid / refrigerant is sucked back into the compressor as vapor. The coefficient of performance is defined as Equation 2.1 shows.

$$COP = \frac{\dot{Q}_o}{\dot{W}_{in}} \tag{2.1}$$

The evaporator load $\dot{Q}_o$ is calculated using an energy balance by

$$\dot{Q}_o = \dot{m}_r \cdot (h_1 - h_4) \tag{2.2}$$

and the compressor work $\dot{W}_{in}$ as

$$\dot{W}_{in} = \dot{m}_r \cdot (h_2 - h_1). \tag{2.3}$$

2.2.2 Suction Line Heat Exchanger

Based on the basic vapor refrigeration cycle, as shown in Figure 2.1, a suction line heat exchanger (SLHX) can be applied for energy efficient operation and process safety. It transfers heat between fluids that exits the gas cooler and fluid prior to the compressor.

As it can be seen from Figure 2.2, the SLHX superheats fluid exiting the evaporator and cools gas exiting the gas cooler. Thereby, the specific cooling capacity increases, which increases the COP. A SLHX is furthermore required because the densities between liquid and vapor CO2 are similar, therefore, some small droplets may be transported in the suction line stream which can lead to liquid hammers in the compressor, and thereby damaging the system[3].

Since the SLHX superheats the exiting CO_2 from the evaporator, consequently the compressor exit temperature increases as well. This leads to a limitation in real systems as the oil used in the compressor limits the maximum discharge temperature, and thereby, it limits the maximum allowable superheat for a given pressure.
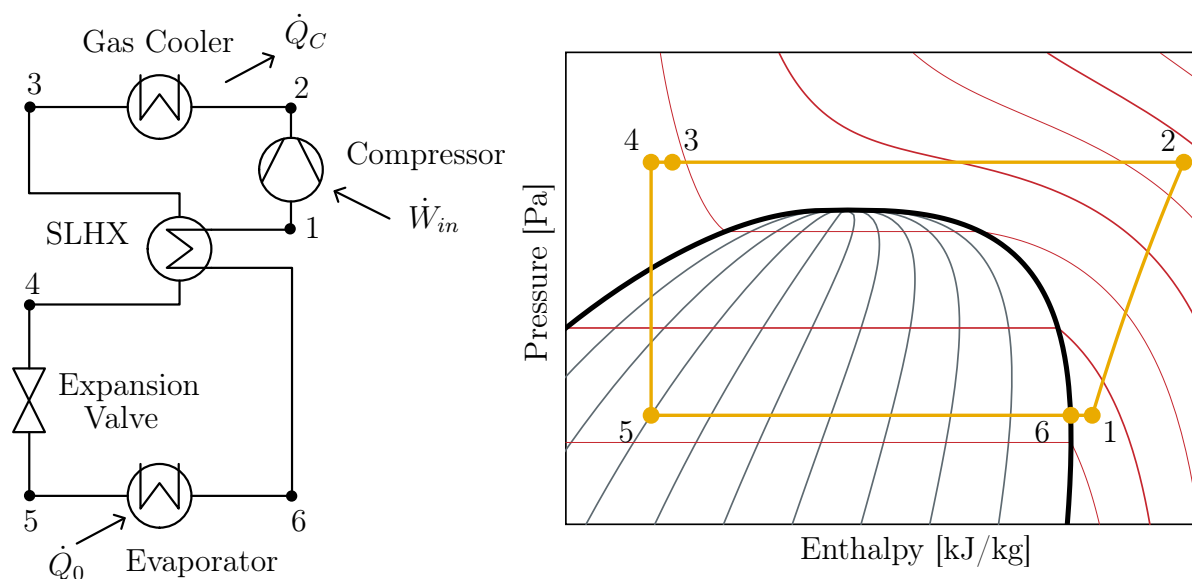
Figure 2.2: Suction Line Heat Exchanger including log p-h Diagram

2.2.3 Ejector

Elbarghthi et al.[6] state that major exergy destruction occurs from the throttling process within commercial CO2 refrigeration systems[6]. It is therefore of great interest to improve the throttling of the refrigerant. Austin et al.[4] describe several possible work recovery components and configurations, such as expansion turbines, rolling piston expanders and ejectors[4]. Out of those, ejectors have the advantage that they consist of no moving parts[6], which benefits the life expectancy, maintenance time and costs.
Elbarghthi et al.[6] report COP improvements by 8-27 % by the usage of an ejector[6].

The general working principle of an ejector is that the expansion of one fluid stream leads to circulation of a second fluid stream from lower pressure. An ejector operates with two inlet streams, the motive and the suction flow, and one discharge stream, as it can be seen in Figure 2.3.
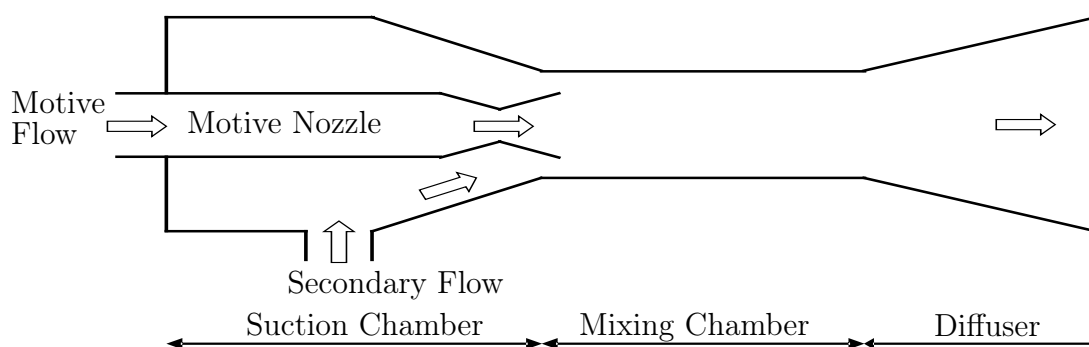
Figure 2.3: Schematic Drawing of an Ejector adapted from Yang et al.[7]

The motive flow, coming from the gas cooler, enters the ejector into the motive nozzle.

The motive flow is isentropically expanded from high pressure, and part of the pressure energy is converted into kinetic energy[6]. The expansion leads to a pressure difference between the secondary fluid stream inlet and the mixing chamber pressure, resulting in a suction mass flow[6].

Within the mixing chamber, due to different stream velocities, energy and momentum is exchanged between the motive flow and the suction flow[7]. Elbarghthi et al.[6] state that due to the mixing, part of the transferred energy transforms into kinetic energy of the entrained fluid, part of the energy transforms into pressure energy and part of the energy is dissipated due to frictional forces[6].

The subsequent diffuser increases the pressure energy by converting kinetic energy to pressure energy[8].

An exemplary integration of an ejector into a transcritical CO2 system is shown in Figure 2.4.
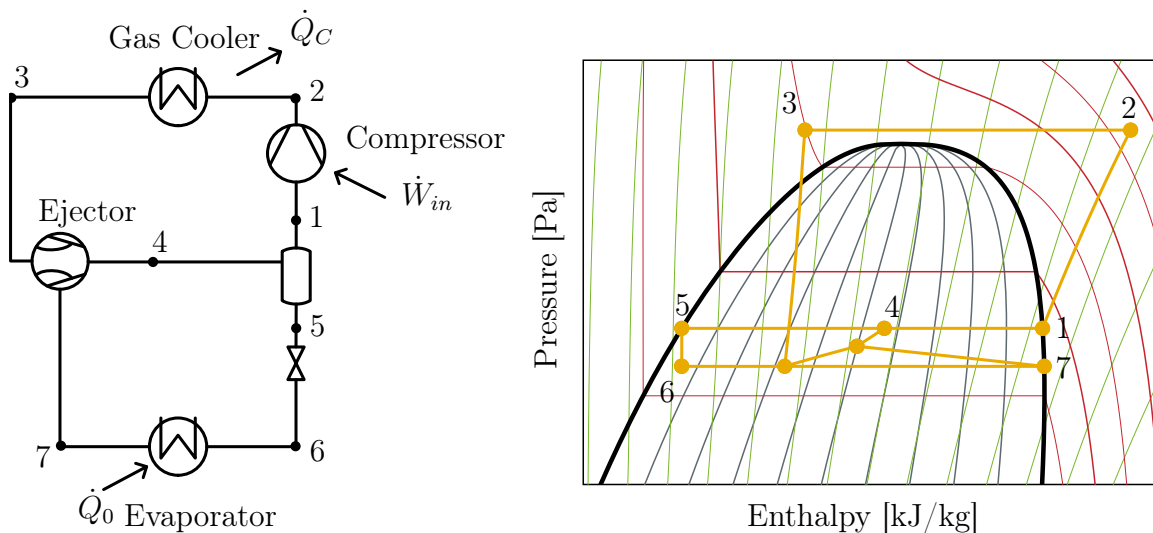
Figure 2.4: Exemplary Ejector System Setup including log p-h Diagram

The motive flow is expanded in the ejector and separated by the downstream separator. The liquid from the separator is expanded further and enters the evaporator at a lower pressure than the separator pressure. The pressure difference between separator pressure and evaporation pressure is overcome by the ejector and the mass flow from the evaporator is sucked back into the separator. Because of the higher suction pressure, the pressure ratio is lower and therefore, the COP increases.

Several key performance indicators (KPI's) are defined to evaluate the performance of an ejector. According to Elbarghthi et al.[6], the definitions are as following:

The pressure lift p_{lift} is defined by Elbarghthi et al.[6] as

$$p_{lift} = p_{rec} - p_{SN} \tag{2.4}$$

Elbel[8] suggests a different KPI, the pressure lift ratio Π_s, which he defines as

$$\Pi_s = \frac{p_{dis}}{p_{SN}} \tag{2.5}$$

The entrainment ratio ER is defined by Elbarghthi et al.[6] as

$$ER = \frac{\dot{m}_{SN}}{\dot{m}_{MN}} \tag{2.6}$$

and the ejector efficiency η_{ejec} as

$$\eta_{ejec} = ER \cdot \frac{\big(h(p_{dis}, s_{SN}) - h_{SN}\big)}{\big(h_{MN} - h(p_{dis}, s_{MN})\big)} \tag{2.7}$$

Elbarghthi et al.[6] achieved ejector efficiencies up to a maximum of $\eta_{ejec} = 0.369$ for $p_{MF} = 100$ bar and $T_{MF} = 25°$C.

Elbarghthi et al.[6] describe that two choking processes occur. The first choking is the choking of the motive flow in the motive nozzle, and the second choking occurs in the entrainment flow[6].

Elbarghthi et al.[6] further on distinguish three operation modes, the critical operation mode, sub-critical mode and stall condition or backflow condition[6]. The critical operation mode is characterized by a maximum entrainment ratio ER, which remains constant even when the discharge pressure p_{dis} is further reduced[6]. It is furthermore characterized by the above mentioned double choked flows[6]. In sub-critical operation, only the motive flow is choked, which is evoked by a rising discharge pressure p_{dis}[6]. If the discharge pressure p_{dis} rises further, the ejector may enter the backflow operation, where a backflow in the suction flow is evoked[6].

2.3 Gravity Fed Evaporator Configuration

Besides improving the expansion device, optimizations of the evaporator are known to be fruitful as well. In conventional refrigeration systems that use dry expansion evaporators leaves the refrigerant usually the evaporator superheated. Thereby, part of the evaporator area is used for superheating and not for evaporation. By changing the evaporator setup such that it operates in flooded operation, one can make use of the following benefits.

Hafner et al.[9] state that the increased liquid contact area benefits the heat transfer co-efficient[9]. Thereby, the heat transfer is improved and the evaporation temperature can be increased (Hazarika et al.[10] reported up to 4.3 K evaporation temperature lift for the investigated system[10]). Thereby, the systems coefficient of performance is increased[9]. Additionally, Zanetti et al.[11] argue that the liquid at the evaporator inlet reduces maldistribution problems, that are observed for dry expansion evaporators[11].
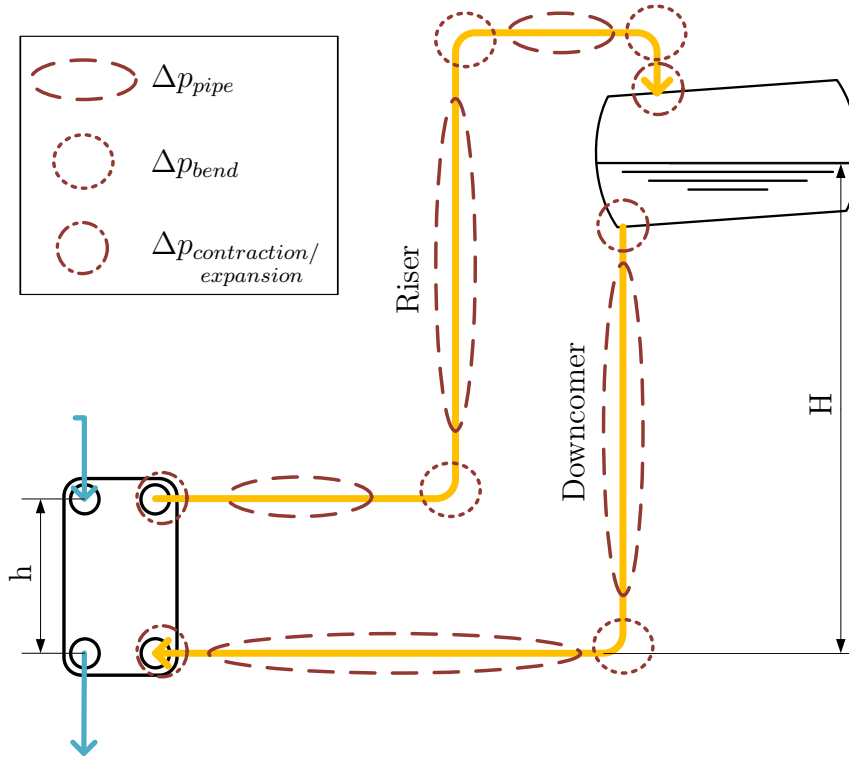
Figure 2.5: Pressure Losses within the Gravity Fed Evaporator Configuration due to Flow in Pipes, Bends and Changes in Pipe Diameter for a Counterflow Heat Exchanger Configuration

A flooded evaporator setup is shown in Figure 2.5. The system consists of a low pressure separator, which separates the fluid and liquid and can act as a suction accumulator. The separator is connected by the downcomer to the heat exchanger, through which liquid is supplied to the evaporator. The exit of the evaporator is connected back to the separator. The working principle is based on the thermosyphon effect, where density differences due to the evaporation of liquid to gaseous refrigerant lead to a buoyancy force, which circulates the refrigerant. The pressure difference between the evaporator and separator due to the static height H has to be larger than the occuring pressure losses within the heat exchanger, bends, frictional losses, etc.

The governing equation for the pressure difference that acts as the prime mover of the fluid is described by Equation 2.8 and adapted from Hazarika et al.[10]. It can be seen that the static height H plays a vital role within this system. A refrigerant flow occurs if the left hand side pressure difference overcomes the right hand side pressure losses.

$$H\rho_l g - h\rho_m g - (H - h)\rho_o g = \sum \Delta p_{losses} \qquad (2.8)$$

Cheng et al.[12] investigated into CO_2 evaporation and obtained Figure 2.6, which shows the heat transfer coefficient for evaporation in horizontal tubes. One can obtain from Figure 2.6 that the heat transfer coefficient stays rather high until a vapor fraction of approximately $x = 0.8$ is reached. Therefore, the optimum exit conditions for a flooded evaporator can be set to approx. $x = 0.8$.
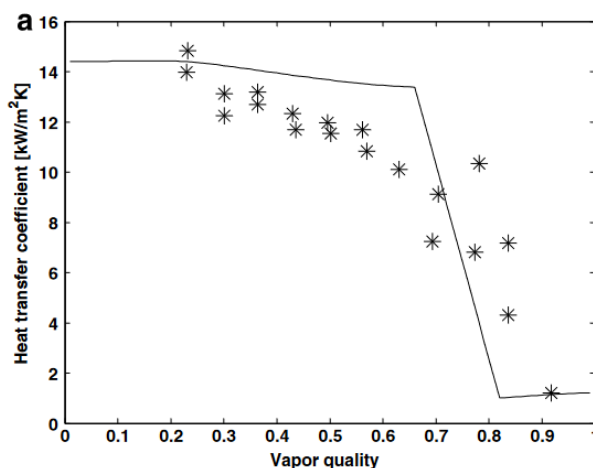
Figure 2.6: Heat Transfer Coefficients during evaporation for CO2 dependent on the vapor quality by Cheng et al.[12]

Hazarika et al.[10] describe the static height H and the riser diameter d_{ris} as the main parameters that influence the performance of the system (for constant secondary fluid side conditions).[10]

Based on their system dimensions, Hazarika et al.[10] obtained the following influence of the static height H (also known as liquid head) on the cooling capacity, as Figure 2.7 shows.

Figure 2.7a shows initially a rising cooling capacity $\dot{Q}_0$ with rising liquid head H. At the maximum cooling capacity, the vapor fraction is at 80 %, which Hazarika et al.[10] consider as the optimum condition[10]. For higher liquid heads, the cooling capacity slightly decreases, with decreasing vapor exit fractions within the evaporator.

Figure 2.7b shows the dependency of the cooling capacity on the riser diameter. As one can obtain from Figure 2.7b, the cooling capacity increases initially with increasing riser diameter, it reaches however a plateau for larger riser diameters than $\approx 26\ mm$.
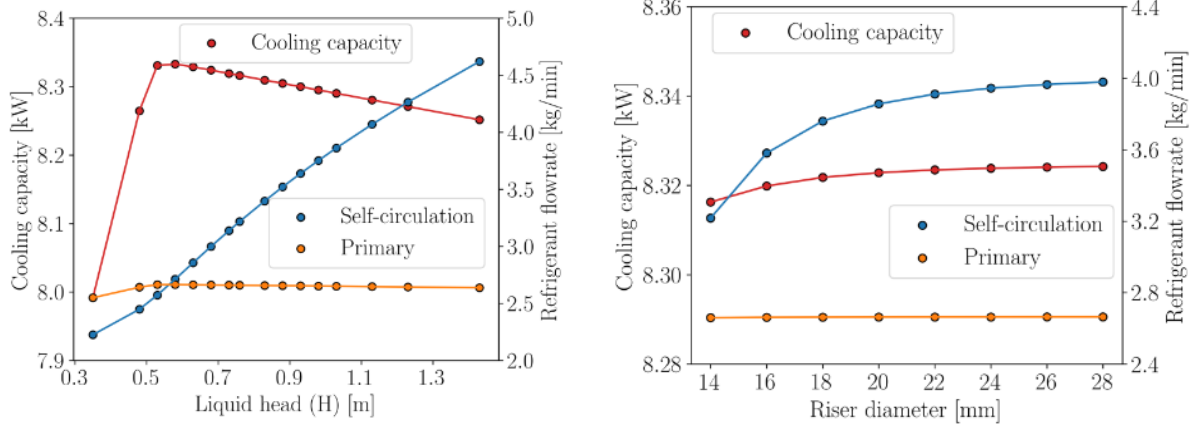
(a) Influence of the static height H onto the cooling capacity for the system investigated by Hazarika et al.[10]

(b) Influence of the riser diameter d_{ris} onto the cooling capacity for the system investigated by Hazarika et al.[10]

Figure 2.7: Gravity Fed Evaporator Performance Characteristics by Hazarika et al.[10]

2.3.1 Two Stage Evaporator

Further improvements for transcritical CO_2 refrigeration systems can be reached by combining the ejector driven evaporator presented in chapter 2.2.3 with the gravity fed evaporator (GFE) from chapter 2.3. Thereby, the following system setup, called a two stage evaporator, is reached (Figure 2.8):

The novelty of this system lies within the evaporator configuration, which features a heat exchanger, which consists of two brazed plate heat exchangers, that are mounted together back to back. Thereby, the secondary fluid is transported internally.

The system setup can be seen in Figure 2.8. It consists of the separator / liquid receiver, which supplies liquid CO_2 to the two stage evaporator. The separator is directly connected with the gravity fed evaporator part, whose working principle is explained in chapter 2.3. The outlet of the gravity fed evaporator goes back into the separator. Before the liquid CO_2 enters the gravity fed evaporator, one stream separates for the supply line of the ejector driven part of the evaporator. A control valve is placed upstream of the ejector fed evaporator, which acts as an expansion and control valve. The control can be chosen in different ways, within this application, an exit quality of $x = 1$ is desired. The ejector driven part of the evaporator acts as the suction line for the ejector, where refrigerant is sucked back into the tank, combined with expanded fluid from the high pressure.

Advantages of this system setup are the joined benefits of an ejector driven evaporator combined with a flooded evaporator. Meaning, the flooded evaporator setup benefits from the higher heat transfer coefficient due to flooded operation, leading to a higher evaporation temperature than dry expansion evaporators. Hence, the elevated evaporation pressure saves compressor work.
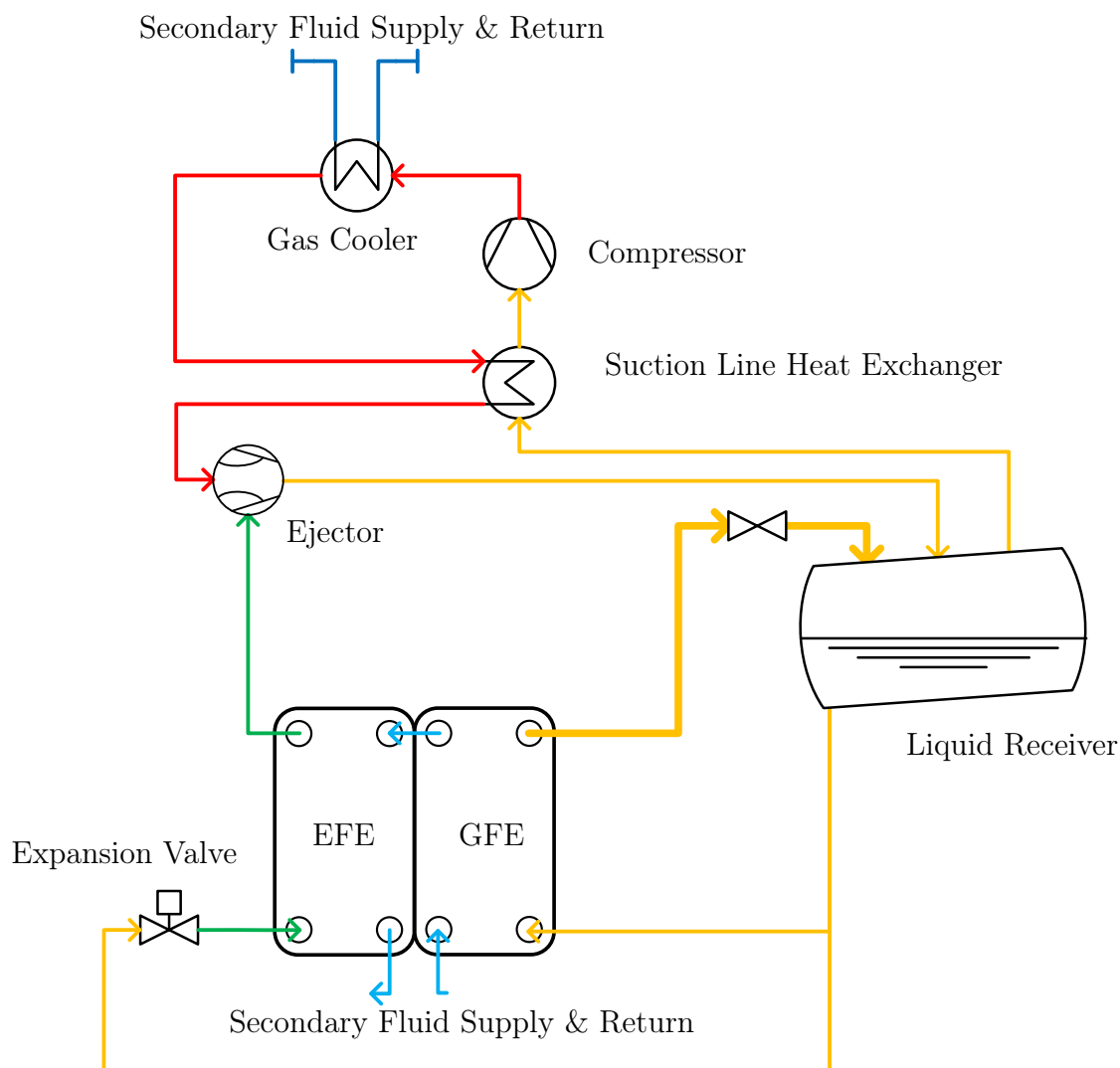
Figure 2.8: Two-stage Evaporator System with a parallel Flow Configuration on the GFE Side and a counterflow Configuration on the EFE Side

The additional benefits from the ejector driven evaporator are lower evaporation temperatures without lower suction pressure of the compressor. The combination of the gravity fed evaporator and the ejector driven evaporator features, therefore, the possibility to exchange heat at two different evaporation temperature levels, which benefits applications where large temperature glides on the secondary fluid side are required. Due to the two different evaporation temperatures, the heat exchanger effectiveness is increased.

Hafner et al.[9] investigated experimentally the system behaviour of a two stage evaporator for different secondary fluid mass flows and inlet temperatures. The evaporator configuration is a counterflow configuration on the GFE and EFE side. Water is used as a secondary fluid. Based on the findings by Hafner et al.[9], the causality chains from Figure 2.9 and Figure 2.10 are created.

Hafner et al.[9] describe in their publication that a rising water inlet temperature at the gravity fed evaporator $T_{w_{in},GFE}$ leads to an increase of the cooling capacity of the gravity fed evaporator $\dot{Q}_{o,GFE}$[9], which is congruent to the expectation based on Fouriers law (Figure 2.9a).

Furthermore, Hafner et al.[9] observe that with a rising water inlet temperature at the gravity fed evaporator $T_{w_{in},GFE}$, the approach temperature rises $\Delta T_{a,GFE}$ as well as the logarithmic mean temperature difference $\Delta T_{LMTD,GFE}$. The same causality chains can be drawn for the ejector fed evaporator part(Figure 2.9a).[9]

(a) Determined Dependencies on the Inlet Water Temperature based on Hafner et al.[9]

(b) Determined Dependency between the secondary fluid temperature glide of the gravity fed evaporator and ejector fed evaporator side based on Hafner et al.[9]
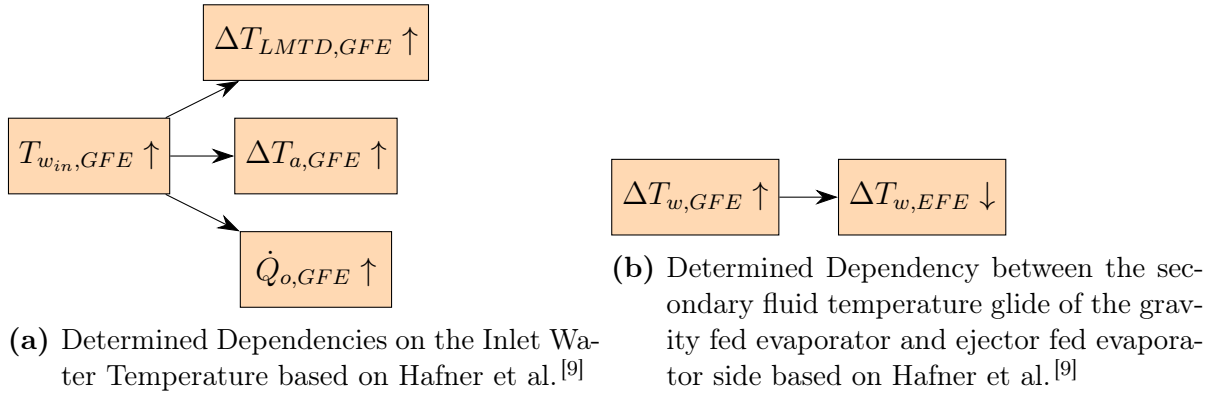
Figure 2.9: Correlation Chains for the Two-stage Evaporator investigated by Hafner et al.[9]

Hafner et al.[9] further concluded that a rising temperature glide in the gravity fed evaporator leads to a lower temperature glide in the ejector driven evaporator(Figure 2.9b)[9].

Hafner et al.[9] found that for the conditions of decreasing water mass flow rate and a high cooling capacity in the ejector fed evaporator $\dot{Q}_{o,GFE}$ (which corresponds to high water inlet temperature $T_{w_{in},GFE}$), the temperature glide of water throughout the gravity fed evaporator increases and a higher GFE exit temperature of the water is observed. Therefore, the temperature difference at the entrance of the EFE increases, which results in a higher cooling capacity in the EFE. Figure 2.10 shows this dependence. The authors further state that the decreasing water mass flow rate decreases the logarithmic mean temperature difference in the ejector fed evaporator.[9]
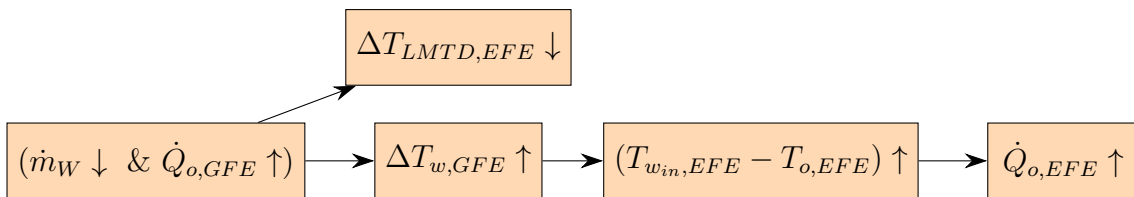
Figure 2.10: Further Correlation Chains for the Two-stage Evaporator investigated by Hafner et al.[9]

Hafner et al.[9] observe that the water inlet temperature has a larger influence on the cooling capacity than the water mass flow rate[9]. Tosato et al.[13] applied the two stage evaporator setup to a hotel with integrated domestic hot water production and report an average COP of 4.1[13].

2.4 Thermal Energy Storage (TES)

Thermal Energy Systems (TES) store energy short and/or long term for a later use. By implementing a TES into a suitable system, the following benefits have been proven.

Alva et al.[14] report that TES systems help to overcome the gap between energy production and energy utilization. The gap can be in time and/or location[14]. Furthermore, TES systems allow to shift the peak power demand from high demand hours to low demand hours[15], which in return can save electricity costs due to differences in peak and off-peak pricing[14]. If a TES system is integrated during the system design, smaller components can be selected, resulting in lower component costs[16].

TES can be divided into three categories: sensible, latent and chemical storage[14]. Within sensible thermal energy storage, the material stores energy by means of a temperature change. Alva et al.[14] calculate the stored energy as

$$Q = m \cdot c_p \cdot \Delta T \tag{2.9}$$

and thereby, the effectiveness of a material depends on the its mass m (or volume V and densityρ), its specific heat capacity c_p and the temperature difference ΔT[14].
Sensible TES is mostly used within high temperature applications due to the high thermal stability and low costs, except for liquid metals and mineral oils[14]. Disadvantages of sensible TES are the change in outlet temperature during discharging and their low energy storage density compared to latent heat storage[14].

Latent TES relies on the phase change of the material, which is used to charge, discharge and storage of energy[14]. As mentioned before, latent TES has a higher energy storage density, which is up to 50 - 100 times higher[14].
Alva et al.[14] state that during the discharge process, the outlet temperature stays constant, but as a main disadvantage, the low thermal conductivity is given[14].

The third TES is the chemical storage. Alva et al.[14] present the main advantages to be the highest energy storage density and the possibility of long storage times. Alva et al.[14]

furthermore describe for certain materials main disadvantages that possibly sintering and grain growth may occur, as well as slow dehydration rates[14]. According to Alva et al.[14], chemical TES is still at laboratory scale.

2.4.1 Thermal Energy Storage within Air Conditioning

TES systems have been implemented into air conditioning in a variety of designs, which serve different optimization and operation strategies. Within literature, TES in air conditioning systems has been implemented to be utilized in combination with free cooling or at either the warm or cold side of a heat pump. The following paragraphs will provide an overview over some system designs.

Implementation of TES for free cooling:
Zeinelabdin et al.[17] experimentally investigated a TES system directly placed within the supply air flow for hot arid regions. The working principle is to charge the TES system using cold air at night and to discharge it during the day by cooling the supply air to the building. Thereby, free cooling is utilized. RT28HC by Rubitherm is used as a PCM with a phase change temperature range of 27-29 °C.[17]

Implementation of TES on the warm side of a heat pump:
Said et al.[18] placed the TES into the air stream that is used for heat rejection from the condenser. The operation strategy is to charge the TES during nighttime and utilize it to cool down the air stream to the condenser. Said et al.[18] report that the condenser pressure decreases and subcooling increases, which in turn leads to a higher COP of the system. SP24E by Rubitherm is used as a PCM. Said et al.[18] report on power savings of 9.8 - 11.2 %, depending on the PCM plate configuration.[18]

Implementation of TES on the cold side of a heat pump:
Sanaye & Hekmatian[15] simulated the integration of ice thermal energy storage (ITES) into an office building located in Bushehr, Iran. The ITES is connected to the evaporator of the heat pump and the AC heat exchanger.[15] Sanaye & Hekmatian[15] observe a reduction in electrical power consumption, as well as a reduction in annual operating costs due to operation of the system during off-peak hours. The 4E analysis shows furthermore a reduction in CO_2 emissions as well as an increase in payback times.[15]

Yan et al.[19] showed the implementation of a ITES as a seasonal storage in a small size building (2000m^2) in Beijing, China. The system uses an ITES that is charged during winter and discharged during summer. It is split into two areas, whereby one can be discharged first during summer time and then be used as a sensible thermal energy storage

for chilled water. The ITES is combined with chiller operation. The system has shown to reduce the annual electricity consumption and costs by 22 % and 76 %, respectively. The life cycle costs decreased as well by approximately 40 %. [19]

Elhelw et al. [20] analyzed among others the implementation of ITES into the air handling unit of an administration building in Alexandria, Egypt. The ITES was implemented as a retrofit system in parallel to the exisiting cooling cycle, and is charged by a separate heat pump. The results show that the energetic and exergetic performance increased, depending on the system configuration and power reductions of up to 6.89 % were achieved [20].

Selvnes et al. [21] implemented a latent CTES unit utilizing water into the air conditioning system of a supermarket in Norway [21]. The AHU, as well as the charging / discharging of the pillow plate CTES unit, is carried out by utilizing CO_2 as a working fluid within a CO_2 refrigeration system [21]. Selvnes et al. [21] report on a reduction of the peak power consumption of up to 19 %. Furthermore, the gained results show the cost savings of the CTES unit depend on the intraday fluctuation of the electricity price, as well as the general electricity price [21].

2.4.2 CTES Charging and Discharging Strategies

Yu et al. [22] provided within his publication an overview over different control techniques and operation strategies for thermal energy storage within buildings [22]. Yu et al. [22] differentiate between classic local-loop control, hard control, soft control, other control and hybrid control [22].

Local-loop control operates based on a target variable and the system operates either by On-Off control, by a PID-control or a programmable logic controller to maintain the target variable at the setpoint condition [22]. According to Yu et al. [22], programmable logic controllers are utilized nowadays in a majority of classical loop controllers.
Within the hard control, a system model is implemented within the control structure, which is used to determine ideal control parameters [22]. Soft control utilizes artificial intelligence to determine the ideal operating conditions [22]. Within the Other Control group, reinforcement learning and swarm optimization methods are utilized [22]. Hybrid Control strategies combine different control techniques out of the previously presented ones together.

3 System Design and Operation Modes

The properties of the TSEV, such as the ability to enable large secondary fluid side temperature glides, besides the increased energy efficiency, make the TSEV prone to be used within air conditioning applications utilized with a secondary fluid. The large temperature glide of the secondary fluid decreases the required mass flow and thereby reduces pump work. Therefore, a system is developed, that integrates the TSEV into an air conditioning system by an intermediate secondary fluid system.

For the application in e.g. fish processing facilities, hotels, etc., possible system extensions such as additional cold storage rooms and freezers are included within the system setup. For later simulations is the demand of cold storage rooms and freezers neglected.

The system setup is shown in Figure 3.1, and consists of the CO_2 heat pump subsystem, including a freezer and cold storage space, and the hydronic subsystem. Water is used as a secondary fluid due to the availability, low cost and the possibility to be used as a latent thermal energy storage.

The heat sink of the CO_2 heat pump system is indicated as a heat rejection to ambient, but heat can also be recovered by e.g. DHW production. Exemplary DHW heat recovery is found in the publications by e.g. Smitt et al.[23], that showed the integration of DHW water production of a CO_2 heat pump system, or the Multipack report No.2[16]. The following chapters 3.1 - 3.2.4 will introduce the system setup of the CO_2 heat pump subsystem and the hydronic AC system and chapter 3.3 the system control.

3.1 CO_2 Heat Pump Subsystem

The CO_2 heat pump consists of the TSEV arrangement, which is connected by a suction line heat exchanger to the MT compressor unit. Additionally, a low-temperature stage is added to charge the ice tank and to operate a freezer.

The proposed CO_2 heat pump configuration consists of parallel compressors, which are staggered in capacity. One of the compressors serves as the baseline compressor, with its design capacity slightly above the required capacity for the TSEV operation, and the parallel compressor supplying enough capacity for the charging of the TES. Depending on the actual sizing of the compressors, possibly a third compressor may be installed for redundancy and to provide an even finer staggered system capacity, that allows operating the compressors near their design points for longer periods.

The heat sink of the system is indicated within Figure 3.1 as the heat recovery / heat
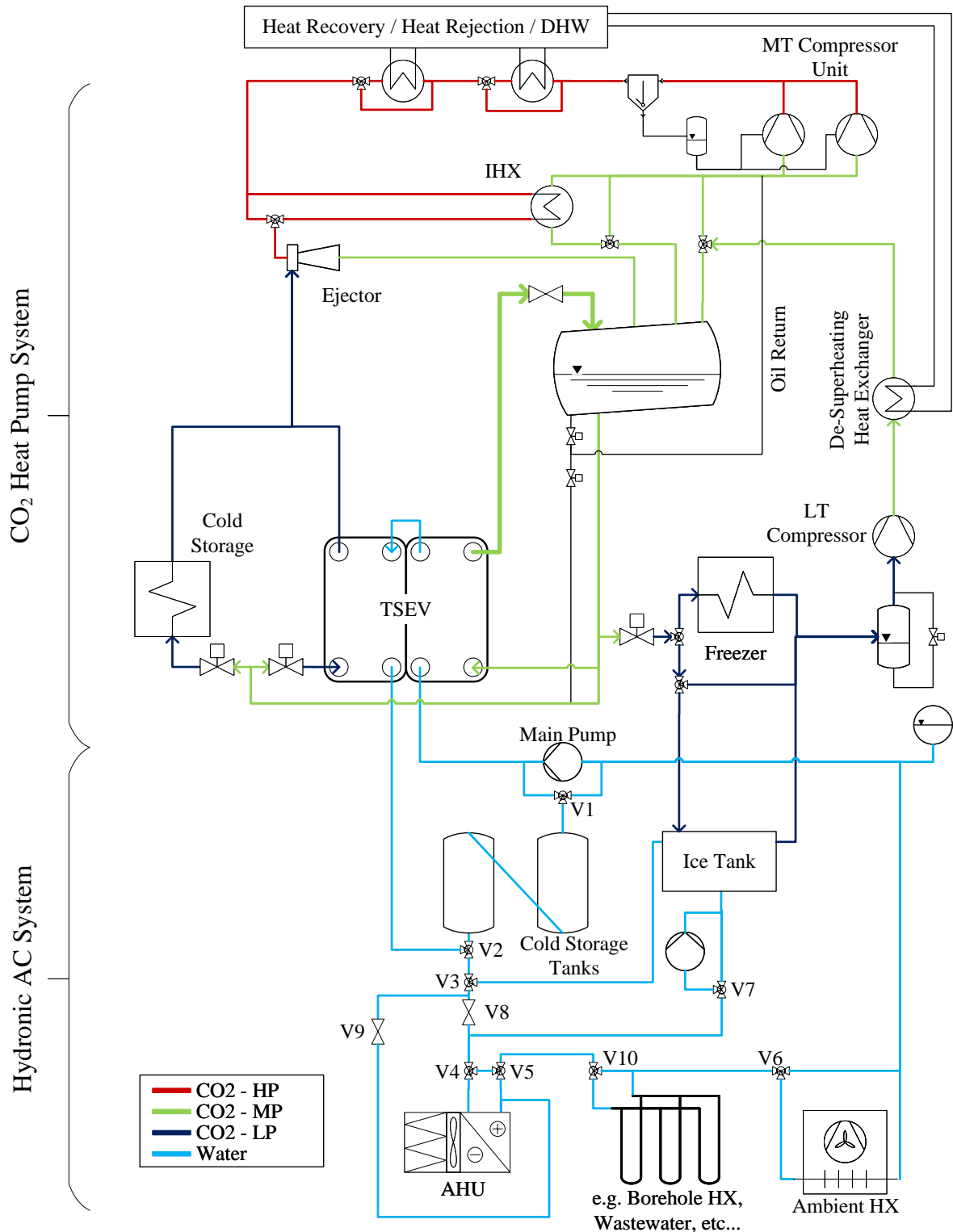
Figure 3.1: Heat Pump and Hydronic System Setup

rejection component. The system operates with an internal heat exchanger (IHX) and a bypass of the IHX, to regulate the superheat of the CO_2 before the compressors and to regulate the temperature prior to expansion.

An ejector is used as an expansion device, with the suction nozzle maintaining the lower

pressure level of the TSEV and the cold storage room. The discharge nozzle connects to the liquid receiver. The liquid receiver serves as the CO_2 storage of the system during still-stand conditions and supplies liquid CO_2 to the TSEV and low-temperature stage of the system. The TSEV is connected to the liquid receiver (and ejector) to operate using the gravity and ejector fed evaporator. By controlling the rotational speed of the compressor is the pressure level and consequentially the water exit temperature of the TSEV controlled. The low-temperature stage of the system expands liquid CO_2 from the liquid receiver further to the desired pressure level and evaporates within the ice tank to charge the TES or to evaporate within the freezer. The CO_2 from the LT stage is compressed by the LT compressor to the liquid receiver pressure level and de-superheated using the heat recovery / heat rejection system. The de-superheating heat exchanger could potentially serve as a pre-heater for the DHW production, if the CO_2 exit temperatures from the LT compressor are within the required temperature range.

The suction line of the MT compressor unit separates into one from the IHX, one from the LT de-superheating heat exchanger, and a bypass of those. Furthermore, the CO_2 exiting the de-superheating heat exchanger can be either discharged into the liquid receiver, or directly flow into the suction line of the MT compressor unit. Thereby, in combination with the IHX configuration, a control of the superheat of CO_2 prior to the MT compressor unit is achieved.

Oil management is implemented using an oil separator with a downstream receiver, which separates and collects the oil after discharge of the compressor unit, respectively. Due to the physical setup of the TSEV, oil will collect at the lowest point of the piping system, and therefore, an oil return line is implemented from the TSEV, by using the venturi effect. Oil return from the LT stage is ensured by the indicated oil / valve connection over the suction accumulator.

Within an actual system, one would most likely install an additional suction accumulator prior to the MT compressor unit, to ensure that no liquid refrigerant under any circumstances enters the compressors.

3.2 Hydronic Subsystem

The hydronic subsystem is shown within the lower part of Figure 3.1. It consists of an ice tank and cold water storage tanks (CST) as thermal energy storage, the two-stage evaporator, as well as the AHU and the ambient heat exchanger.

Figure 3.2 shows the setup of the ice tank, which consists of vertical pipes that run through a tank filled with water. Within the vertical pipes, CO_2 evaporates due to the

heat transfer from the water to the CO_2 . Water is entering the tank from either the top or bottom and is cooled down by flowing along the ice layer that forms around the tubes due to the evaporation of CO_2 .
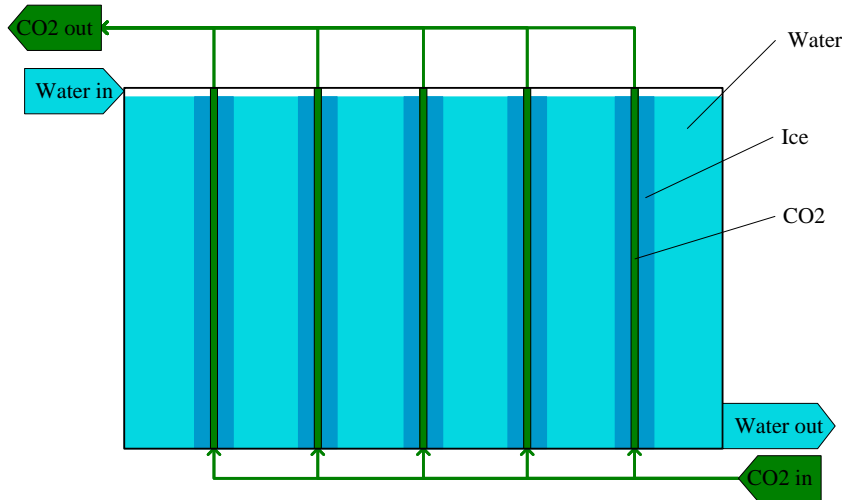
Figure 3.2: Cold Thermal Energy Storage Unit - Ice Tank Setup

The hydronic sub-system can be easily extended with additional heat sources, such as a borehole heat exchanger, process industry exhaust air or other heat sources, depending on the application and quality of the heat source. For the operation with ambient air as a heat source, the ambient heat exchanger needs to be protected against freezing within the water pipes, which requires potentially a separate glycol loop.

The following Table 3.1 shows an overview of the possible operation modes of the hydronic sub-system and is ordered after the CST operation. Since the ice tank is charged through the CO_2 system, the charging of the ice tank is not included in Table 3.1 or as an extra operation mode. Operation modes that allow the use of the ambient heat exchanger are marked in the "AHX Possible?" column.

For the further work, the operation modes are sorted based on a rule-based optimal control strategy for the utilisation of an ice storage in cooling applications by the American Society of Heating, Refrigerating and Air-Conditioning Engineers[24]. Within the developed control strategy, the operation modes of the CTES system are classified into three main system operation strategies: CTES charging, CTES discharging-maximizing storage discharge rate and CTES discharging-minimizing the storage discharge rate and maximizing the use of the chiller. Therefore, the operation modes from Table 3.1 are assigned to the corresponding system operation strategy and are presented in detail in the chapters 3.2.1-3.2.3. The rule-based optimal operation strategy will be presented in chapter 3.3.

Table 3.1: Operation Modes of the Hydronic Subsystem (TSEV - Two Stage Evaporator;
CST - Cold Storage Tanks; MP - Main Pump
IP - Ice Tank Pump; AHU - Air Handling Unit;
AHX Possible ? - If the operation of the ambient heat exchanger is possible)

	Operation Mode	TSEV	CST	MP	IP	AHU	AHX Possible ?
Charging of CST + AC off	1	On	On	On	Off	Off	Yes
	2	Off	On	Off	On	Off	No
	3	On	On	On	On	Off	No
Charging of CST + AC on	4	On	On	On	Off	On	Yes
	5	Off	On	Off	On	On	No
	6	On	On	On	On	On	Yes
CST Neutral + AC on	7	On	Off	On	Off	On	Yes
	8	Off	Off	Off	On	On	No
	9	On	Off	On	On	On	Yes
CST Discharge + AC on	10	On	On	On	Off	On	Yes
	11	Off	On	On	On	On	No
	12	Off	On	On	Off	On	Yes
	13	On	On	On	On	On	Yes
	14*	Off	On	On	Off	On	No
	15*	On	On	On	Off	On	Yes

* The flow is regulated for these operation modes by Valve 3
through the ice tank

Operation Mode $OM = 2$, $OM = 3$, $OM = 5$, $OM = 6$ are not intended to be used by the control strategy and are therefore presented as additional operation modes in chapter 3.2.4.

3.2.1 CTES Charging

As shown in Figure 3.1, the hydronic subsystem consists of two CTES units, the cold water tanks and the ice tanks. Since the ice tanks can be charged independently of the operation of the hydronic circuit by the LT compressor, and therefore the charging of those is not affecting the hydronic circuit directly, no further representation of ice tank charging is required at this point.

Figure 3.3a shows operation mode $OM = 1$, which charges the cold water storage tanks at maximum system capacity. Hence, the main pump circulates water through the TSEV into the cold water tanks. In case there is a cooling demand of the AC system while charging the cold water tanks, the system can switch to $OM = 4$ (Figure 3.3b), which is based on $OM = 1$, but distributes parts of the chilled water to the AHU to meet the AC demand. Within both OMs, the ambient heat exchanger can be operated, but a change in valve V2 would be required to redirect flow through the ambient heat exchanger in $OM = 1$.
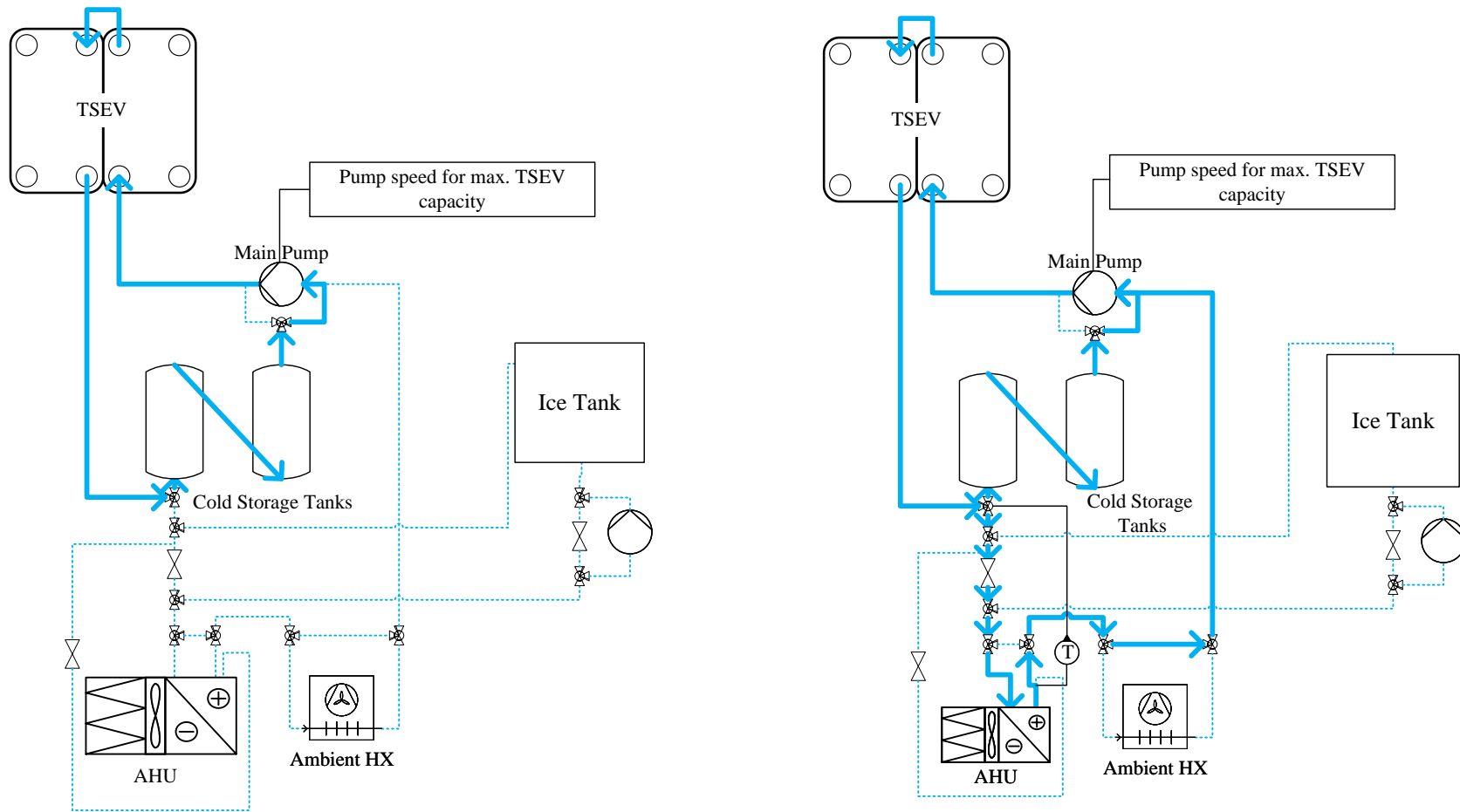
(a) Operation Mode 1: Cold Water Storage Tank Charging with Two-stage Evaporator

(b) Operation Mode 4: Cold Water Storage Tank Charging with Two-stage Evaporator and AHU active

Figure 3.3: Operation Modes during Cold Water Storage Tank Charging

3.2.2 CTES Discharging - Min. Use of Storage incl. Peak Load Limiting

The operation strategy by the American Society of Refrigeration and Air-Conditioning Engineers distinguishes between a CTES Discharge - minimal use of storage, including peak load limiting and a maximum use of storage (which's operation modes are presented in the following chapter).

The minimal use of storage in this case requires the TSEV to operate full time up to it's maximum system capacity. In case the system capacity increases, the remaining load needs to be covered by the thermal energy storage, respectively the water and ice tanks.

The operation modes are presented with increasing system capacity, which results in this case in an increasing use of the CTES units. Since the charging of the ice tank requires lower evaporation temperatures than the charging od the cold water storage tanks, the efficiency of ice production is lower, and therefore, the discharge of the water tanks is preferred over the ice tank discharge, when additional load needs to be covered. All operation modes within this system strategy allow to include the ambient heat exchanger.

If the AC demand is lower than the maximum TSEV capacity, $OM = 7$ in Figure 3.4a is activated. The main pump circulates water through the TSEV followed by the AC heat exchanger. The main pump is controlled by the exit temperature of the circulated air out of the AC heat exchanger, as shown in Figure 3.4a.

In case the AC load rises further, $OM = 10$ is activated, where the flow out of the main pump is distributed between the TSEV and the cold storage tanks. Thereby, the TSEV can operate at the design system capacity and the cold storage tanks cover the remaining load. In this case, V2 controls the flow such that the design TSEV system capacity is reached, which can be measured based on water mass flow and temperatures of the in and outflow of the TSEV. This system configuration is shown in Figure 3.4b.

In case the operation $OM = 10$ is not sufficient to meet the setpoint conditions of the AHU air flow and the main pump operates at its maximum speed, $OM = 15$ is activated (see Figure 3.5a). $OM = 15$ operates the TSEV at the design capacity, with the cold storage water tanks connected in parallel. The confluent water of the TSEV and CST is separated by V3 to flow either through or bypass the ice tank. Thereby, the water temperature can be further reduced to meet the AC demand. As the main pump is operating at its maximum speed, and the distribution between TSEV and the cold storage tanks is done by V2 to meet the design heat pump capacity, V3 controls the air exiting the AHU to meet the setpoint conditions.
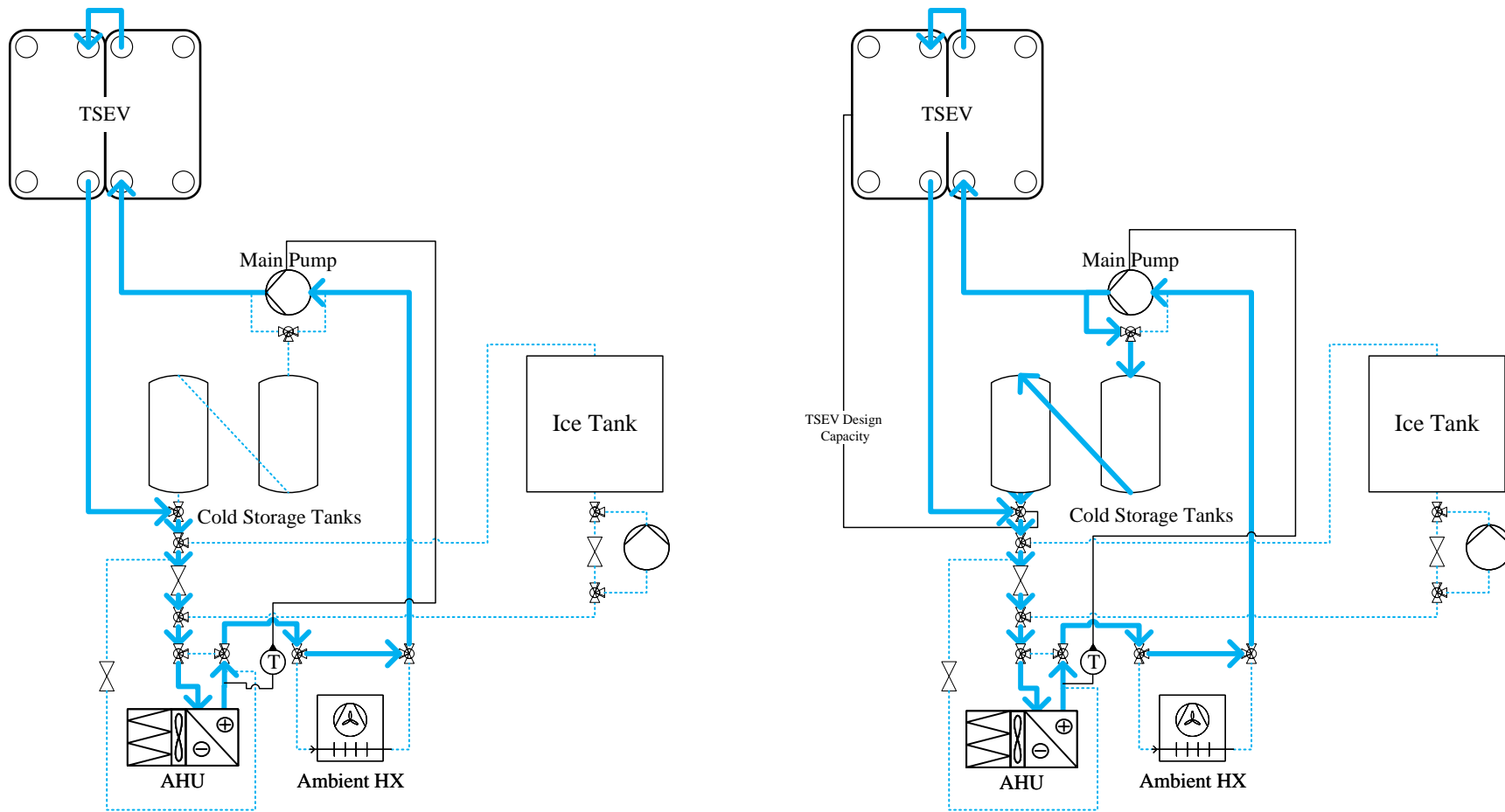
(a) Operation Mode 7: AHU Load covered solely by the Two Stage Evaporator

(b) Operation Mode 10: AHU Load covered by Two-Stage Evaporator Operation and Cold Water Storage Tank Discharge

Figure 3.4: Thermal Energy Storage Discharge Operation Modes utilizing Minimal Use of Storage 1/3
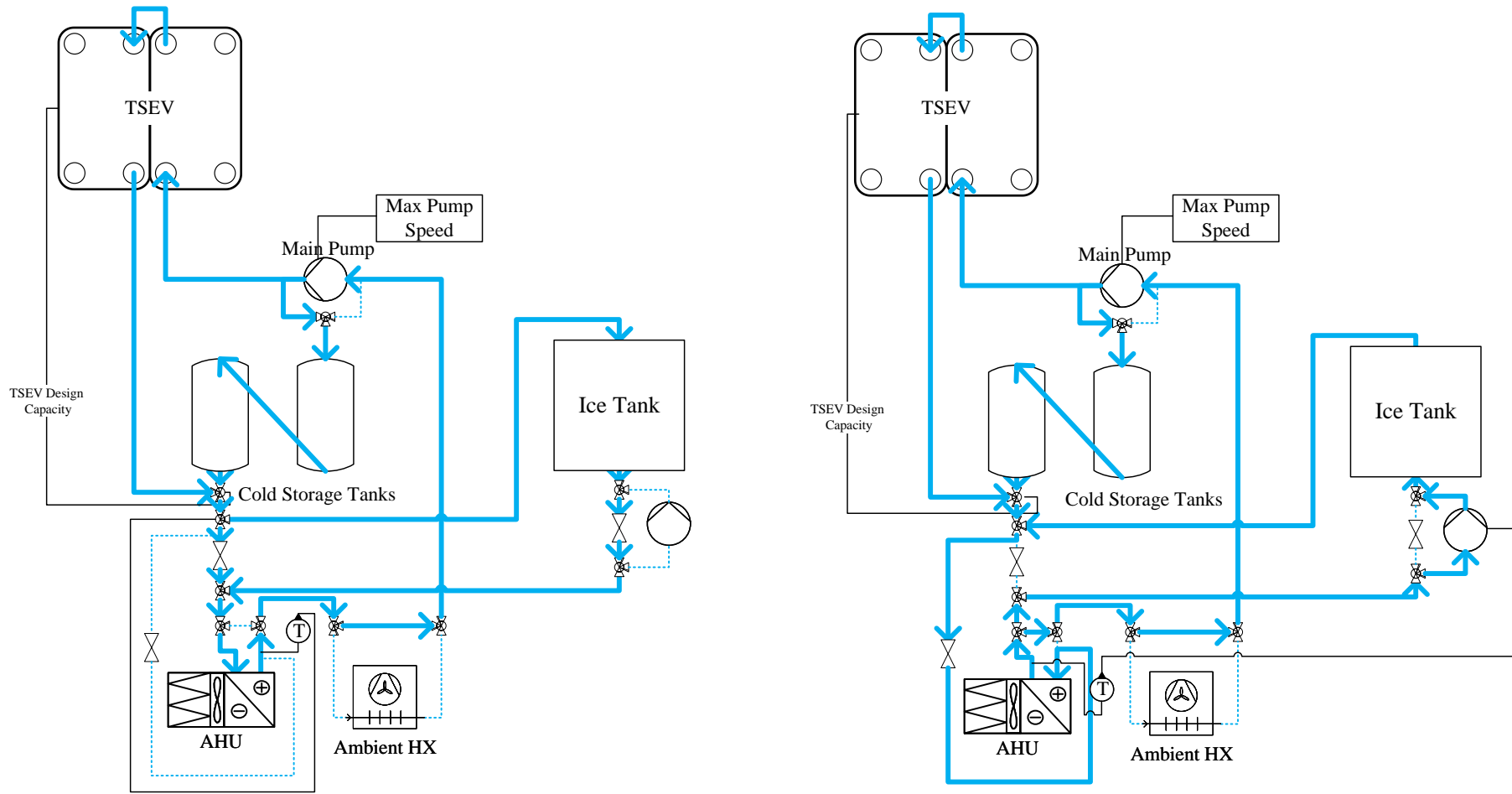
(a) Operation Mode 15: AC Load covered by the Two-stage Evaporator, Cold Storage Tanks and Ice Tank Discharge. Ice Tank Pump remains inactive

(b) Operation Mode 13: AC Load covered by the Two Stage Evaporator, Cold Storage Tanks and Ice Tank Discharge. Ice Tank Pump is active

Figure 3.5: Thermal Energy Storage Discharge Operation Modes utilizing Minimal Use of Storage 2/3

For the case that even larger system capacities are required, $OM = 13$ can be used. It is based on $OM = 15$, but the pump on the ice tank is activated, such that the mass flow of water through the AHU is increased through the use of the ice pump (Figure 3.5b). In this case V3 is passive and the ice pump ensures to meet the setpoint conditions for the conditioned air exiting the AHU.

If the cold water tanks run empty while the system operation strategy is "CTES Discharge - minimal usage of Storage", $OM = 9$ is activated. The main pump circulates water through the TSEV at its design conditions for operation at the design capacity of the TSEV. The temperature of the exiting air of the AHU is controlled by the ice pump, which circulates additional mass flow through the AC heat exchanger. Hence, only the TSEV and the ice tank cover the load on the AHU.
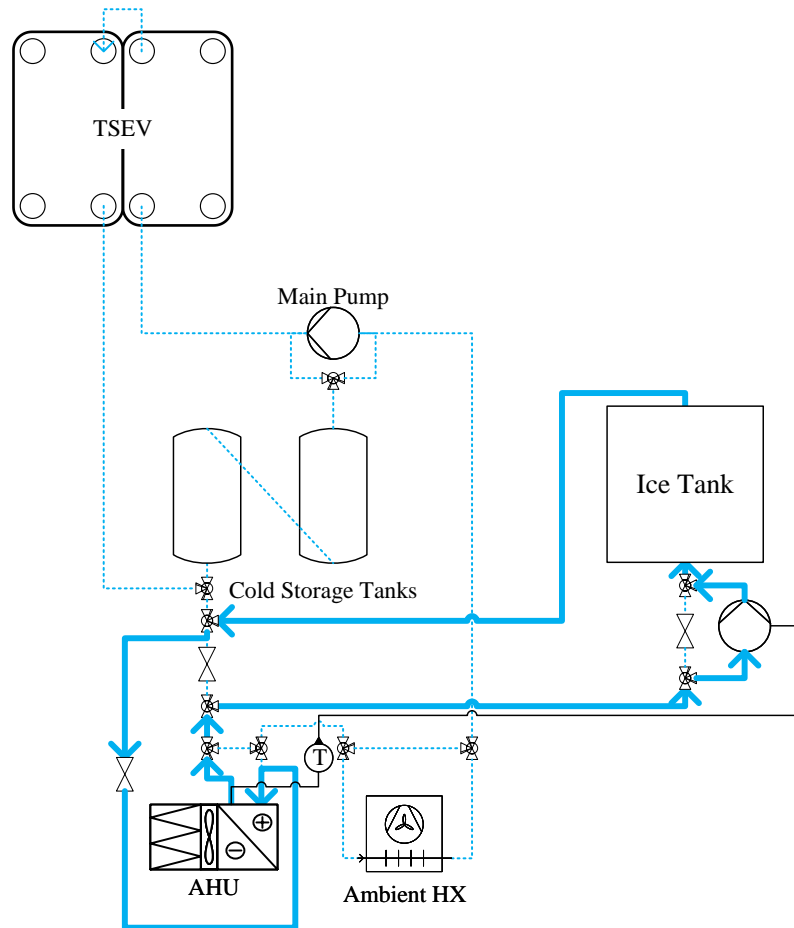
Figure 3.6: Thermal Energy Storage Discharge Operation Modes utilizing Minimal Use of Storage 3/3 - Operation Mode 9: AC Load covered by the Two-stage Evaporator and Ice Tank by the Main Pump and Ice Tank Pump

3.2.3 CTES Discharging - Max. Use of Storage

In case that maximal Discharge of the TES is desired, the proposed system configuration offers four operation modes. It should be noted that during this operation strategy, the heat pump is turned off and the cooling demand is solely met by the ice and cold water storage.

Similar to previous chapter 3.2.2, the discharge of the cold water tank is preferred over the discharge of the ice tank due to the described efficiency drawback. In case that the cold water tanks run dry, $OM = 8$ in Figure 3.7a discharges the ice tank. Since only the ice tank is used for meeting the cooling demand, the ice pump regulates the water flow and thereby meets the outlet conditions of the ventilation air.

$OM = 12$, shown in Figure 3.7b, only uses the cold water tanks to meet the load from the AC. The exit temperature of the AHU is controlled by the mass flow rate of the main pump. As the warmer water enters the tanks from above, the stratification within the tanks is conserved.

If the AC demand cannot be met by the single discharge of the cold water tanks, $OM = 14$ combines the discharge of the ice tank and the cold water tanks at full main pump capacity. To meet the setpoint conditions of the AHU, V3 redirects the water flow through either the ice tank or a bypass of the ice tank, and thereby adapts the temperature of the water to meet the air setpoint conditions of the AHU.

For further capacity increases, $OM = 11$ features the simultaneous discharge of the cold water tanks and the ice tank by using both pumps, the ice pump and main pump. As previously discussed, the main pump operates at its full capacity, whereas the ice pump controls the additional flow to meet the setpoint conditions of the AC air exiting the AHU.
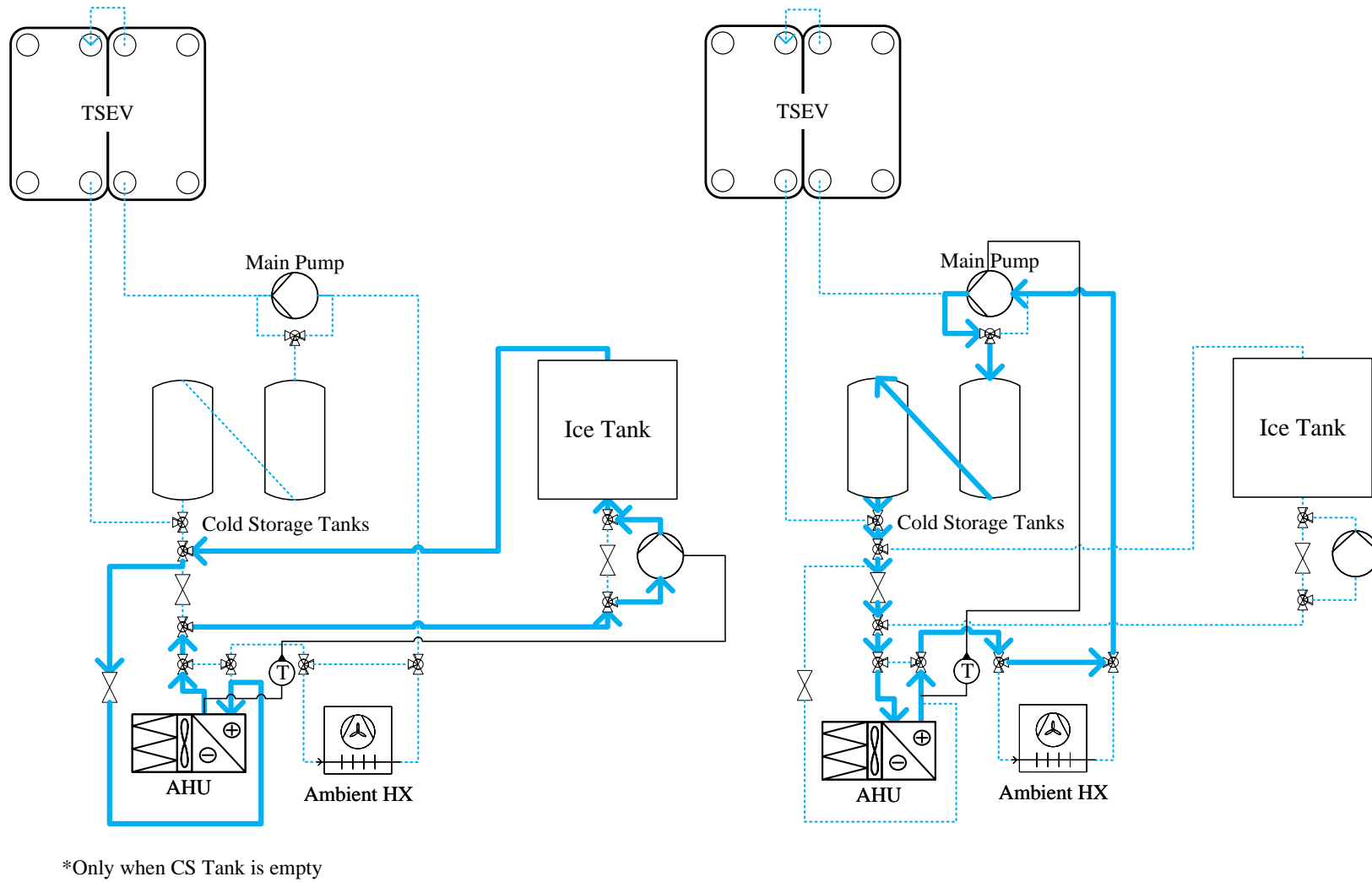
(a) Operation Mode 8: AC Load is covered by the Ice Tank and Ice Tank Pump

(b) Operation Mode 12: AC Load is covered by the Cold Storage Tanks

Figure 3.7: Thermal Energy Storage Discharge Operation Modes utilizing Maximal Use of Storage 1/2
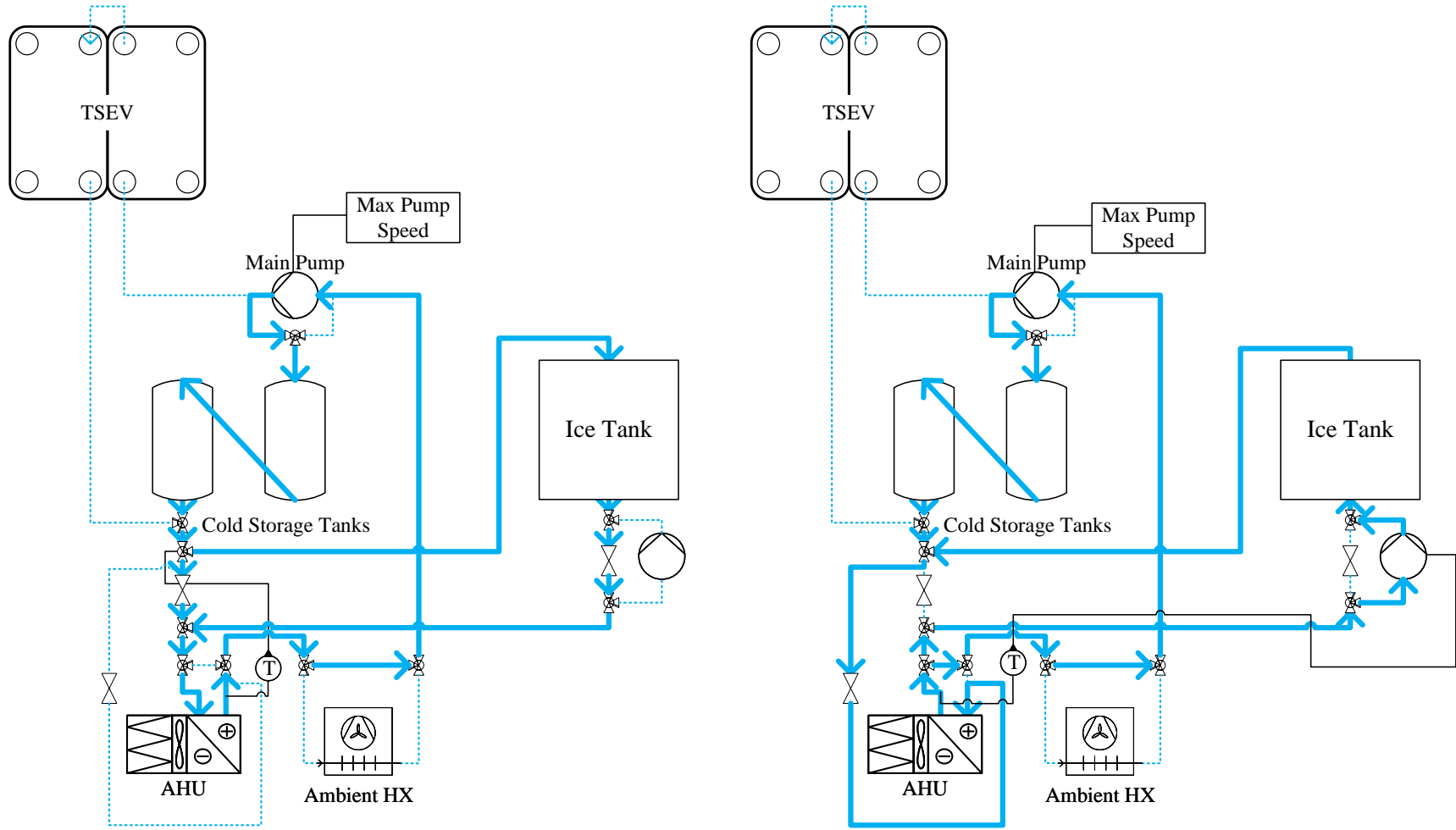
(a) Operation Mode 14: AC Load covered by the Cold Water Storage Tank and Ice Tank. Ice Tank Pump remains inactive

(b) Operation Mode 11: AC Load covered by the Cold Water Storage Tank and Ice Tank. Ice Tank Pump is active

Figure 3.8: Thermal Energy Storage Discharge Operation Modes utilizing Maximal Use of Storage 2/2

3.2.4 Additional Operation Modes

Additional operation modes are operation modes, that the system configuration offers, but that are not intended to be frequently used by the rule based control strategy, which will be presented in chapter 3.3.

Operation mode $OM = 2$ offers the possibility to charge the cold storage tanks by discharging the ice tank by using the ice tank pump. Operation Mode $OM = 2$ is shown in Figure 3.9a. To charge the CST using the ice tank is from an energy efficiency point of view not beneficial, due to the required lower evaporation temperatures to charge the ice tank compared to the operation of the TSEV to charge the CST. Hence, $OM = 2$ is only activated when the CST are required to charge and the heat pump should remain deactivated. Such a scenario could occur, when the ice tank capacity contains sufficient charge (enough thermal energy is stored) to cover an appearing demand on the AHU over a certain period, but the ice tank discharge rate is not sufficient to cover the appearing load at a specific point in time. Therefore, the CST could be charged without operating the heat pump system and providing enough cold water discharge rate to cover the load on the AHU. The AHU remains inactive in $OM = 2$.
If the operation of the AHU is required, $OM = 5$ is activated, which operates additionally the AHU, but is otherwise applied in the same scenario and shown in Figure 3.9b.

Operation Mode $OM = 3$ charges the CST by using the TSEV and the ice tank and is shown in Figure 3.10a. The charging of the CST by simultaneous operation of the TSEV and ice tank discharge is only advisable, if e.g. the AHU load prediction foresees large AHU loads in the near future, that cannot be covered by the ice tank and TSEV alone and require therefore a quick recharge of the CST to provide additional system capacity. $OM = 3$ has the drawback of previously mentioned COP drawback due to the ice tank charge / discharge. If the additional operation of the AHU is required during $OM = 3$, $OM = 6$ is activated, which extends $OM = 3$ by the operation of the AHU. $OM = 6$ is shown in Figure 3.10b.
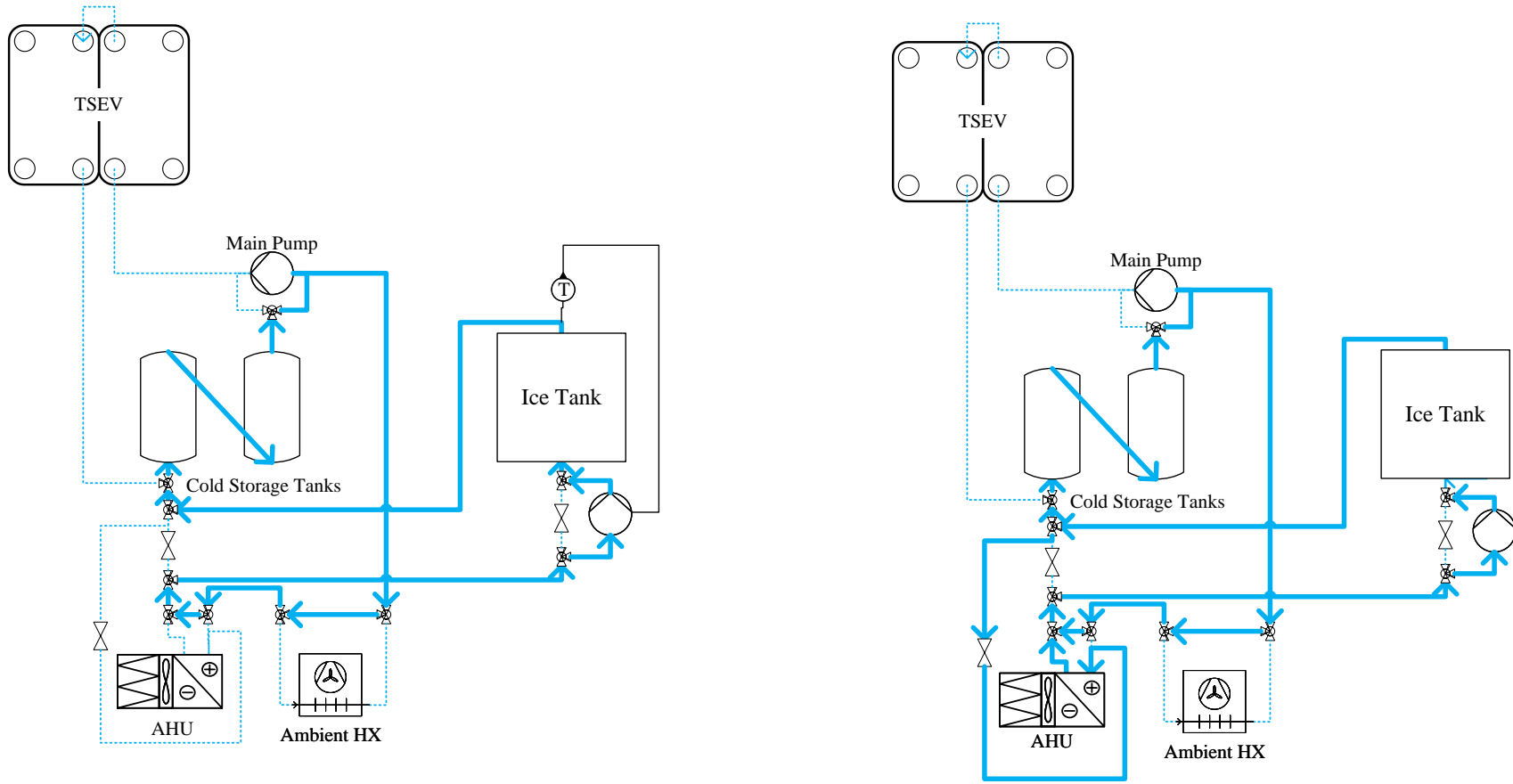
(a) Operation Mode 2: Cold Water Storage Tank Charging through the Ice Tank utilizing the Ice Tank Pump

(b) Operation Mode 5: Cold Water Storage Tank Charging through the Ice Tank utilizing the Ice Tank Pump with AHU operation

Figure 3.9: Additional Hydronic Subsystem Operation Modes 1/2
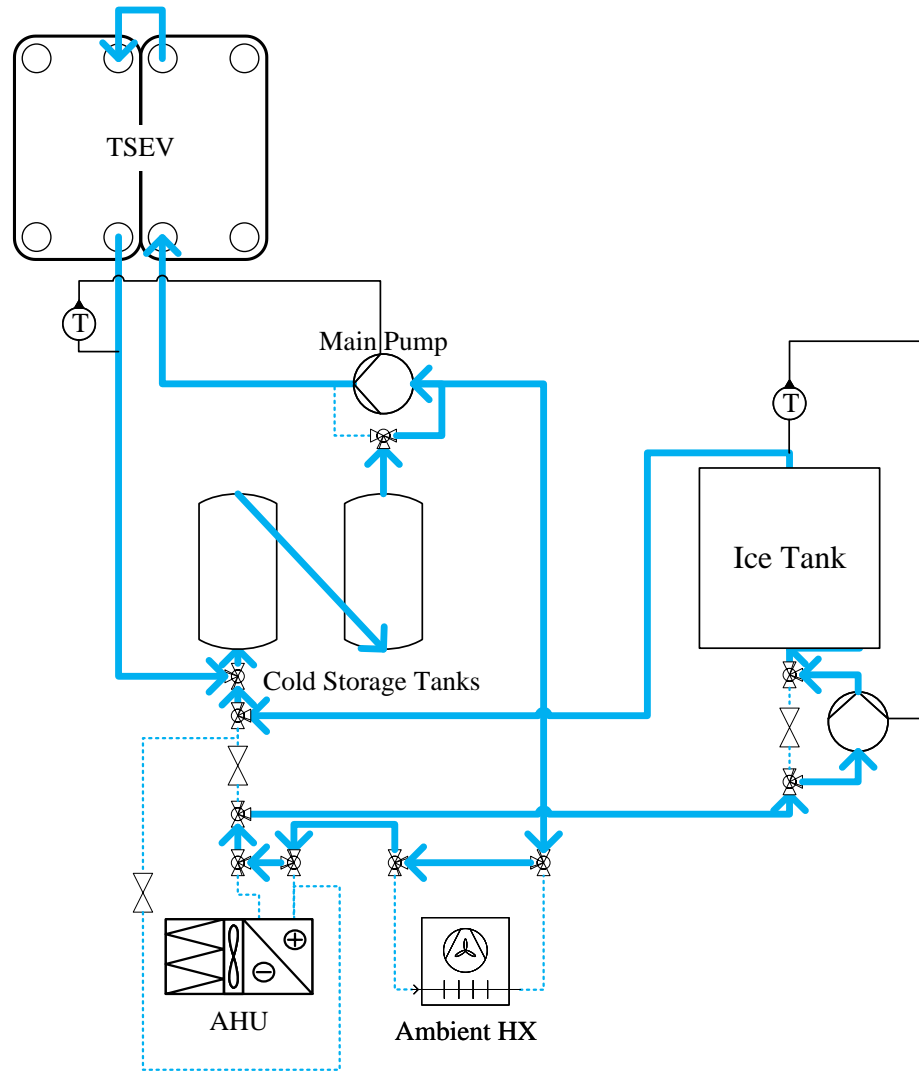
(a) Operation Mode 3: Cold Water Storage Tank Charging through the TSEV and Ice Tank
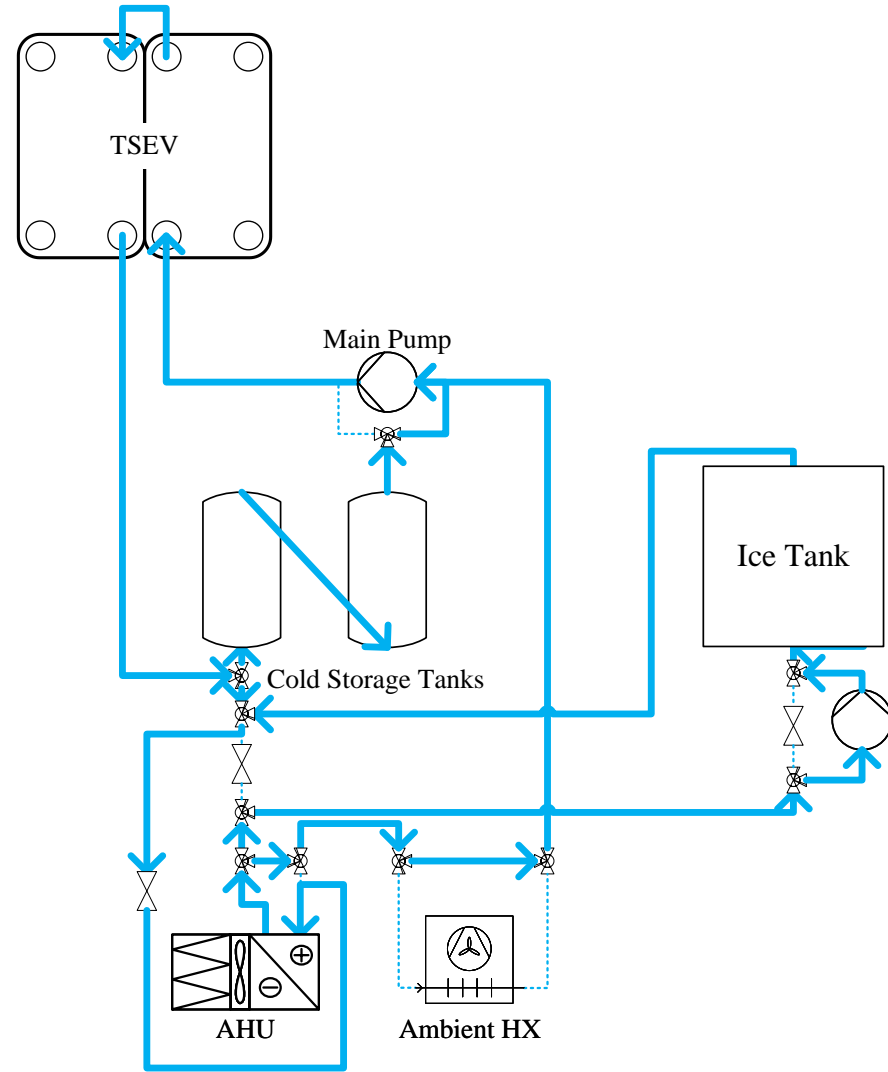
(b) Operation Mode 6: Cold Water Storage Tank Charging through the TSEV and Ice Tank with AHU operation

Figure 3.10: Additional Hydronic Subsystem Operation Modes 2/2

3.3   System Control

As presented in the sections above, the system consists of the following subsystems: the heat pump system, hydronic system as well as the air control volume. These subsystems are interconnected, as presented in Figure 3.11.
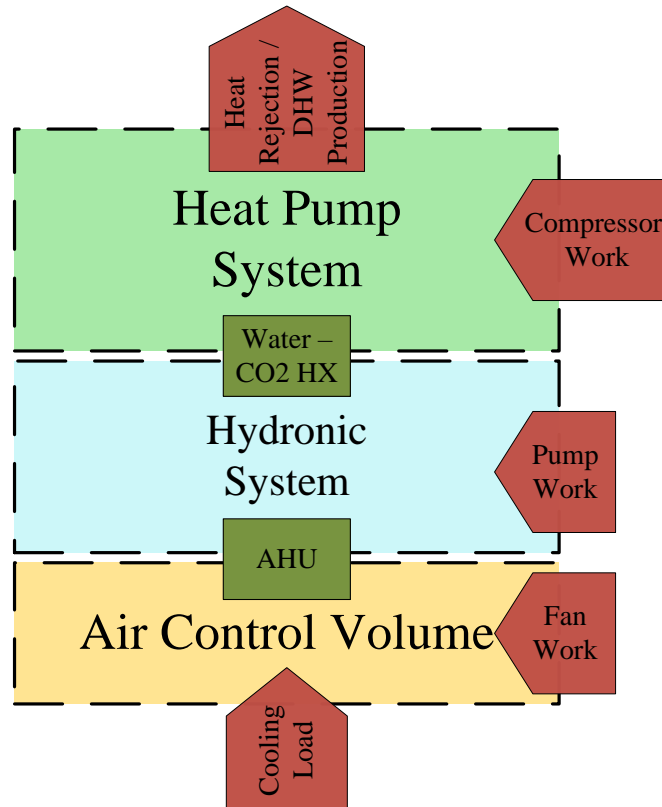
Figure 3.11: Simplified Schematic System Overview

The cooling load, which can be produced for example due to technical equipment, people, kitchen, etc. is heating up the air volume. In case the temperature rises above a certain boundary value reacts the hydronic subsystem by cooling the air within the control volume using the AHU. Cooling can be provided as presented before by the different operation modes from chapter 3.2.1 and 3.2.4.

If the control strategy requires the operation of the two-stage evaporator or the charging of the ice tank, the heat pump system will operate, as well as if the cold water storage tanks or ice tanks need to be charged. Hence, the operation strategy of the hydronic system acts as the main controller of the heat pump and hydronic system, and is influenced by the cooling demand on the air control volume.

The control strategy for the hydronic subsystem is based on the operation strategy of an ice tank CTES presented in the 2015 ASHRAE handbook[24], which adapts an ice tank charging and discharging strategy from Drees & Braun[25]. The ice tank operation strat-

egy developed by Drees & Braun[25] is a rule-based optimal control strategy[25]. Since the presented strategy by ASHRAE[24] only includes an ice tank as CTES, the control strategy needs to be adapted for the combined use of cold water storage tanks and ice tanks. The control strategy differentiates between operation during the on-peak and off-peak period. Within the off-peak period, the TES is set to charge, since the control strategy assumes lower system loads and possibly lower electricity rates. During the on-peak period is the TES discharged or neutral and the CO_2 heat pump system operated if required. The operation strategy is determined periodically and the process activated by the parameter "Decision Activation".

The off-peak period part of the control strategy charges the ice tank and cold water storage tanks continuously. The corresponding operation mode for cold water storage tank charging is $OM = 1$, and as previously mentioned are the ice tanks charged independently of the operation mode. If a load on the air handling unit is present, the OM changes from $OM = 1$ to $OM = 4$ to cover the AC load. $OM = 1$ corresponds to CST charging only, and $OM = 4$ corresponds to CST charging with AHU operation.
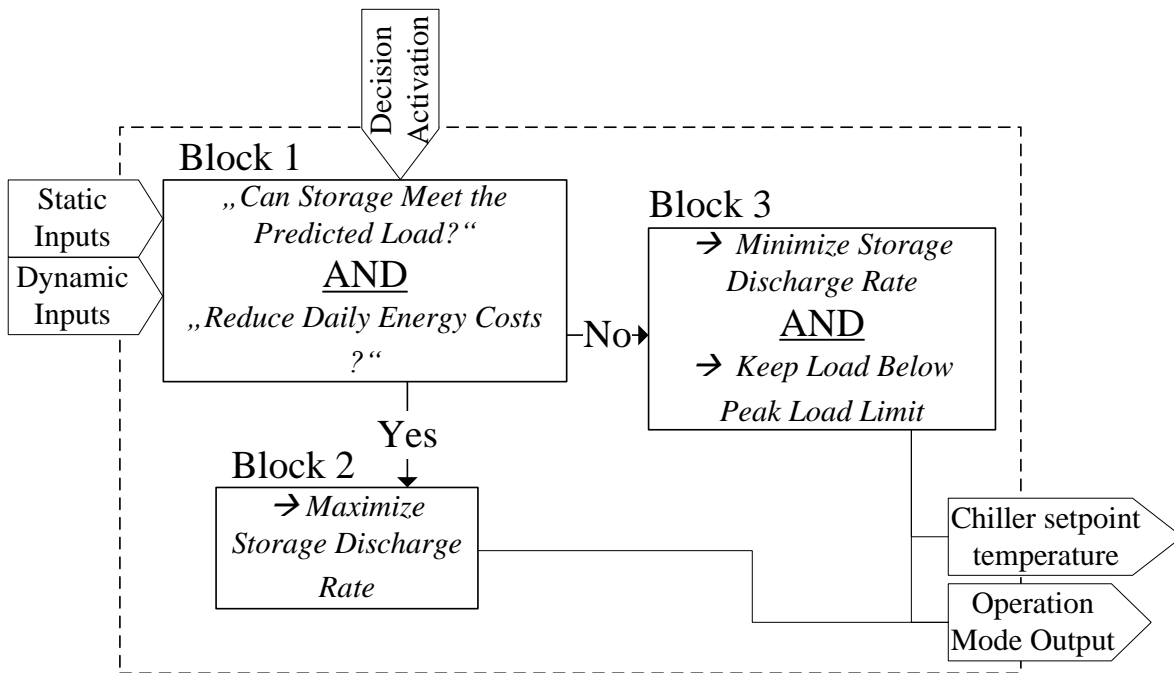
Figure 3.12: Discharging Part of the Adapted Control Strategy based on the 2015 ASHRAE Handbook[24]

The TES discharging part of the control strategy, which operates during on-peak hours, consists of the following three segments, as illustrated in Figure 3.12:
Block 1 determines if the storage discharge rate should be maximized (Block 2) or minimized (Block 3). Depending on the result of Block 1, either Block 2 or Block 3 is activated

and determines which of the operation strategies from chapter 3.2.2 - 3.2.3 should be used. The operation strategy determines the required operation mode, as well as the two-stage evaporator water exit temperature, as an output.

Based on the determined operation strategy, the valves are positioned accordingly and pump controllers are activated or deactivated. Furthermore, the control strategy is communicated to the heat pump control, which operates the two stage evaporator and LT compressor according to the demand. The following paragraph presents Block 1 - Block 3.

Block 1:
As mentioned previously, Block 1 decides whether the discharge rate of the TES should be maximized or minimized. Therefore, Block 1 holds the following criterion based on the 2015 ASHRAE Handbook[24]:

$$ECR > (COP_d/COP_c) \;\&\&\; (X - X_{min}) \cdot C_s \geq Q_{load,acc} \tag{3.1}$$

It first asks whether the associated energy costs of discharging the storage are lower than the direct use of the chillers[24]. If the first part of the criterion is fulfilled, it is then checked if the remaining storage capacity is sufficient to meet the predicted demand within the on-peak period[24]. In case the criterion from equation 3.1 is fulfilled, Block 2 is activated and the storage is used to its maximum capacity. If the criterion does not hold, Block 3 is activated to minimize the storage discharge rate.

Block 2:
Block 2 maximizes the utilization of the CTES and is as mentioned above activated by Block 1. Block 2 (as well as Block 3) utilize an input that determines whether additional cooling capacity is required (named *CID - capacity increase / decrease*). The input *CID* is in the form of an integer and has for Block 2 a range of 1-3. As mentioned previously, the discharge of the cold water storage tanks is preferred over the discharge of the ice tanks due to the energy efficiency reasons. An overview over Block 2 is shown in Figure 3.13.

Therefore, for the lowest system capacity demand ($CID = 1$), which is covered by only the CTES, the discharge of the cold water tanks is preferred (operation mode 12), and the ice tank discharge is only activated when the SOC of the cold water storage tanks is below 5 % (operation mode 8).
If the CID variable is increasing to $CID = 2$, the operation mode is changed to operation mode 14 and the discharge of the ice tank is used for providing additional cooling capacity. The ice pump is off in this configuration and water from the CST can flow by distribution
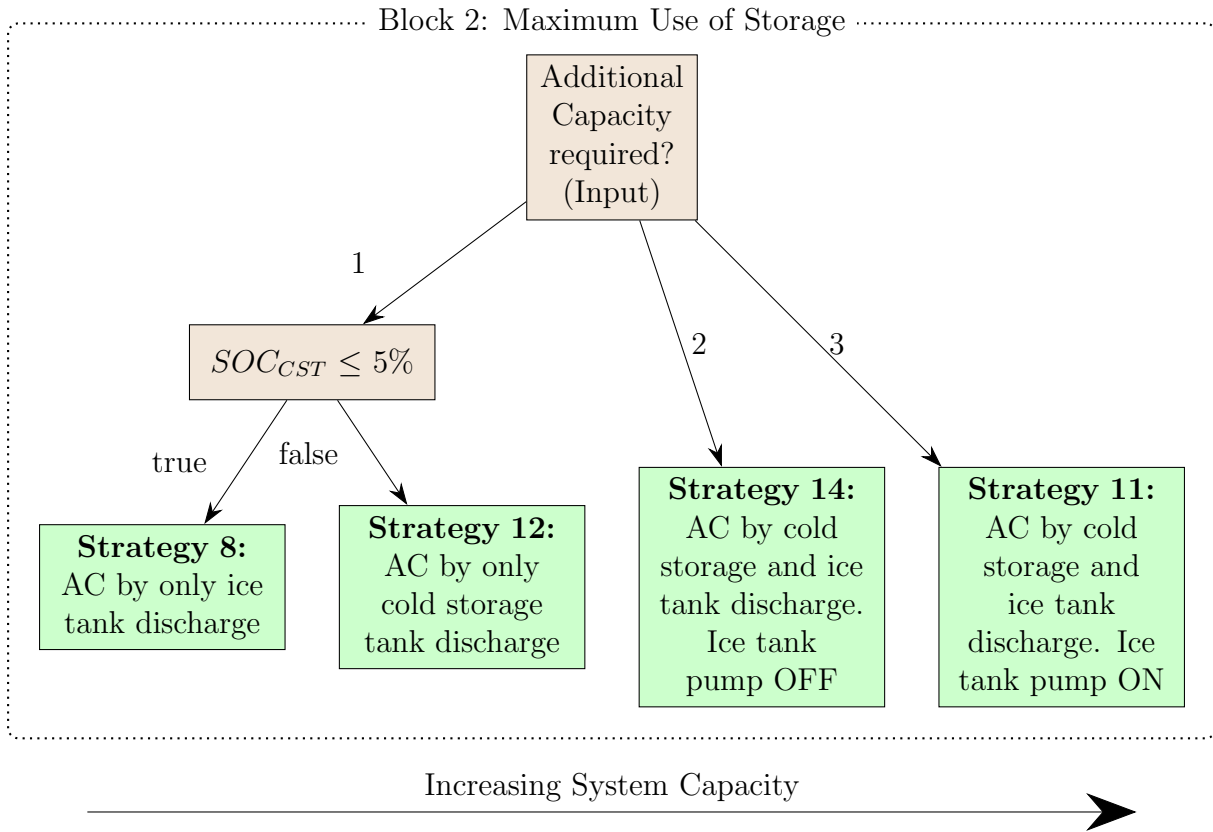
Figure 3.13: Block 2 of the Adapted Control Strategy adapted from the ASHRAE Handbook[24]

of valve V3 through the ice tank or bypass it. If the cooling capacity is still not sufficient, and CID increases to $CID = 3$, the operation mode is changed to $OM = 11$ and the ice tank is discharged by the ice tank pump using the return water of the AHU additionally to the CST discharge.

Block 3:

Block 3 minimizes the CTES discharge rate and therefore maximizes the use of the TSEV. Similar to Block 2, it takes the CID value as an input to determine which operation mode should be utilized at the current situation, and an overview over Block 3 is shown in Figure 3.14

In case the current CID value is $CID = 1$, operation mode $OM = 7$ is chosen, which covers the AC cooling demand by only the TSEV. For the cases where the operation of only the TSEV is not sufficient to meet the AHU cooling demand, CID increases to $CID = 2$ and $OM = 10$ is chosen. In $OM = 10$ operates the TSEV at its design conditions, and the additional demand is covered by the CSTs. In case the combination of operating the TSEV and the CST is not sufficient, then the AC cooling demand is met by operation mode $OM = 15$ at $CID = 3$, which features the simultaneous discharge of the CST and ice tank, as well as the operation of the TSEV. The ice tank pump remains off in this
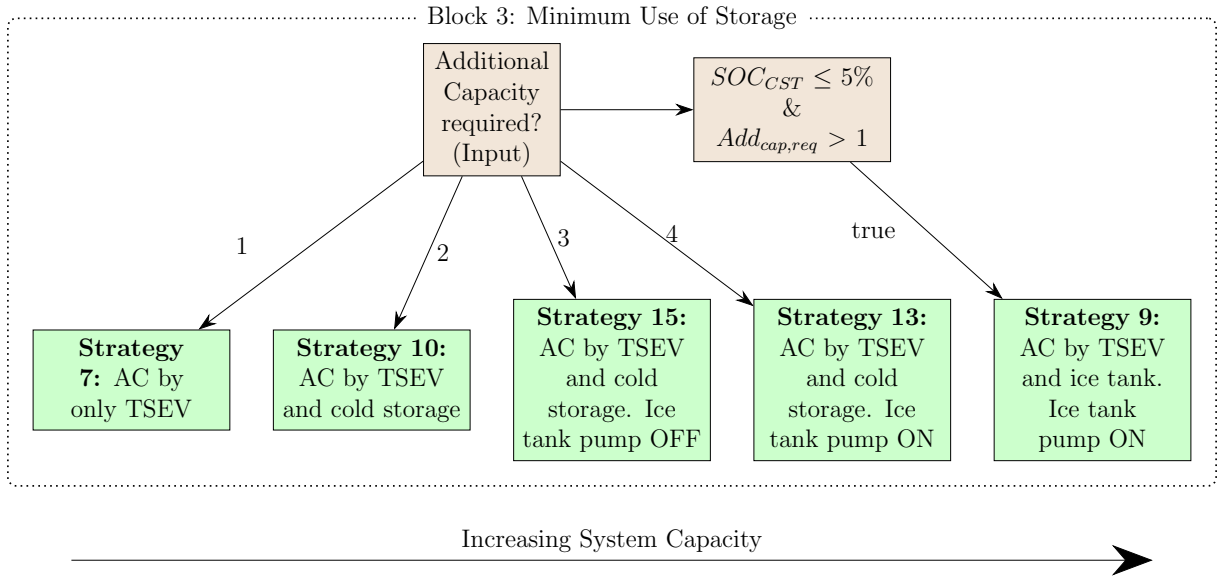
Figure 3.14: Block 3 of the Adapted Control Strategy adapted from the ASHRAE Handbook[24]

configuration and the flow through the ice tank is regulated by Valve 3.

For further capacity increases, the system can operate in operation mode $OM = 13$, which includes similar to operation mode 15 the use of the TSEV, CST and ice tank by increasing the flow rate by utilizing the ice pump.

For the case that the CST run dry, and additional capacity is required, operation mode $OM = 9$ is activated where the AC cooling demand is met by the TSEV and the ice tank with the ice tank pump on.

For the calculation of the chilled water setpoint temperature, the following algorithm from the 2015 ASHRAE handbook[24] is used:

1. Load for Load Limiting Operation:

$$\dot{Q}_{LLC} = max\left(\frac{Q_{load,occ} - (X - X_min) \cdot C_s}{\Delta t_{on}}, \dot{Q}_{ch,min}\right) \tag{3.2}$$

2. Calculating the chiller target cooling load:

$$\dot{Q}_{ch} = min\left(\dot{Q}_{load}, max\left(\dot{Q}_{LLC}, \dot{Q}_{ch,peak}\right)\right) \tag{3.3}$$

3. Calculating the chiller target supply temperature:

$$t_{chws} = max\left(t_{chwr} - \frac{\dot{Q}_{ch}}{c_{p,w} \cdot \dot{m}_{w,ch}}, t_c oil\right) \tag{3.4}$$

If Block 3 is activated, an activation signal to the heat pump signalises that the heat pump needs to operate and meet the calculated supply temperature of the chilled water t_{chws} exiting the TSEV.

4   Methodology

The following chapter presents the methodological approach in chapter 4.1 and furthermore, the model created in the simulation software Dymola.

4.1   Methodological Approach

The aim of the thesis is to investigate a novel CO_2 heat pump / hydronic AC system setup that includes the TSEV with TES in the form of cold water storage tanks and an ice tank to cover the AC load. Due to the interaction between the system components and the resulting operation modes, the dynamic system behaviour is of greater interest than steady state operation. Hence, a model of the system is required that allows dynamic simulations to investigate the system performance and behaviour.

Dymola with modelica as the modelling language is used as the simulation tool. Dymola as a simulation tool is capable to handle complex simulation models, and is used within e.g. automotive and aerospace engineering, robotics, ... [26]. Furthermore, Dymola offers the advantage of accessible source code with the an easy implementation of user defined models[26]. For the modelling of refrigeration processes, the TIL Suite contains an external library to be used within modelica, which includes pre-defined models of refrigeration system components, such as compressor, heat exchangers, etc. The TIL Suite consists of several sub-libraries and tools, which include for example the system components (TIL) and a database of thermophysical properties of different fluids (TIL-Media)[27]. Due to the pre-defined models, their source-code accessibility and possibility to extend and adapt the models is the TIL-library chosen as the main modelica library to be used within the simulation.

Once the model is built within Dymola and the different sub-models are established is an exemplary AC load posed onto the system. The system behaviour and consequently the results are gained through the simulation in Dymola and are analysed within the software.

Due to the novelty of the system is a verification of the entire model against experimental data not possible, since a physical system does not exist. Furthermore, a verification of the different sub-models, which are presented in the following chapters, is due to the limited time frame of the master thesis not possible. Prior to final conclusions should a verification be carried out, to obtain insights on the correctness of the gained results. Hence, the results gained within this work can only be regarded as preliminary and as a proof of concept instead of final system results.

4.2 Overall Model Structure

The entire model is shown in Figure 4.1 and consists of the model of the system on the right, and its inputs, control system and result variables on the left. The workflow of the simulation operates the following way:

Key system parameters, e.g. sizing of the ice tank and cold storage water tanks, setpoints, etc., are entered within the green input block on the left. Those parameters are fed to the corresponding component / control block. Certain constant component sizes (e.g. tube sizes, heat exchanger sizes, etc.) are entered within the right side model directly.

Based on the input parameters and measurements from sensors, the system control determines the operation strategy, as presented in chapter 3.3, as well as the setpoint temperature of supply water from the TSEV t_{chws}. The determined operation strategy and variables are communicated to the corresponding components and controllers.
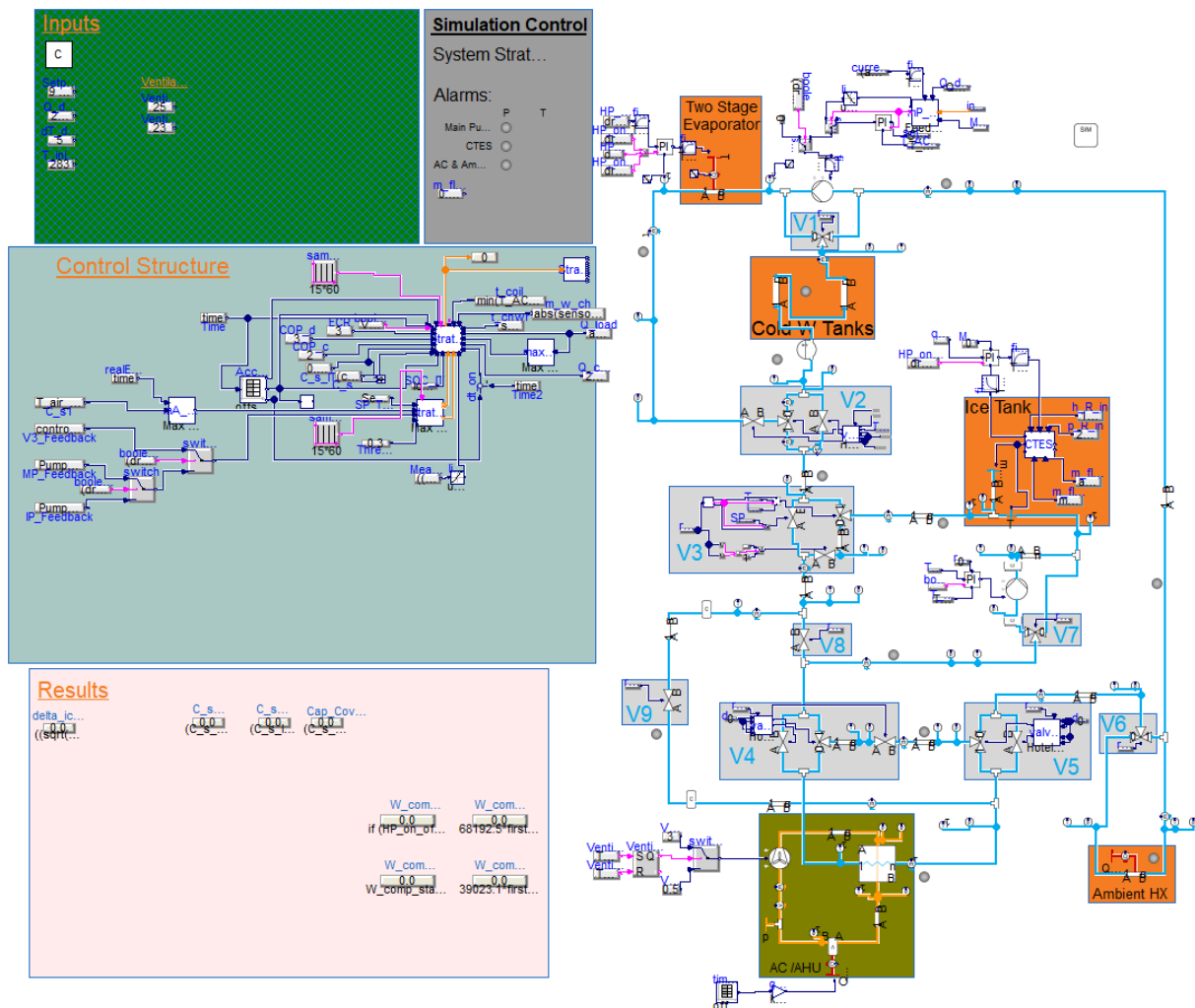
Figure 4.1: Overview of the entire Dymola Simulation Interface

The right part of the simulation represents the physical system. The AHU subsystem, including the water to air heat exchanger, is located at the bottom. Grey boxes represent

valves V1-V9 and are connected as shown in chapter 3. The orange boxes represent heat exchangers or thermal energy storage components (excluding the AHU). The ambient heat exchanger can be seen in the lower right corner, the ice tank as well as the cold water storage tanks in the middle, and the two stage evaporator at the top. Heat exchange in the TSEV and ambient heat exchanger is implemented as a tube connected to a heat boundary. Thereby, the transferred heat affects the discretized cells of the tube as an external heat flow.

Tubes are placed between the components, as they are not only physically present in an installed system but also act as a buffer and to a certain extent as a damping by the induced pressure drop during fluid flow. Tube sizes are exemplary and range between $l = 1 - 15 \, \text{m}$ at $d = 0.05 \, \text{m}$.

The sizing of the different components is presented in chapter 5.2.1 prior to the initial simulation.

4.3 Sub-Model Construction

Several sub-models have to be individually built due to the unavailability of pre-defined models or to limit the computational complexity of the simulation. This includes the control volume sub-model, the ice tank model, and the TSEV model, which are described in the following chapters.

4.3.1 Control Volume Sub-Model

The AC load is posed onto a control volume, which can be seen in Figure 4.2. The control volume represents the volume of the "real-world" application, e.g. the volume of a hotel or fish production facility. It is assumed that the total AC demand acts on one air volume and thereby increases its temperature. The AC load is in this case implemented as a heat source using the shown heat boundary, which offers the implementation of different demand profiles.

To maintain temperatures that are within acceptable (indoor) conditions is the control volume connected to an air-to-water heat exchanger, which represents the air handling unit (AHU). Air is circulated using a fan, which operates using an on-off control by a RS FlipFlop block. The fan has a high and a low volume flow $\dot{V}_{air,sp}$ setpoint setting. $\dot{V}_{air,sp,high}$ is turned on when the temperature of air that exits the control volume exceeds an upper threshold value, and the lower volume flow of air $\dot{V}_{air}$ is turned on whenever the air exiting the control volume exceeds a lower threshold value. Thereby, the temperature is maintained between the upper and lower threshold value, if the AHU can cover the necessary cooling demand and the volume flow of the fan is sufficient. To encounter
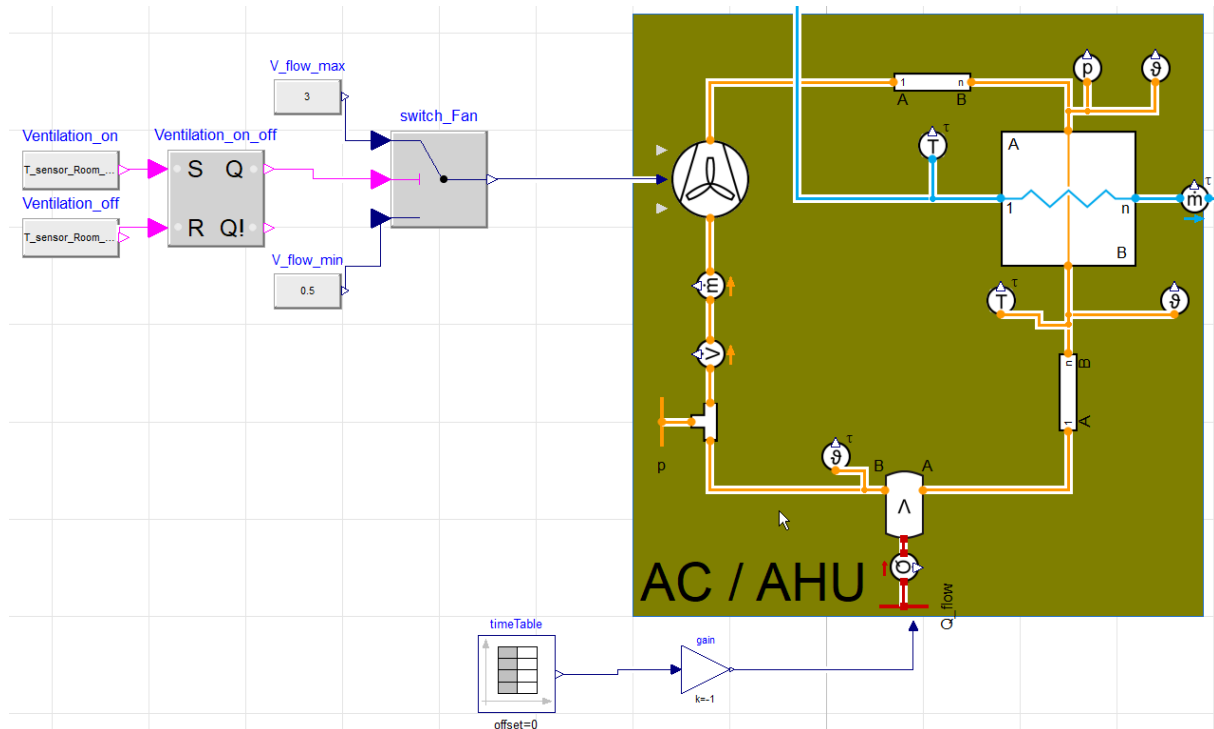
Figure 4.2: Control Volume Sub-Model within Dymola

pressure changes due to temperature induced density changes within the air system is the air volume connected to a pressure boundary that maintains the pressure within the air volume at atmospheric pressure.

4.3.2 Ice Tank Unit

The ice tank consists of the in Figure 3.2 shown principle of vertical tubes running through the water tank. Within the tubes, CO_2 evaporates due to heat transfer from the water to the CO_2 . Hence, ice formation occurs around the tubes.

A simplified ice tank model is built from the ground up, since no ice tank model with the proposed working principle was available. The simplified ice tank model splits the ice tank into horizontal cells, which is described by the parameter *nCells*. Within each cell, the fluid properties are assumed to be constant and uniform. Furthermore, the following assumptions are made:

- Buoyancy forces within the water and CO_2 cell are negligible

- Uniform distribution of flow & temperature within the water cell

- Vertical heat conduction within the ice is negligible

- Constant heat transfer coefficients on the water and refrigerant side

- If there is refrigerant flow and in the case that no ice formation occurs, it is assumed that the outside of the tube is at $T = 0°C$

- Ice front formation is independent of the adjacent ice fronts

- Only the fusion enthalpy of water is considered to store energy, hence no sensible heat storage within ice is considered

Each horizontal cell consists of three sub-cells, a CO_2, ice and water sub-cell, as Figure 4.3 shows. Each sub-cell contains the entire media mass of the horizontal cell, and the geometry of the tank is represented within the heat transfer and fluid mass calculations. The heat transfer equations calculate the heat transfer to the outer ice surface / ice front, since the temperature is known to be at $T_{ice,surface} = 0°C$. Figure 4.4 shows the geometry details of a cut-out from the ice tank to illustrate important parameters.
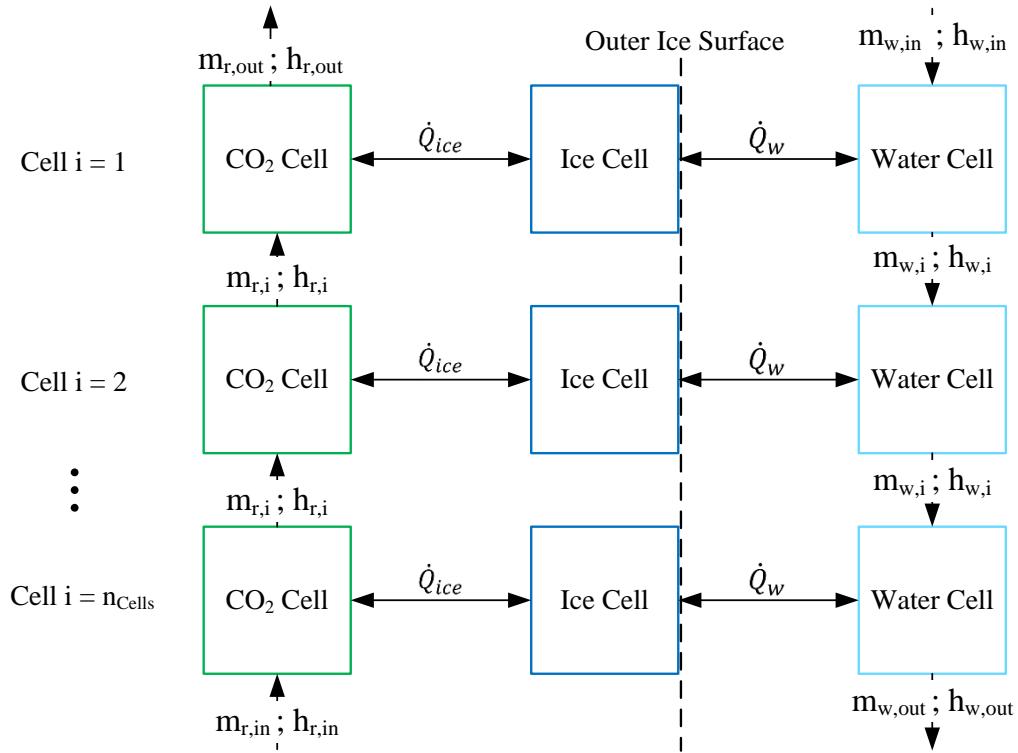
Figure 4.3: Discretization, Fluid Flow and Heat Transfer Mechanisms of the Ice Tank Model
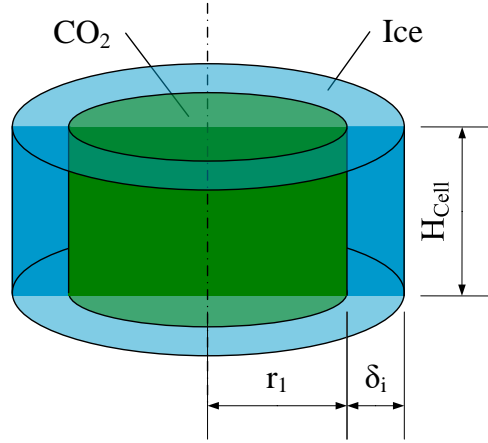
Figure 4.4: Geometry Detail of Ice Formation around the Tube within the Ice Tank

The following section presents the governing equations of the ice tank in equation 4.1 - 4.13. The governing equations are presented with the node $_i$, which corresponds to the cell number.

Initial Equations:

$$\delta_i = \delta_{i,init} \tag{4.1}$$

$$h_{w,cell,i} = h_{w,i}(T_{w,cell,i}) \tag{4.2}$$

$$h_{r,cell,i} = h_{r,in} \tag{4.3}$$

Water Cell Equations:

Mass of the water cell:

$$m_{w,cell,i} = (H_{cell} \cdot D_{tank} \cdot W_{tank} - n_{tubes} \cdot \pi \cdot \left((r_1 + \delta_i)^2\right) \cdot H_{cell}) \cdot \rho_{w,i} \tag{4.4}$$

Energy Balance of water cell:

$$\frac{\partial h_{w,cell,i}}{\partial t} \cdot m_{w,cell,i} = -\dot{Q}_w + \dot{m}_w \cdot (h_{w,cell,i-1} - h_{w,cell,i}) \tag{4.5}$$

Mass flow in water cells:

$$\dot{m}_{w,i} = \dot{m}_{w,i-1} + (\rho_{w,i} - \rho_{ice}) \cdot \frac{\dot{Q}_{st,i}}{\Delta h_{fus} \cdot \rho_{ice}} \tag{4.6}$$

Ice Cell Equations:

44

Stored Energy in ice:

$$Q_{st,i} = \Delta h_{fus} \cdot \rho_{ice} \cdot \pi \cdot H_{cell} \cdot n_{tubes} \cdot \left((r_1 + \delta_i)^2 - r_1^2\right) \tag{4.7}$$

Ice surface energy balance:

$$\dot{Q}_{st} = \dot{Q}_{ice} - \dot{Q}_w \tag{4.8}$$

Refrigerant Cell Equations:
Mass of refrigerant cell:

$$m_{r,cell,i} = \left(n_{tubes} \cdot H_{cell} \cdot \pi \cdot (r_1 - \delta_{tube})^2)\right) \cdot \rho_{r,i} \tag{4.9}$$

Energy Balance of refrigerant cell:

$$\frac{\partial h_{r,cell,i}}{\partial t} \cdot m_{r,cell,i} = \dot{Q}_{ice} + \dot{m}_r \cdot (h_{r,cell,i+1} - h_{r,cell,i}) \tag{4.10}$$

Mass flow in refrigerant cell:

$$\dot{m}_{r,i} = \dot{m}_{r,i} - \frac{\partial m_{r,cell,i+1}}{\partial t} \tag{4.11}$$

Heat Transfer Equations:
The heat transfer equations are adapted from Incropera et al.[28]. The heat transfer from the water cell to the outer ice surface is calculated by:

$$\dot{Q}_{w,i} = \alpha_{w,i} \cdot 2\pi \cdot \left((r_1 + \delta_i)^2 - r_1^2\right) \cdot H_{cell} \cdot (T_{w,cell,i} - T_{0,i}) \tag{4.12}$$

Heat transfer from refrigerant to outer ice surface:

$$\dot{Q}_{ice,i} = \frac{(T_{0,i} - T_{r,i})}{\frac{1}{2 \cdot \pi r_1 \cdot H_{cell} \cdot \alpha_{r,i}} + \frac{log(\frac{r_1 + \delta_i}{r_1})}{2\pi \cdot k_{ice} \cdot H_{cell}}} \tag{4.13}$$

The governing equations are implemented as a *"block"* class in Modelica within the equations section. The modelica code of the ice tank model is attached in appendix A.2.

The implementation of the ice tank model is shown in Figure 4.5. On the refrigerant side requires the model the inputs of the mass flow $\dot{m}_{R,in}$, the enthalpy $h_{R,in}$ and the pressure $p_{R,in}$ of the refrigerant. By an attached PI controller is the mass flow of refrigerant controlled to exit the ice tank at a vapour quality of $x = 1$.

The controller is turned on whenever the current operation mode is $OM = 1$. On the

water side requires the model the water mass flow $\dot{m}_{w,in}$ and the inlet temperature $T_{w,in}$ of water as the input variables. The water side pressure is assumed to be at atmospheric pressure $p_{atm} = 1.013\,\text{bar}$.
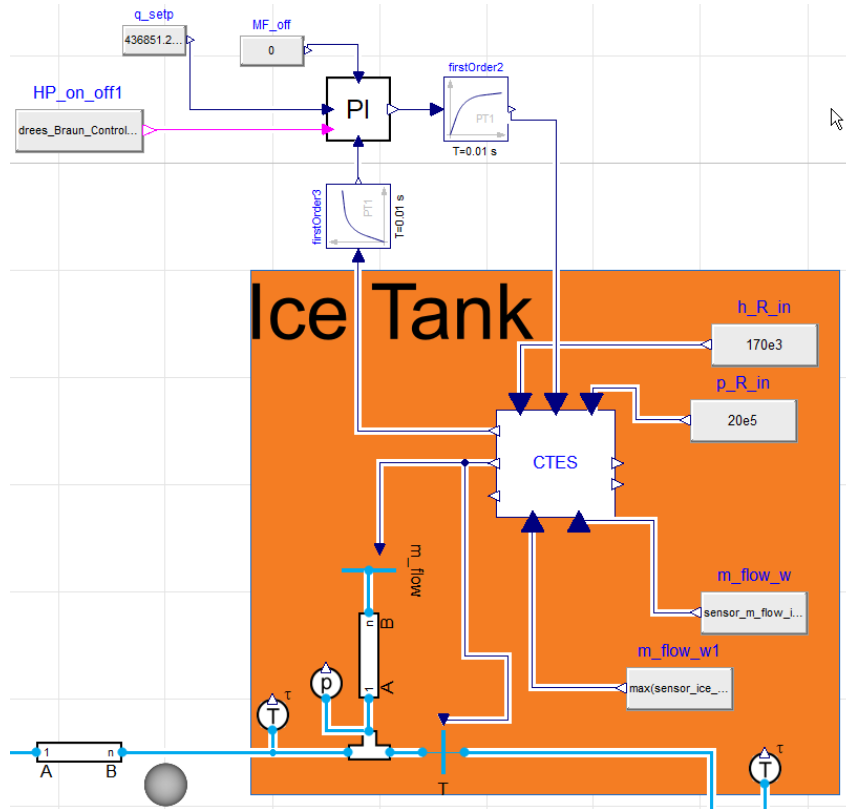
Figure 4.5: Ice Tank Model implemented within the Modelica Model in Dymola

The ice tank model calculates the enthalpy $h_{R,out}$ of the exiting CO_2 , the temperature of the exiting water $T_{w,out}$ and the mass derivative of water $der(\dot{m}_w)$ due to density changes while charging and discharging. The water exiting the ice tank is connected within the simulation to the hydronic sub-system by an inline boundary. The inline boundary allows to specify one flow variable and preserves the remaining variables and the flow variable is set to be temperature and is connected to $T_{w,out}$, which is calculated by the ice tank model.

The modelica code of the ice tank model uses conditional statements to implement geometrical boundaries, such as once all the ice layer covers the free cross sectional area of the tank, the heat transfer to the ice is set to $\dot{Q}_{st,i} = 0\,\text{W}$. This limits further build-up of the ice thickness since the interaction between ice-fronts is disregarded, as mentioned within the assumptions.

A key parameter is the state of charge per cell SOC_{cell}, which expresses the percentage to

which the cell is charged with ice. The SOC_{cell} is calculated using the following equation:

$$SOC_{cell,i} = \frac{(n_{tubes} \cdot \pi \cdot (\delta_i + r_1)^2) - (n_{tubes} \cdot \pi \cdot (r_1)^2)}{W_{tank} \cdot D_{tank} - (n_{tubes} \cdot \pi \cdot r_1^2)} \tag{4.14}$$

The state of charge of the entire ice tank SOC_{IT} is calculated as the average of $SOC_{cell,i}$ for $i = 1 \ldots n_{cells}$.

4.3.3 CO_2 Heat Pump

The following chapters present the model building of the CO_2 heat pump. Included is in chapter 4.3.3.1 the presentation of the two stage evaporator model and in chapter 4.3.3.2 the model utilized for the LT compressor.

4.3.3.1 Two Stage Evaporator

The TSEV part of the CO_2 heat pump system is approximated based on data of the TSEV configuration, which was calculated by Bengsch[29]. Bengsch[29] investigated the performance of the TSEV configuration with experimentally verified simulations. The data obtained by Bengsch[29] are three data sets of $T_{TSEV,in} = 9 - 18\,°C$ at a pressure of the ejector fed evaporator of $p_{EFE} = 35, 38\,\&\,41\,bar$ for a water mass flow rate of $\dot{m}_w = 0.6$ or $0.4\,kg\,min^{-1}$. The high pressure p_{GC} was set to $p_{GC} = 120\,bar$.[29]

Based on the data set by Bengsch[29], a non-linear regression is carried out. The compressor work is used as the response variables for the non-linear regression and the total evaporator load, water inlet and exit temperatures are taken as the predictor variables of the compressor work.

The built in function *fitnlm* in Matlab is taken as the tool to find the non-linear regression result. Equation 4.15 shows the functional form of the model and provided a higher accuracy than a polynomial or $\dot{W}_{comp} \propto \dot{Q}_{ev} \cdot T_{TSEV,in} \cdot T_{TSEV,out}$ approach.

$$\dot{W}_{comp} \propto \frac{\dot{Q}_{ev}}{(T_{TSEV,in} - T_{TSEV,out})} \tag{4.15}$$

The following section presents the result which is obtained through the non-linear regression in Matlab. $x2$ represents the evaporator load $\dot{Q}_{ev}$, $x1$ the two-stage evaporator inlet temperature $T_{TSEV,in}$ and $x3$ the two-stage evaporator outlet temperature $T_{TSEV,out}$. $b1$ - $b5$ are the corresponding coefficients that are determined by the non-linear regression.

```
Nonlinear regression model:
y ~ (x2^b4)/(b1*x1^b3 - b5*x3^b2)
```

```
Estimated Coefficients:
Estimate          SE          tStat          pValue

---------      --------      -------      ----------


b1      0.80206      0.39844       2.013       0.054576
b2       1.2483      0.30759       4.0583      0.00040152
b3     -0.32896      0.12395      -2.6539       0.013393
b4       0.7988      0.077956      10.247      1.2729e-10
b5     -0.012037     0.01056      -1.1399       0.2647



Number of observations: 31, Error degrees of freedom: 26
Root Mean Squared Error: 227
R-Squared: 0.991,   Adjusted R-Squared 0.99
F-statistic vs. zero model: 4.23e+03, p-value = 5.83e-37
```

Based on the determined coefficients, the non-linear regression model reads:

$$\dot{W}_{comp} = \frac{\dot{Q}_{ev}^{0.7988}}{\left(0.80206 \cdot T_{TSEV,in}^{-0.32896} - (-0.012037 \cdot T_{TSEV,out}^{1.2483})\right)} \tag{4.16}$$

The evaporator load is entered in kW and the temperatures are entered in °C. For the given data points by the data set of Bengsch[29], Figure 4.6 shows the deviation of the compressor work by prediction through the non-linear regression model to the calculated value by Bengsch[29].
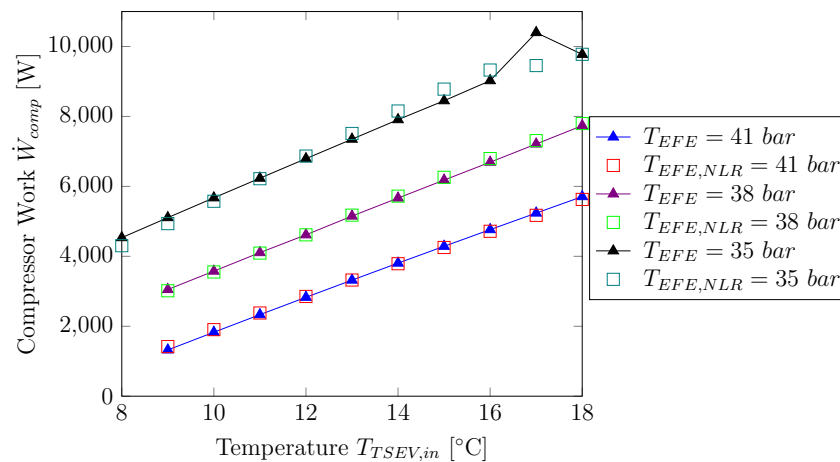
Figure 4.6: Simulated Compressor Work of TSEV Model calculated on Data by Bengsch[29] vs. Non-Linear Regression (NLR) Prediction

4.3.3.2   LT Compressor Model:

The compressor work related to the ice tank charging is approximated by a simplified two stage compression calculation. The intermediate pressure is set to $p_{IP} = 39$ bar, since

the liquid receiver of the TSEV system operates at pressures near $p_{IP} = 39 \, \text{bar}$. The LT compressor compresses CO_2 from the ice tank pressure to the intermediate pressure p_{IP}. The MT compresser unit compresses vapour state CO_2 further from the intermediate pressure p_{IP} up to the gas cooler pressure level of $p_{GC} = 120 \, \text{bar}$. It is assumed that the mass flow leaving the LT compressor is cooled down by the desuperheating heat exchanger and enters the MT section at $\Delta T_{SH} = 5 \, \text{K}$ superheat. Both compression stages are approximated with an isentropic efficiency of $\eta_{is} = 0.7$, with the isentropic efficiency being defined by Equation 4.17, based on Hafner & Eikevik[30].

$$\eta_{is} = \frac{h_{2s} - h_1}{h_2 - h_1} \tag{4.17}$$

Indices $_1$ refers to the state entering the compressor and $_2$ exiting the compressor. The compressor work of the LT and MT compressor unit due to the ice tank charging is calculated based on Eq. 4.18.

$$\dot{W}_{comp} = \dot{m} \cdot (h_2 - h_1) \tag{4.18}$$

While simultaneous operation of the TSEV and ice tank charging, the MT compressor work is defined as the sum from the MT compressor.

4.3.4 Cold Storage Tank Modelling

The cold water storage tanks are modelled by using the pre-defined class *Tube* within the TIL-Suite and tank sizes are defined within chapter 5.2.1. Furthermore are the following assumptions made:

- No heat loss through the walls of the tanks

- Linear pressure drop of $\Delta p_{nominal} = 0.01 \, \text{bar}$ at $\dot{m}_{nominal} = 1 \, \text{kg} \, \text{s}^{-1}$

- Buoyancy is neglected within the water.

- Ports are located at the highest and lowest point of the tank

- Due to the port location, no dead volume is present

The state of charge SOC_{CST} is calculated based on the following Equation 4.19. The operating range of the cold storage tank is assumed to be between $T_{CST} = 4 - 12 \, °\text{C}$. $T_{CST} = 4 \, °\text{C}$ is set as the lower limit, since at $T \approx 4 \, °\text{C}$, the local maxima of the water density occurs, based on the Engineering Equation Solver (EES)[31]. At lower temperatures, the density would decrease and the stratification of the tanks may not be preserved. Temperatures larger than $T > 12 \, °\text{C}$ are assumed to be too high for the simulated appli-

cation.

$$SOC_{CST} = \frac{\sum_{i=1}^{n_{Cells}} m_i \cdot c_{p,w} \cdot (12\,°\mathrm{C} - T_i)}{m_{tank} \cdot c_{p,w} \cdot (12\,°\mathrm{C} - 4\,°\mathrm{C})} \tag{4.19}$$

$$SOC_{CST} = \frac{\sum_{i=1}^{n_{Cells}} m_i \cdot c_{p,w} \cdot (12\,°\mathrm{C} - T_i)}{50} \tag{4.19}$$

4.4 Operation Strategy Determination and Communication

This chapter presents the strategy determination and communication of the corresponding operation modes within the system. The presented rule-based optimal control strategy from chapter 3.3 is implemented within the entire model, as Figure 4.7 shows.

The "Hydronic AC System General control block" in Figure 4.7 takes the inputs as presented from chapter 3.3, with the assumption that $COP_d/COP_c > ECR$ is always true. Hence, the strategy determination is only dependent on the SOC of the cold water storage tanks and ice tank. The "Hydronic AC System General control block" is connected to an additional block, called "Capacity decrease/increase", which evaluates whether an operation mode with a higher maximum system capacity is required. Based on its inputs, the "Hydronic AC System General control block" evaluates the required system strategy every 15 min and communicates the operation mode to the "operation mode control block". The "operation mode control block" communicates to the individual valve codes and/or valve positions, which changes the positions of the valves and changes the controller settings of regulated valves. Details of the valve control are presented in chapter 4.5.1.

The operation of the ice tank pump (IP) and the main pump (MP) are as well dependent on the operation strategy and are therefore connected to the "operation mode control block" as well.
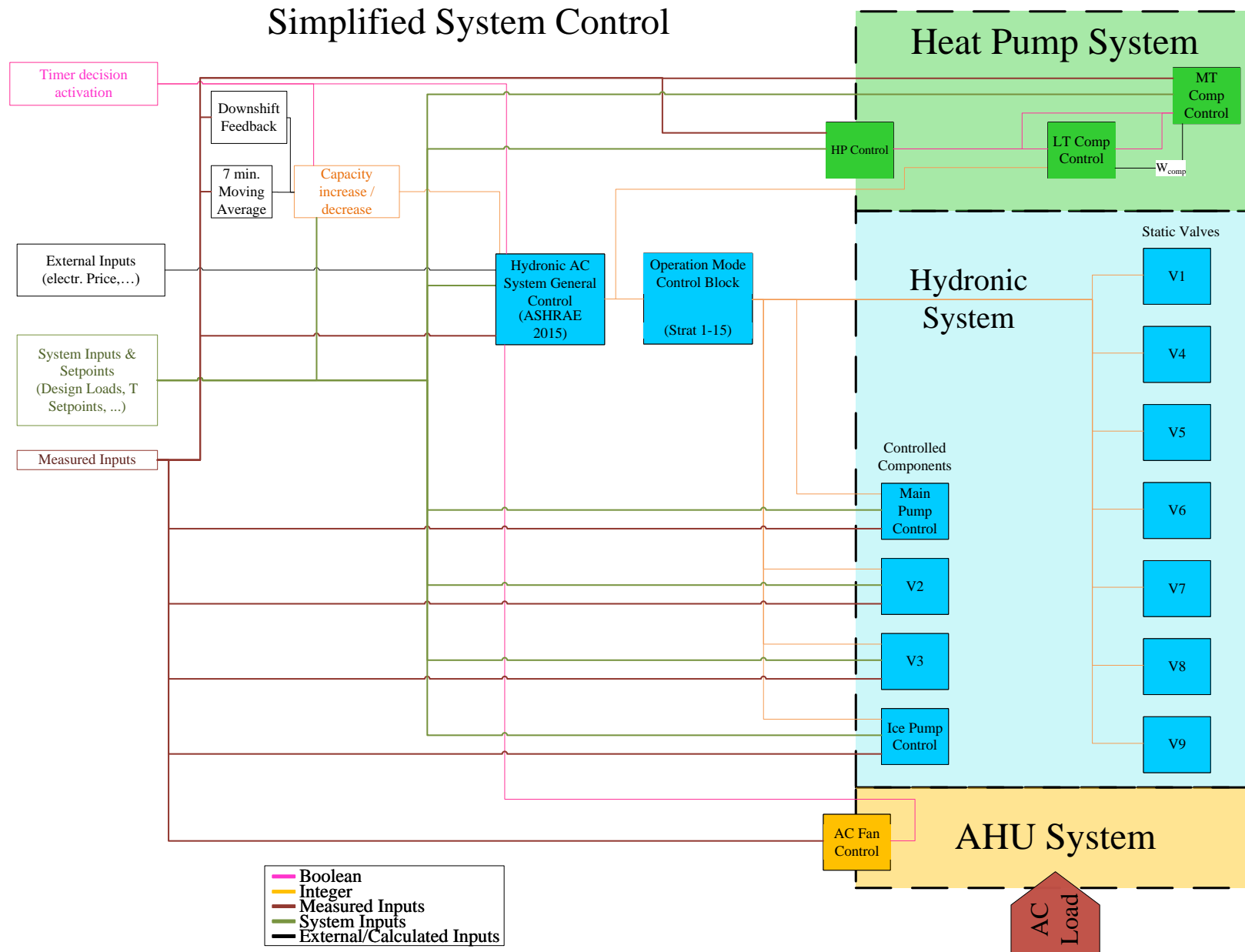
Figure 4.7: Simplified Overview over the Information Flow within the System Control Structure

Charging of the Thermal Energy Storage:

During the charging process of the TES, which occurs during the off-peak hours, are the cold storage tanks and the ice tank charged, combined with the occasional operation of the AHU. This is expressed in the operation modes $OM = 1$ and $OM = 4$, which correspond to CST charging and CST charging + AHU operation, respectively. Hence, the charging of the ice tank is not directly depicted in $OM = 1$ and $OM = 4$, and an additional control structure needs to be implemented.

As the simultaneous charging of the CST and ice tank would lead to a large required compressor work, an attempt to reduce the required maximum MT compressor work, by implementing the following rule set:

1. If the operation mode changes from $OM = 1$ to $OM = 4$ (CST charging to CST charging + AHU operation) during the off-peak period, the charging of the ice tank stops to ensure a reduced MT compressor work. This is based on the assumption that potentially the work required for the AHU operation is larger than the charging process of the TSEV. The change in operation mode from $OM = 1$ to $OM = 4$ takes place if the volume flow of air is set to the higher setpoint by the RS FlipFlop block (see chapter 4.3.1).

2. If the operation mode is $OM = 1$, the charging of the CST is only allowed to start if the LT compressor load (calculated based on Eq. 4.18) is smaller than $\dot{W}_{LT,comp} = 10\text{kW}$. By setting this condition, the combined imposed MT compressor load of the TSEV and LT stage is limited.

The charging process of the ice tank ends as soon as the SOC_{IT} reaches $SOC_{IT} \geq 0.95$ by deactivating the PI controller that controls the mass flow of CO_2 through the ice tank. A maximum SOC_{IT} value lower than $SOC_{IT} < 1$ is chosen to ensure that flow through the ice tank is possible, since at a $SOC_{IT} = 1$, ice covers the entire cross sectional area and no water flow is possible. The charging of the CST similarly ends when the SOC_{CST} is $SOC_{CST} \geq 0.99$. Within the simulation, the MT pump stops operating once this condition is fulfilled and the operation mode is $OM = 1$.

Discharging of the Thermal Energy Storage:

During the discharging process of the thermal energy storage, which can occur within the on-peak period, is the exit temperature of air in the AHU controlled by either the main pump, V2, V3 or the ice tank pump. Hence, the present operation mode OM determines which component is active in controlling the supply air temperature. As shown in Figure 4.7, the "Hydronic AC System General control block" is dependent on the integer input from a block called "capacity increase / decrease". The "capacity increase / decrease block" determines whether an operation mode with higher total system capacity should

be activated. A higher system capacity is chosen if the average of the last seven measured temperatures of the control room with an interval of $\Delta t = 60$s between the measurements is higher than the setpoint temperature.

An operation mode with a lower overall system capacity is chosen once the currently controlling component of the supply air temperature is below 30 % of its maximum capacity, if the "Timer decision activation" is active.

4.5 Component Control

The following chapters present the control of valves and pumps.

4.5.1 Control of Valves

Passive valves within this simulation are defined as valves that are not individually controlled by a PI-Controller. The position of passive valves is changed according to the active operation mode by the "operation mode control block".

Active valves are defined as valves that are actively controlled by a PI controller or another dynamic control. For the regulation of active valves, the operation mode control block communicates valve codes, depending on the operation mode, to the active valve controller. Valve V2 can be seen in Figure 4.8 as an example of an actively controlled valve. To ensure the full desired functionality based on the different operation modes 1-15, are certain active valves set up by a three way valve (TWV), a bypass shut off valve (SOV) over the TWV, as well as an additional shut of valve in front of the three way valve (FSOV).
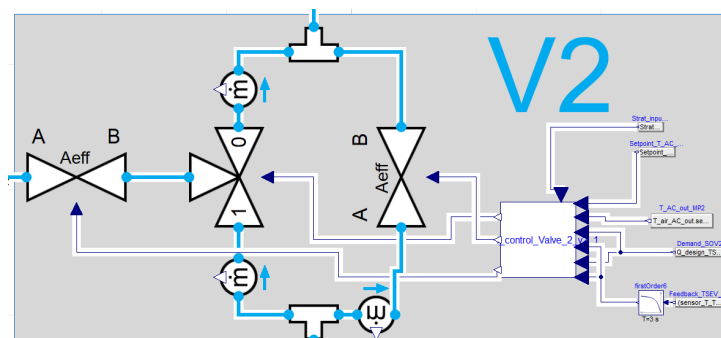
Figure 4.8: Exemplary Valve V2 as an example of an Actively Controlled Valve

The valve control block accommodates two PI controllers that control the TWV and SOV. The FSOV is, in case it is required to be active, regulated to act contrary to the SOV using the same PI controller as the SOV, but with inverse behaviour. The following Table 4.1 presents the different valve codes and their meaning.

Table 4.1: Valve codes with their corresponding valve position.

Valve codes	Three way valve	Bypass SOV	SOV before TWV (FSOV)
100	0	0	1
101	0	1	1
102	1	0	1
103	1	1	1
104	0	1	0
105	1R	0	1
106	1R	1R	1
107	1R	1	1R

R: Regulating; **SOV:** Shut off Valve
TWV: Three Way Valve

4.5.2 Pump Control

The main pump is controlled by either a PI controller in the case of controlling the supply air temperature or the mass flow is calculated based on the design TSEV capacity.

In the case of charging, the heat pump should run at the design TSEV capacity and therefore the mass flow of the main pump is adapted to match the maximum system capacity, based on the following Eq. 4.20.

$$\dot{m}_{w,MP} = \frac{\dot{Q}_{max.sys.cap.}}{c_{p,w} \cdot \Delta T_{TSEV}} \tag{4.20}$$

If the cold storage tanks reach a $SOC_{CST} > 0.99$, the charging cycle stops and the mass flow of the main pump becomes $\dot{m}_{w,MP} = 0 \, \text{kg s}^{-1}$.

In case the TSEV is in operation and the tanks are discharging, the flow through the main pump is only actively controlled if the main pump is responsible for controlling the air supply temperature. Otherwise is the flow set to the maximum pump speed, to enable the highest rate possible of cold storage discharge and TSEV operation. Both pumps (main and ice tank pump) are, in case they are actively controlled by their PI controller, controlling the temperature of the air leaving the AHU.

5 Preliminary System Results and System Optimization

The following chapter presents results from initial simulations of the ice tank model and entire system. Therefore, chapter 5.1 investigates the influence of the cross sectional area coverage of the ice tank by the CO_2 tubes onto the charging time of the ice tank. Based on the results from chapter 5.1 and further input parameters, an initial simulation of the entire system is carried out, which provides insights into the system characteristics in chapter 5.2. Based on the gained preliminary results are required system improvements presented, which are carried out in chapter 5.3 - 5.4.

5.1 Ice Tank Testing - Influence of Covered Cross Sectional Area by Tubes

The performance of the ice tank is influenced by its geometry design decisions and operating conditions. Since the model assumes a constant heat transfer coefficient on the water and refrigerant side, the tube dimensions influence only the heat transfer area and volumes of the sub-cells. Therefore, an investigation on the influence of the cross sectional area covered by refrigerant tubes onto the charging time is carried out. The simulation is carried out as a stand-alone investigation and is thereby de-coupled from the entire system model. The investigation requires a constant tube diameter, which is set within this work to $d_{tube} = 40\,\text{mm}$, and is oriented on tube sizes used within the NTNU/SINTEF laboratory. Table 5.1 shows the test conditions and operation parameters.

Table 5.1: Conditions for the Ice Tank Model Testing to investigate the Influence of the Cross Sectional Area Coverage by Tubes

Charging Conditions	
Inlet enthalpy CO_2	$h_{\text{CO}_2} = 170\ \text{kJ kg}^{-1}$
Inlet pressure CO_2	$p_{\text{CO}_2} = 21\ \text{bar}$
Mass flow rate CO_2	$\dot{m}_{\text{CO}_2} = 0.2\ \text{kg s}^{-1}$
Initial ice layer	$\delta_{i,init} = 0\ \text{m}$

Tank Geometry	
Volume (Width x Depth x Height)	$V = 1\,\text{m} \cdot 1\,\text{m} \cdot 1\,\text{m} = 1\ \text{m}^3$
Diameter of CO_2 tubes	$d_{tubes,\text{CO}_2} = 0.04\ \text{m}$
Number of tubes	$n_{tubes} = 160, 130, 100, 70, 30$
Initial water temperature	$T_{w,init} = 0\ ^\circ\text{C}$
Thickness tubes	$\delta_{tube} = 0.002\ \text{m}$
Number of cells	$n_{cells} = 20$

5.1.1 Results of Cross Sectional Area Coverage of the Ice Tank

Based on the parameters presented in Table 5.1, the influence of the cross sectional area coverage by changing the number of tubes is evaluated. Figure 5.1 shows the charging time to reach a state of charge of $SOC_{IT} > 0.99$ over the percentage of ice tank cross sectional area coverage by the refrigerant tubes. As Figure 5.1 shows, the charging time decreases with increasing cross sectional area coverage by tubes. The lowest simulated charging time of $t_{charge} = 2.95\,\text{h}$ was achieved at a covered area of $20.11\,\%$, and the highest simulated charging time of $t_{charge} = 44.34\,\text{h}$ occurred for a covered area of $3.77\,\%$.
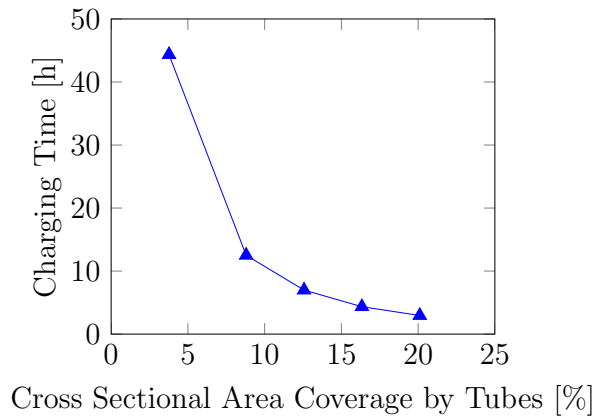
Figure 5.1: Cross Sectional Area Coverage by Tubes against the Ice Tank Charging Time

5.1.2 Discussion on Cross Sectional Area Coverage of the Ice Tank

The presented result in Figure 5.1 in Chapter 5.1.1 presents an inverse curve of the charging time against the cross sectional area coverage by the tubes. Figure 5.1 leads to the conclusion that the cross sectional covered area by the tubes should be larger than $10\,\%$, as the decrease in charging time is rather drastically for cross sectional area coverages lower than $10\,\%$. For higher cross sectional area coverages by the refrigerant tubes, the decrease in charging time is limited, and therefore, it is questionable whether a higher cross sectional area coverages by the refrigerant tubes is beneficial. Since a higher cross sectional area coverage by the refrigerant tubes leads to a higher number of tubes (for a constant tube diameter d_{tube}), the thermal energy storage capacity is decreased, since the space for the ice formation decreases. Furthermore, the refrigerant flow per tube decreases in a practical application with a higher number of tubes. Hence, the Reynolds number decreases, which would consequentially decrease the heat transfer coefficient. This effect is not considered within the model, as the heat transfer coefficient is set to be constant on the water and refrigerant side and independent of the flow regime. Hence, the benefits of a higher number of tubes needs to be treated carefully and it requires the implementation of a heat transfer correlation of evaporating CO_2 for vertical tubes for further investigations.

Besides the effect on the heat transfer coefficient, the material and production costs increase with an increased number of tubes.

For further simulations, the cross sectional area coverage is set to be within $12-13\%$ and the number of tubes is adapted accordingly to the cross sectional area of the ice tank.

5.2 Initial Simulation

It is required prior to the simulation of the entire system (hydronic system and CO_2 heat pump system) to set system parameters, setpoints and sizes to the individual components. Therefore, the following chapter 5.2.1 presents the parameters, setpoints and component sizes of the individual components. The presentation of the parameters in chapter 5.2.1 follows the presentation of the gained results (chapter 5.2.2) with a subsequent discussion (chapter 5.2.3).

5.2.1 Design Parameters

The following section presents the design parameters for the initial simulation. It should be noted that these parameters are exemplary to gain insights into the system behaviour and performance. The exemplary AC load, which is posed onto the system is shown in Figure 5.2. The maximum occurring load is $\dot{Q}_{AC,load,max} = 60.1\,\text{kW}$.
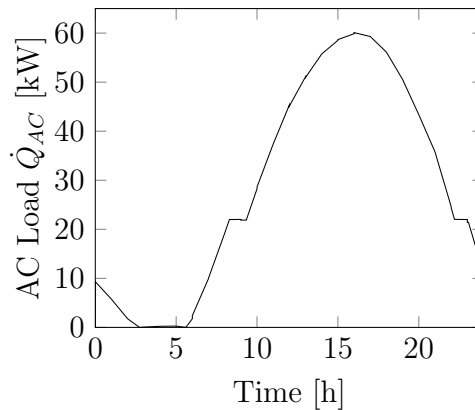
Figure 5.2: Exemplary Air Conditioning Load posed onto the Control Volume

5.2.1.1 Cold Water Storage Tanks:

Inner Tank Volume: For initial simulations, the inner cold water storage tank volume is set to $V_{tank} = 2.5\,\text{m}^3$ for both cold water storage tanks.

Diameter and height of tank: The diameter of the cold water storage tanks is set to $d_{CST} = 1\,\text{m}$ which is based on manufacturers informations for DHW storage tank sizes of $V = 1000\,\text{L}$ (Danfoss ThermoClean®004X1623[32]).

Inlet & Exit Port Location: The inlet and exit ports are located at the top and bottom of the tank, such that no dead volume is created above or below the inlets.

Initial Temperature: The initial temperature of the tanks is set to $T_{CST,init} = 15\,°C$.

5.2.1.2 Heat Pump:

Design TSEV Load $\dot{Q}_{TSEV,design}$: Based on the simulational and experimental work by Bengsch[29], the design TSEV load is set to $\dot{Q}_{TSEV,design} = 20\,kW$.

5.2.1.3 Ice Tank

Length, width, height of tank: For the initial simulation, an ice tank size of $W_{tank} \cdot D_{tank} \cdot H_{tank} = 2.5\,m \cdot 2.5\,m \cdot 1\,m$ is chosen.

Number of Tubes $n_{tubes,IT}$: Based on the results from Figure 5.1 and the following discussion in chapter 5.1, the tube number should be chosen such that the cross sectional area coverage is higher than 12 % for an efficient charging time. That corresponds with a tube diameter of $d_{tube,IT} = 0.04$ m to approx. 100 tubes per square meter. Based on the cross sectional area, the tube number results in $n_{tubes,IT} = 625$.

Outside Tube Diameter d_{tube,CO_2}: The outside tube diameter is chosen to be $d_{tube,IT} = 40mm$, as presented in chapter 5.1.

Initial Ice Coverage $\delta_{i,init}$: The initial ice thickness is set to $\delta_{i,init} = 0\,m$.

α_{CO2}: As the CO_2 evaporates within the tubes of the ice tank, its thermophysical properties are changing and thereby the heat transfer characteristics as well. However, the simplified ice tank model considers only a constant heat transfer coefficient, both on the refrigerant as well as the secondary fluid side. Hence, an approximated value is chosen to represent the possible operating conditions. Pamitran et al.[33] investigated experimentally the heat transfer coefficient of CO_2 in circular, horizontal tubes. For CO_2 , the measured heat transfer coefficient lied between approx. $\alpha_{CO2} = 7 - 12\,kW\,m^{-2}\,K^{-1}$ [33]. Based on these results, a heat transfer coefficient on the refrigerant side is assumed to be constant at $\alpha_{CO2} = 8000\,W\,m^{-2}\,K^{-1}$.

α_{water}: On the water side, the heat transfer coefficient will depend on the state of charge, as the ice layer influences the flow cross sectional area. Hence, depending on the state of charge, mass flow and geometry, the heat transfer coefficient varies. As there is no experimental data available, an estimate of α_{water} is taken based on Incropera et al.[28] to be $\alpha_{water} = 500\,W\,m^{-2}\,K^{-1}$.

Water Flow direction The water is assumed to always enter the ice tank from the top and exit from the bottom. Within initial simulation, numerical instabilities

were observed that led to this assumption. The impact of this assumption will be discussed in detail within the discussions.

Ice Tank Refrigerant Mass Flow The allowable range of the PI controller, which controls the refrigerant mass flow is set to $\dot{m}_r = 0 - 0.4\,\text{kg}\,\text{s}^{-1}$.

5.2.1.4   Water Pumps, Fans and Air Control System:

Maximum Mass Flow Main Pump $\dot{\mathbf{m}}_{\mathbf{w,MP}}$: The mass flow of the pump is based on the maximum cooling load, and a water side temperature difference of minimum 4 K over the heat exchanger. Hence, the pump mass flow for 60.10 kW maximum heating load is

$$\dot{m}_{w,MP,max} = \frac{\dot{Q}_{max,load}}{c_{p,w} \cdot \Delta_T} = \frac{60.10\,\text{kW}}{4.180\,\text{kJ}\,\text{kg}^{-1}\,\text{K}^{-1} \cdot 4\,\text{K}} = 3.594\,\text{kg}\,\text{s}^{-1} \qquad (5.1)$$

To create a margin to the required pump speed, a maximum pump speed of $\dot{m}_{w,MP,max} = 4\,\text{kg}\,\text{s}^{-1}$ is chosen.

Maximum Mass Flow Ice Tank Pump $\dot{\mathbf{m}}_{\mathbf{w,IP}}$: The maximum mass flow of the ice tank pump (IP) is chosen to be $\dot{m}_{w,MP,max} = 3\text{kg}\,\text{s}^{-1}$ based on the same assumptions as the maximum mass flow of the main pump, but as the ice tank pump usually does not cover solely the cooling demand, but in combination with the main pump, a lower maximum mass flow is regarded as acceptable. The maximum ice tank mass flow may be subject to later changes, depending on the gained results.

Maximum and Standby Fan Speed: The maximum fan speed is designed such that it can pump sufficient air flow for 90% of the highest cooling load. 90 % is chosen, since it is assumed that effects like building thermal mass and air volume inertia do not require the fan to cover the entire maximum cooling load at once.

Hence, Equation 5.2 calculates the maximum air flow based on an energy balance on the air flow.

$$\dot{V}_{air} = \frac{\dot{Q}_{max,load} \cdot 0.9}{c_{p,air} \cdot \rho_{air} \cdot \Delta T} \qquad (5.2)$$

The highest peak heating demand occurs based on the demand profile of Figure 5.2 with 60.1 kW. The design temperature difference is assumed to be the difference between the highest indoor temperature (25 °C) and the supply air setpoint temperature (9 °C), resulting in a temperature difference of $\Delta T = 18\,\text{K}$.

With thermophysical property values of air based on the EES software at $T = 15\,°\text{C}$

and $p = 1.013\,\text{bar}$, the volume flow calculates to

$$\dot{V}_{air} = \frac{60.1\,\text{kW} \cdot 0.9}{1.006\,\text{kJ kg}^{-1}\,\text{K}^{-1} \cdot 1.204\,\text{kg m}^{-3} \cdot 16\,\text{K}} = 2.79\,\text{m}^3\,\text{s}^{-1} \tag{5.3}$$

Hence, a maximum volume flow of $\dot{V}_{air,max} = 3\text{m}^3\,\text{s}^{-1}$ is set as the upper limit and $\dot{V}_{air,max} = 0.5\text{m}^3\,\text{s}^{-1}$ is set as the lower limit.

Indoor Setpoint Temperatures: Reference values for acceptable indoor conditions are based on NS EN ISO 7730[34], which gives an indoor temperature during summer of $T_{indoor} = 24.5 \pm 1.5\,°\text{C}$ as reference values, for category type B of indoor comfort. To limit the magnitude of temperature fluctuations within the system is the upper temperature setpoint reduced to $T_{room,SP,upper} = 25\,°\text{C}$.

Air Volume Size: The air volume size is set to $V_{air} = 7000\,\text{m}^3$.

AHU Sizing: The sizing of the air handling unit is oriented on air handling units located within the laboratory. The following AHU dimensions are implemented:

- Finned Tube Length: 3 m

- Number of serial and parallel tubes: 20 and 12, respectively

- Number of serial and parallel tubes distance: 0.022 m and 0.025 m, respectively

- Fin Thickness: 0.2e-3 m

- Fin Pitch: 0.004 m

- Inner Tube Diameter: 0.017 m

- Tube Wall Thickness: 1.5e-3 m

- Number of Tube side Parallel Hydraulic Flows: 10

AHU Heat Transfer Coefficients: Based on Incropera et al.[28], the heat transfer coefficient is assumed to be $\alpha_{water,AHU} = 1000$ W m^{-2} K^{-1}. On the air side, the heat transfer is estimated to be $\alpha_{air,AHU} = 65$ W m^{-2} K^{-1}. This estimate is based on the publication by Sun et al.[35].

5.2.1.5 System Strategy Control:

The following parameters are input values for the implemented control strategy.

Minimum Chiller Load: The minimum chiller load is assumed to be 10 % of the maximum system capacity of the heat pump. Hence, for a system capacity of $\dot{Q}_{0,HP,max} = 20\,\text{kW}$, the minimum allowable chiller load is $\dot{Q}_{HP,min} = 2\,\text{kW}$.

Downshift Threshold Value: As mentioned in chapter 3.3, a feedback control is built that determines whether the current operation strategy is sufficient or a strategy with a higher or lower cooling capacity is required. For a downshift in system capacity, a threshold value of 0.3 is taken. That implies that in case the feedback for the downshift is below 0.3, the operation strategy will be changed to a operation strategy with a lower cooling capacity.

Minimum State of Charge X_{min}**:** The minimum state of charge of the TES, meaning the cold water tanks and the ice tank combined is set to $X_{min} = 0$.

Times of On-Peak and Off-Peak Period: The off-peak period, which triggers the charging of the TES system, is set to be from 11pm until 8am and the on-peak period vice-versa.

Setpoint Supply Air Temperature The setpoint temperature of the supply air temperature that leaves the AHU is initially set to 9 °C.

5.2.2 Preliminary Results of the Initial Simulation

The following results are based on the design parameters presented in the previous chapter 5.2.1 and the operation and control strategy from chapter 3.3. Figure 5.3 presents a general system overview, Figure 5.4 component and compressor loads and Figure 5.5 details on the air handling unit. Within all Figures, the on-peak period is marked in grey (light and dark grey). The period of the load limiting operation strategy is marked in light grey and the maximum use of storage in dark grey.

The first subplot of Figure 5.3 shows the (AC) load on the control volume over a 24 h period. It ranges between 0 - 60.1 kW. During the on-peak period, the maximum load of $\dot{Q}_{load} = 60.1\,\text{kW}$ at $t = 16\,\text{h}$ occurs. The load profile shows generally higher loads during the on-peak period. The second subplot in Figure 5.3 shows the operation modes over the 24 h time span. During the off-peak period (white background), the operation mode varies between 1 and 4, which corresponds to CST charging with the TSEV and CST charging with the TSEV + AHU operation. A change in operation strategy from TES charging to TES discharging with min. use of storage occurs at $t = 8.25\,\text{h}$. Within the TES Discharge - Min. Use of Storage period, the operation mode varies between the different possible operation modes 10, 15, 13. At $t = 12.25\,\text{h}$, the operation mode stays at operation mode $OM = 13$, the highest system capacity operation mode.

The third subplot in Figure 5.3 shows the SOC of the entire TES system X, the state of charge of the ice tank SOC_{IT} and the state of charge of the cold storage tank SOC_{CST}
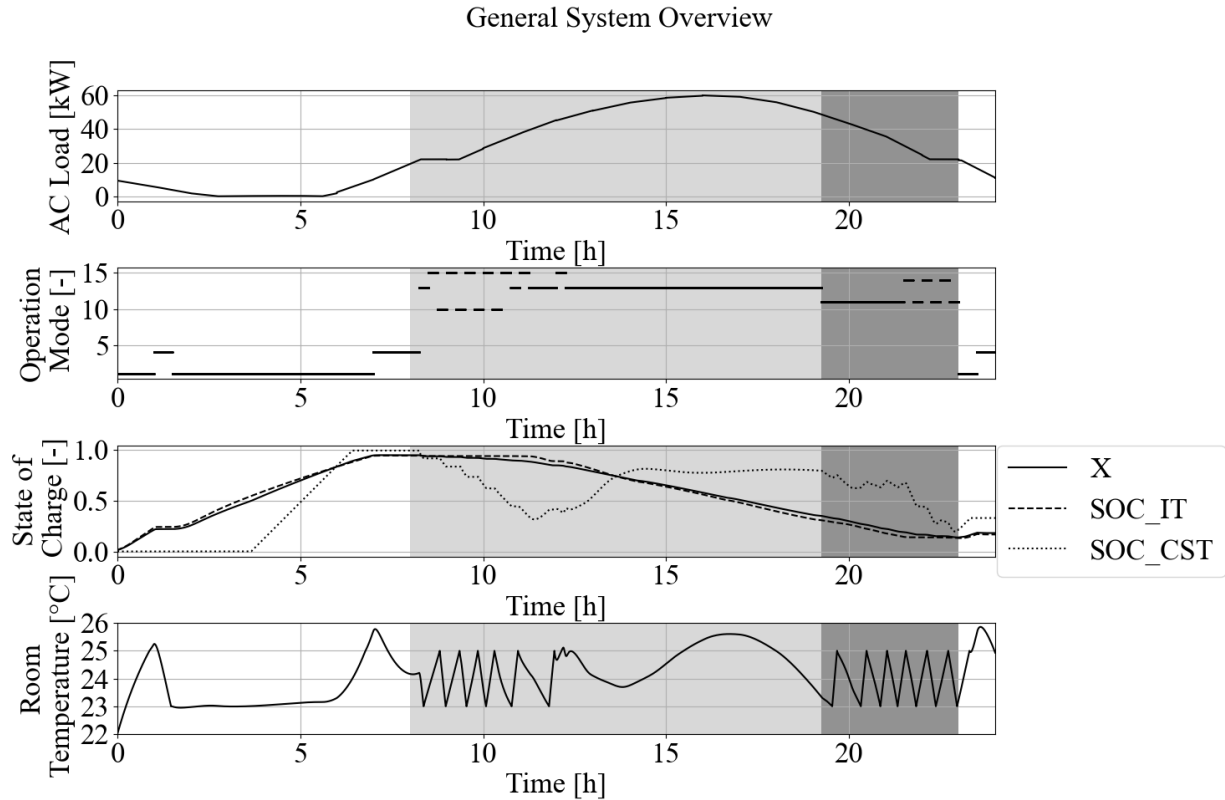
Figure 5.3: Results from the Initial Simulation 1/3. On-peak Period is marked in grey, Minimal Use of TES in light grey and Maximal Use of TES in dark grey

over the 24 h time span. One obtains that the SOC_{IT} increases whenever the operation mode is $OM = 1$, corresponding to CST charging. At times during the off-peak period, where the operation mode is $OM = 4$, the SOC_{IT} remains constant. Furthermore, the rate of charge of the ice tank can be seen to be significantly lower than the charging of the cold water storage tanks. During the on-peak period, the SOC_{IT} shows during the operation modes $OM = 10$ and $OM = 15$ generally smaller discharge rates compared to the time when the system operates at the highest capacity operation mode $OM = 13$. The SOC_{CST} increases during the Peak Load Limiting Strategy between $t = 11.45\,\text{h} - 14.44\,\text{h}$ and remains approximately constant until the change in operation strategy to TES Discharge - maximum use of storage. At the end of the on-peak period, the remaining SOC is at $X = 0.14$.

The measured room temperature T_{room} of the control volume is shown in the fourth subplot of Figure 5.3. During the off-peak period increases the room temperature depending on the induced load, until the operation mode changes from $OM = 1$ to $OM = 4$, which decreases the room temperature. During the on-peak period fluctuates the room temperature T_{room} between the boundaries of $T_{room} = 23 - 25\,°\text{C}$, unless the load on the control volume is near its peak. The same fluctuation is observed during the operation strategy "TES

Discharge - Maximum Use of Storage" between $T_{room} = 23 - 25\,°\text{C}$.

Figure 5.4 shows the compressor and component loads over a 24-h time span. The compressor work of the LT compressor is shown in the first subplot. The LT compressor operates during the off-peak period whenever the operation mode is $OM = 1$.

Once the SOC_{IT} exceeds $SOC_{IT} = 0.95$, the LT compressor stops. The maximum LT compressor work is observed at $t = 0.34$h with $\dot{W}_{LT,comp} = 18.01\,\text{kW}$. In the second subplot of Figure 5.4 is the work of the MT compressor shown over the 24 h time span. The MT compressor work peaks at $\dot{W}_{MT,comp} = 28.2\,\text{kW}$ at $t = 3.24$h. During the on-peak period at times where the operation mode remains constant at $OM = 13$ remains the MT compressor work constant as well at $\dot{W}_{MT,comp} \approx 5.44\,\text{kW}$.

The third subplot of Figure 5.4 presents the load on the TES on the water side. Within the off peak period, the load on the CST is negative while TES charging (operation mode $OM = 1$). During the on-peak period, the load is positive, which corresponds to discharging. It furthermore shows a negative load at $t = 11.4 - 11.84$ h and $t = 12.4 - 14.22$ h, which occurs at the same time as the increase of the SOC_{CST}.

The fourth subplot of Figure 5.5 shows the load on the TSEV. In periods where the TSEV is active, the load is at $\dot{Q}_{TSEV} \approx 20$kW, which corresponds to the design evaporator load. Exceptions are seen at times of $t = 8.37 - 12.32$ h, with fluctuating TSEV loads between $\dot{Q}_{TSEV} \approx 10.2 - 28\,\text{kW}$.

Figure 5.5 shows details of the air handling unit. The first subplot of Figure 5.5 shows the volume flow of air over the 24-h period. The volume flow switches between $\dot{V}_{air,AHU} = 0.5\,\text{m}^3\,\text{s}^{-1}$ and $\dot{V}_{air,AHU} = 3\,\text{m}^3\,\text{s}^{-1}$. The second subplot shows the room temperature T_{room}, which was already presented in Figure 5.3, but is included for better understanding of the system. The third subplot of Figure 5.5 shows the logarithmic mean temperature difference (LMTD) of the air handling unit AHU. During the time near the highest load on the control volume, which corresponds to the highest room temperature T_{room}, the LMTD is at $LMTD = \approx 8.7\,\text{K}$. Towards the beginning and end of the on-peak period varies the LMTD between $LMTD = \approx 1.5 - 7.3\,\text{K}$, with the shape corresponding to the volume flow of air. During the off-peak period in $OM = 4$, the $LMTD$ is observed to approach $LMTD \approx 2.83\,\text{K}$.

The fourth subplot shows the inlet (supply) temperature of water and the exiting (supply) temperature of air of the AHU. During the off-peak period, the supply air temperature $T_{s,air}$ during times where the AHU is active (OM = 4), is $T_{s,air} \approx 18 - 25\,°\text{C}$. The corresponding water temperature is $T_{s,w} \approx 4\,°\text{C}$. During the on-peak period, the temperatures vary with water temperatures between $T_{s,w} \approx 3.1 - 9.53\,°\text{C}$. The corresponding air temperatures are between $T_{s,air} \approx 4 - 14\,°\text{C}$.
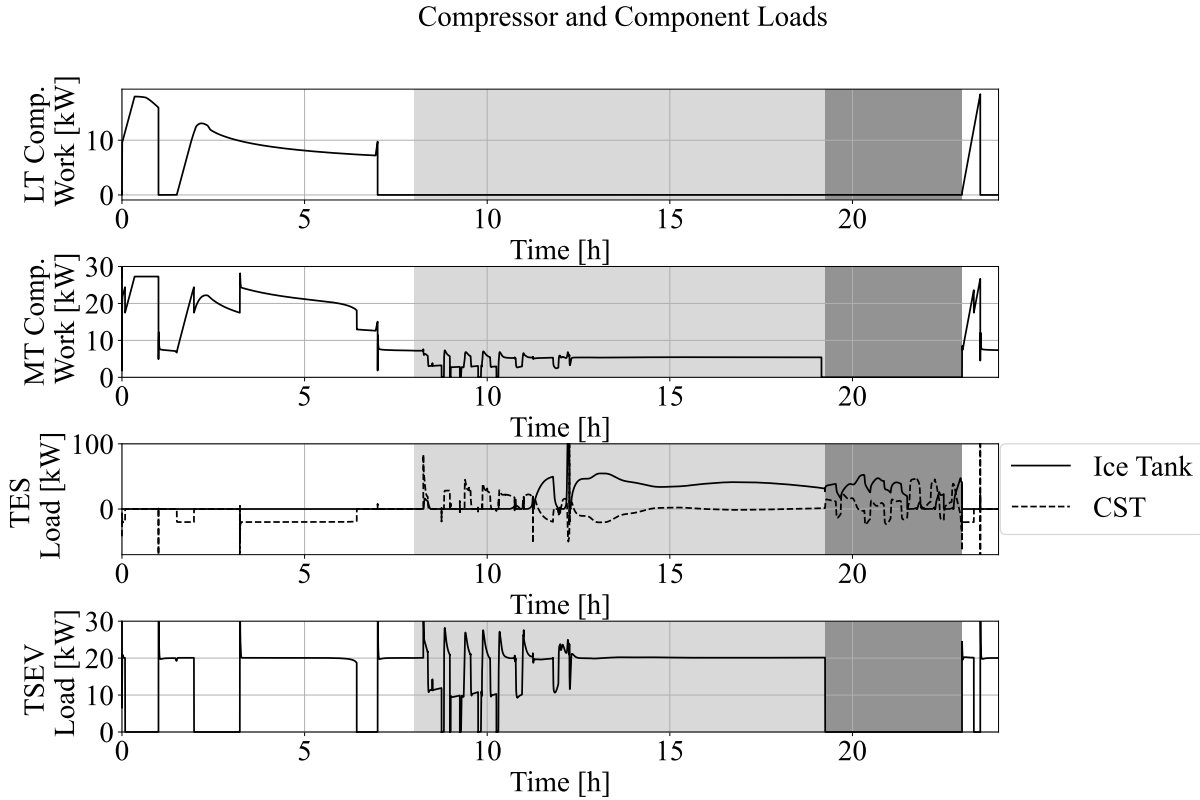
Figure 5.4: Results from the Initial Simulation 2/3. On-peak Period is marked in grey, Minimal Use of TES in light grey and Maximal Use of TES in dark grey

5.2.3 Discussion of the Preliminary Results of the Initial Simulation

The discussion of the results is divided into the TES charging period, the TES discharge - Min. use of storage + peak load limiting period and the TES discharge - maximal use of storage period. Beforehand are general results and observations discussed.

Generally, the room temperature is maintained with small exceptions (Figure 5.3 subplot four) in the desired temperature range of $T_{SP,room} = 23 - 25\,°C$. Furthermore, the change in operation modes and the increase in system capacity due to the change in operation modes works as expected, within certain limitations, which will be discussed during the later discussion. Based on the presented result from Figure 5.4 in the first and second subplot, one obtains that the major operating time under full capacity of the compressors is shifted to off-peak periods, by the usage of the TES system. Only the MT compressor is required to run at a reduced load of $\dot{W}_{MT,comp} = 5.44\,kW$ during the on-peak - min. use of storage period, to operate the TSEV at an evaporator load of $\dot{Q}_{TSEV} = 20\,kW$.

Charging period:
At the end of the charging period, the TES be should fully charged to $SOC_{IT} = 0.95$. However, the SOC_{IT} does not reach an entirely charged state at the end of the off-peak

Air Handling Unit
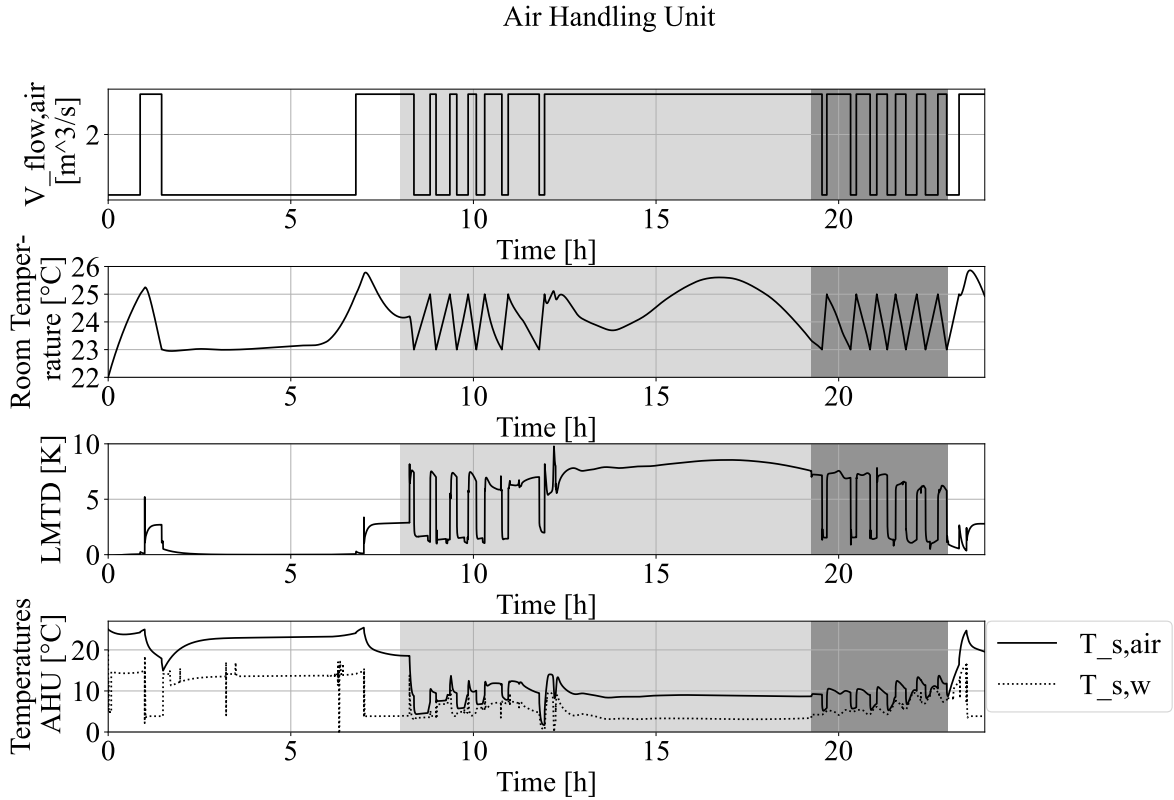
Figure 5.5: Results from the Initial Simulation 3/3. On-peak Period is marked in grey, Minimal Use of TES in light grey and Maximal Use of TES in dark grey

period $SOC_{IT} = 0.94$ (cmp. Figure 5.3), but in multi-day operations is the off-peak period extended by one hour, since the off-peak period is starting from 11pm the day before. Hence, the remaining $\Delta SOC_{IT} = 0.01$ would be charged within the additional hour.

As presented in Figure 5.3 the room temperature T_{room} overshoots the upper setpoint of $T_{SP,room,high} = 25\,°\mathrm{C}$ during operation in the off-peak period. From the presented results in Figure 5.3, one obtains that the OM is changed with a delay, even though the room temperature T_{room} exceeded $T_{SP,room,high} = 25\,°\mathrm{C}$. The delay can occur, since the operation mode and operation strategy is determined every 15 min. Hence, if the overshoot of the room temperature happens just after the operation mode has been reviewed, it takes another 15 min until the operation mode is changed accordingly. Additionally, system inertia due to the liquid mass within the pipe imposes further delays in the reaction time on the AHU.

Within the charging process of the CTES, the compressor work reaches a maxima, as shown in Figure 5.4, at rather high maximum compressor loads. The reason for that can be found in the control of the ice tank charging. As the current PI controller, that represents the LT stage of the heat pump system, regulates the mass flow of CO_2 at $p_{CO_2} = 20\,\mathrm{bar}$ between $\dot{m}_{CO_2} = 0 - 4\,\mathrm{kg\,s^{-1}}$, the corresponding LT and consequentially

the MT compressor work are highly dependent on the mass flow of CO_2. Thereby, maximum compressor loads of $\dot{W}_{LT,comp,max} = 18.1\,\text{kW}$ and $\dot{W}_{LT,comp,max} = 28.2\,\text{kW}$ occur, as the PI controller of the ice tank tries to reach the target enthalpy corresponding to $x = 1$ at $p_{CO_2} = 20\,\text{bar}$. The high peak load followed by part-load operation during TES charging, decreases the compressor efficiency as the part load operation deviates from the design point of the compressor. Hence, it would be ideal, if the LT compressor could operate at full capacity the entire charging period. Therefore, a capacity regulation system should be implemented as one of the next steps with an adaptable CO_2 evaporation pressure.

Furthermore, the presented results from Figure 5.4 show that the condition "Only charge CST when LT compressor load smaller than 10 kW" reduces the maximum MT compressor work, as the charging of the CST tank consequentially starts when the LT compressor work $\dot{W}_{LT,comp} < 10\,\text{kW}$. The charging of the CST can be seen in the third subplot of Figure 5.4 at periods where the TES load of the CST is negative, which means charging. The TSEV load is, during the charging period whenever in operation, at approximately the design setpoint of $\dot{Q}_{TSEV} \approx 20\,\text{kW}$ (Figure 5.4). Hence, one can conclude that during the charging period operates the TSEV as intended at the design capacity, and if not for the charging of the ice tank would the MT compressor operate at an approximately constant load. Furthermore, the LMTD of the AHU $LMTD_{AHU}$ is at an acceptable value of $LMTD_{AHU} = 2.83\,\text{K}$ at times of $OM = 4$, which is in this case the consequence of the air supply temperature $T_{s,air}$ not reaching the setpoint of $T_{s,air,SP} = 9\,°\text{C}$. Comparing the $LMTD_{AHU}$ to the later period when the operation mode is $OM = 13$ between $t \approx 13-18\,\text{h}$, the $LMTD_{AHU}$ is significantly higher (up to $LMTD_{AHU} = 7.2\,\text{K}$). This could possibly be improved by changing the geometry of the heat exchanger and thereby influencing the heat transfer coefficient. However, as the heat transfer coefficient is assumed to be constant, hence independent on the flow characteristics, the $LMTD_{AHU}$ is connected with a certain uncertainty, as the water side heat transfer coefficient would change depending on the mass flow, as the mass flow of water can vary between $\dot{m}_w = 0-7\,\text{kg}\,\text{s}^{-1}$. Therefore, heat transfer correlations should be implemented, to improve the uncertainties related to the air handling unit.

On-peak Period - Min. use of Storage and Peak Load Limiting (Block 3):
The on-peak period, where Block 3 is active, which refers to peak load limiting and min. use of storage, is marked in light grey in the Figures 5.3 - 5.5. The SOC_{IT} and SOC_{CST} decrease during $t = 8.25 - 11.45\,\text{h}$, since the AC load onto the control volume rises above the design TSEV capacity of $\dot{Q}_{TSEV,design}$. However, within this time period, one observes that the SOC_{CST} remains constant during certain times (e.g. $t = 9-9.3\,\text{h}$), even

though the operation mode is $OM = 10$ or $OM = 15$ (Both $OM = 10$ or $OM = 15$ are designed to discharge the CST). This is caused by the lower volume flow of air setpoint $\dot{V}_{fan,air,lowersetpoint} = 0.5\,\mathrm{m^3\,s^{-1}}$. The low volume flow of air results in lower hydronic system loads and therefore reduces the load onto the TSEV and TES. Hence, as the valve V2 is controlling for $OM = 10$ and $OM = 15$ the distribution of flow between the TSEV and CST, and tries to always maintain the design TSEV load of $\dot{Q}_{TSEV,design} = 20\,\mathrm{kW}$, it directs the entire flow of the main pump through the TSEV, leading to no CST discharge.

Whenever the switch to a high volume flow of air occurs in the AHU, the load on the TSEV overshoots the design capacity, as V2 does not react fast enough to predict and limit the TSEV design capacity overshoot. This TSEV capacity overshoot is an appearance that occurs within the model due to the implementation of the TSEV, since the PI controller regulates based on temperature and is not limited to a maximum of $\dot{Q}_{TSEV,design} = 20\,\mathrm{kW}$ while regulating. Within a real system, an overshoot may occur for short periods of time, but is self-regulating due to the evaporation pressure and temperature increase, leading to lower transferred heat and thus higher water exit temperatures. Additionally, the current TSEV implementation does not accurately represent the system inertia, which would affect dynamic changes of the system.

The control of the volume air flow rate $\dot{V}_{air,AHU}$ creates, as presented in Figure 5.3 in the fourth subplot, an oscillation of the indoor temperature with up to $\Delta T_{room} = 2\,\mathrm{K}$ in the time span of $\Delta t \approx 0.3\,\mathrm{h}$. This could possibly cause discomfort due to the rapid changes of temperature. Therefore, a stabilization of the indoor temperature should be subject of the further improvements of the system.

As already discussed on the TSEV load, where the fluctuations occur at $t = 8.25 - 11.45\,\mathrm{h}$, the MT compressor load consequentially differs as well from its value at the design evaporator load. This causes instability within the refrigeration system and requires fast and precise system controls. Furthermore, as the MT compressor load is based on the non-linear regression model from chapter 4.3.3.1, the MT compressor load response is immediate to the change of water inlet conditions of the TSEV. A real heat pump system is expected to have slower and less rapid system responses due to system inertia and heat transfer characteristics.

Between $t = 11.45 - 19.25\,\mathrm{h}$ shows the SOC_{CST} a remarkable trend. Even though the active operation mode discharges the cold storage tanks, shows the SOC_{CST} an increase in the beginning of the time period and remains constant afterwards, even though no charging of the CST is intended. Because the temperature of water leaving the AHU within this period is lower than the CST temperature and lower than the minimum

charging temperature, the cold storage tank is charged unintentionally. The temperature of water is lower due to the usage of the ice tank, since the water exiting the ice tank is at approx. $T_{w,IT} \approx 0 - 1 \,°\text{C}$, depending on the operating conditions. The recharge is highly dependent on the setpoint of the supply air temperature, and the unintentional re-charge effect would not occur at higher air supply temperature setpoints.

The LMTD is within this peak period as well rather high (up to $LMTD = 7.3 \,\text{K}$), with the supply air temperature reaching approx. its setpoint at $T_{s,air,SP,AHU} = 9 \,°\text{C}$. That indicates that the hydronic system is able to contain the imposed load on the water side, as the supply air reaches its target temperature, but the volume flow rate of air of $\dot{V}_{air,max} = 3 \,\text{m}^3 \,\text{s}^{-1}$ is not sufficient to maintain a room temperature of lower than $T_{room,max} \leq 25 \,°\text{C}$ during this period. Hence, an increase in the volume flow rate of air would be beneficial to encounter the room temperature increase. A decrease in air supply temperature $T_{s,air}$ would also reduce the room temperature, however, a reduced supply temperature would require to provide even lower water temperatures, which is limited theoretically to the freezing point of water. Furthermore, the operation of the TSEV to reach lower water temperatures does not only decrease the energy efficiency, but also has practical limitations. An operation near the freezing point of water may cause local formation of ice and thereby increase the water side pressure drop and in the worst case cause a blockage on the water side of the TSEV. Hence, the increase in volume flow rate of air is preferred over lowering the supply air temperature setpoint.

To encounter possible discomfort by the rather low supply air temperature, as it is at times leaving the AHU at $T_{s,air} \leq 10 \,°\text{C}$, the supply air should be mixed with circulating air within the control volume, to reach acceptable supply air temperatures in case living beings are within the control volume. This is not regarded further in this study, but a simple air mixing system would be required, which could be implemented by e.g. a simple fan.

On-peak period - Max. Use of Storage

During the period of Block 2 of the implemented control strategy, that takes action at $t = 19.25 - 23 \,\text{h}$, the load on the AHU is solely covered by the TES. As the AC load remains rather high, the system operates in the beginning of the period at the highest system capacity, $OM = 11$ and maintains the indoor room temperature accordingly. Within this period, the SOC_{IT} decreases due to the discharge operation. The SOC_{CST} however remains approx. constant during the first half of this time period, for the same reasons as it was the case at $OM = 13$ during the on-peak time $t = 11.45 - 19.25 \,\text{h}$, since the water temperature leaving the AHU charges unintentionally the CST. Furthermore, similar to the beginning of the on-peak period, the room temperature T_{room} oscillates

between $T_{room} = 23 - 25\,°\mathrm{C}$, which could possibly create discomfort and should therefore be changed.

At the end of the on-peak period, the state of charge of the TES system X remains at $X = 0.14$, as presented in Figure 5.3. Hence, the system control does not achieve to discharge the entire TES at the end of the on-peak period. For the ice tank, it has a greater role to entirely discharge the TES, as a remaining ice layer hinders the heat transfer between the refrigerant and the water, and thereby reduces the energy efficiency during charging. The reason for the non-entire discharge is assumed to be the combination between the unintentional recharge of the SOC_{CST}, which can't be adapted for as the remaining on-peak period cannot be prolonged, possible inaccuracies in the load prediction and an energy imbalance between the stored energy in the ice tank and energy transferred to the water, which will be presented further in chapter 7.1.

Required Actions:

Based on the presented discussion, the following steps should be taken first for further system improvement.

1. **Volume Flow Rate of Air:** To ensure that the room temperature does not increase above the upper setpoint temperature, the maximum volume flow of air should be increased from $\dot{V}_{s,air,max} = 3\,\mathrm{m^3\,s^{-1}}$ to at least $\dot{V}_{s,air,max} = 4\,\mathrm{m^3\,s^{-1}}$, and possibly even higher values in case $\dot{V}_{s,air,max} = 4\,\mathrm{m^3\,s^{-1}}$ is not sufficient.

2. **Oscillations in the Room Temperature:** A system with a corresponding controller should be implemented to reduce the fluctuations in the room temperature and maintain a more stable indoor air temperature. Thereby, possible thermal discomfort for living creatures should be avoided.

3. **Max. Compressor Load:** The LT compressor load should be limited and adapted to a rather constant LT compressor load. Ideally, the LT compressor operates during its operation at full and constant capacity. It will not be possible to operate the MT compressor at full capacity at all times, since the load during charging of the ice tank and the load during TSEV operation deviates too much. A parallel MT compressor setup reduces part-load operation to a certain extent, since one compressor can cover the TSEV load at maximum capacity and the parallel compressor could cover the additional load during charging of the ice tank.

5.3   Stability Improvement of Control Volume Air Temperature

As presented in the previous chapter 5.2.2, the room temperature oscillates between the upper and lower setpoint during the on-peak period, which could cause discomfort if the system is used e.g. within an office building. Furthermore, the initial preliminary results, presented in Figure 5.5, show that with the current maximum volume flow rate of air, the upper room setpoint temperature can not be held, as the indoor room temperature increases above the upper setpoint during peak load periods.

Hence, an active air control by means of a PI controller that regulates the volume flow rate of air is implemented and set to a maximum mass flow rate of $\dot{V}_{air,max} = 4\,\mathrm{m\,s^{-1}}$. The PI controller regulates the volume flow of air based on the temperature of air leaving the room/control volume.

Since previously the operation of the AHU was triggered by the activation of the higher setpoint of the volume flow rate of air during TES charging (see chapter 4.4), the system now needs to operate continuously the AHU, as the operation of the PI controller is permanently active. Hence, the system operates continuously in $OM = 4$. As the charging of the ice tank was previously dependent that the system operates in $OM = 1$, this condition is removed and the TES will be charged during $OM = 4$ without limitations.

In case the SOC_{CST} reaches a fully charged state before the end of the off-peak period, the operation mode changes to $OM = 12$ (AC by CST discharge) and the ice tank continuous to charge. $OM = 12$ is active as long as the SOC_{CST} is $SOC_{CST} \geq 0.8$ and at $SOC_{CST} < 0.8$, $OM = 4$ is re-activated.

Based on the changes in volume air flow rate $\dot{V}_{air,max}$ and its control, the following results are obtained.

5.3.1   Results from the Stability Improvement of Control Volume Air Temperature

Figure 5.6 shows the same subplot configuration as Figure 5.3. The first subplot of Figure 5.6 shows the AC load, which imposes higher loads during the on-peak period, which is marked in grey. Since the AC load remains unchanged to the previous simulation, the maximum load accours at the same time at $\dot{Q}_{load,max} = 60.1\,\mathrm{kW}$ at $t = 16\,\mathrm{h}$.

The second subplot of Figure 5.6 shows the operation mode. During the off-peak period, the operation mode is $OM = 4$ until the SOC_{CST} reaches $SOC_{CST} > 0.99$ (third subplot of Figure 5.6). As the $SOC_{CST} > 0.99$, the OM changes to $OM = 12$, which corresponds to covering the AC load by only cold water tanks discharge. During the on-peak load limiting (Block 3) period, the operation mode changes between $OM = 13, 15, 10$ at

71
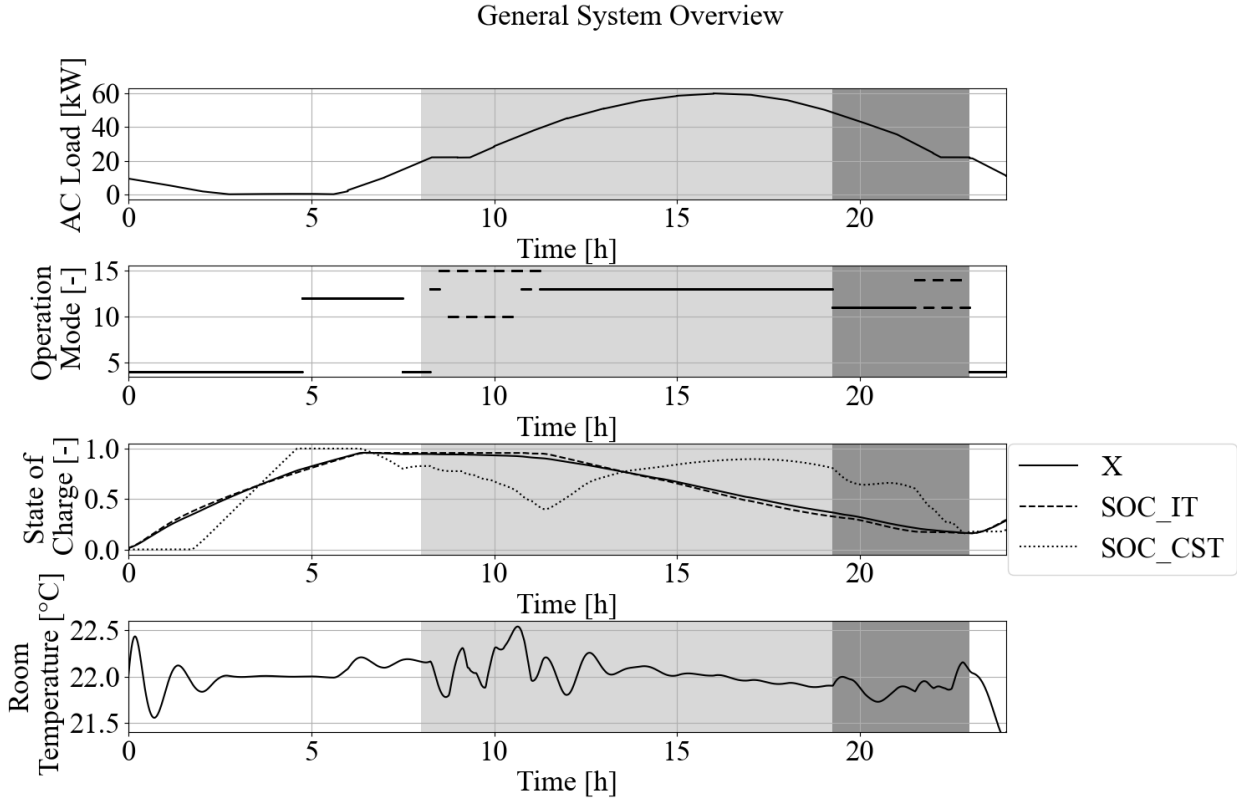
Figure 5.6: Results from the Improvement of Indoor Air Temperature Stability 1/3. On-peak Period is marked in grey, Minimal Use of TES in light grey and Maximal Use of TES in dark grey

$t = 8.25 - 11.5\,\text{h}$. At $t = 11.5 - 19.25\,\text{h}$, the operation mode remains constant at $OM = 13$. At $t = 19.25\,\text{h}$, the operation strategy changes from Min. Use of Storage/ Load limiting operation to Maximum use of storage, as the OM changes from $OM = 13$ to $OM = 11$. During the period of maximum use of storage ($t = 21.5 - 23\,\text{h}$), the operation mode OM fluctuates between $OM = 11$ and $OM = 14$.

The third subplot of Figure 5.6 shows the state of charge of the TES X, the SOC_{IT} and SOC_{CST}. The SOC_{IT} increases from $t = 0\,\text{h}$ until it reaches $SOC_{IT} > 0.95$ at $t \approx 6.31\,\text{h}$ and remains constant afterwards within the off-peak period. The SOC_{CST} increases within the off-peak period linearly between $t \approx 1.48\,\text{h} - 4.5\,\text{h}$ and remains at $SOC_{CST} = 1$ afterwards. During the on-peak period, where the min. use of storage / peak load limiting is active, the SOC_{CST}, X and SOC_{IT} decrease initially, depending on the OM. At $t = 11.64\,\text{h}$, the SOC_{CST} reaches a local minimum with $SOC_{CST} = 0.38$, with the SOC_{CST} approaching a local maximum of $SOC_{CST} = 0.89$ at $t = 17.05\,\text{h}$. During the on-peak max. use of storage period, the SOC_{CST} and SOC_{IT} decrease gradually, with the SOC_{CST} maintaining a plateau of $SOC_{CST} \approx 0.61 - 0.65$ between $t = 20 - 21.4\,\text{h}$.

The fourth subplot of Figure 5.6 shows the room temperature T_{room} over the 24 h period. The room temperature T_{room} approaches the setpoint of $T_{SP,room} = 22\,°\text{C}$ within

the off-peak period. During the on-peak period, the room temperature T_{room} fluctuates between $T_{room} = 22 \pm 0.5\,°\text{C}$, except at $t = 11.57\,\text{h}$ with $T_{room,max} = 22.53\,°\text{C}$.

Subplot 1 of Figure 5.7 shows the LT compressor work $\dot{W}_{LT,comp}$. The compressor work increases initially until it reaches $\dot{W}_{comp,LT} = 17.98\,\text{kW}$ at $t = 0.34\,\text{h}$. From the plateau it approaches $\dot{W}_{comp,LT} = 7.13\,\text{kW}$ at $t = 6.31\,\text{h}$. As the SOC_{IT} reaches the setpoint $SOC_{IT,SP} = 0.95$, the LT compressor shuts off, and remains inactive during the on-peak period. Once the end of the on-peak period is reached, the LT compressor work increases until it reaches $\dot{W}_{comp,LT} = 18.8\,\text{kW}$ at $t = 23.51\,\text{h}$.
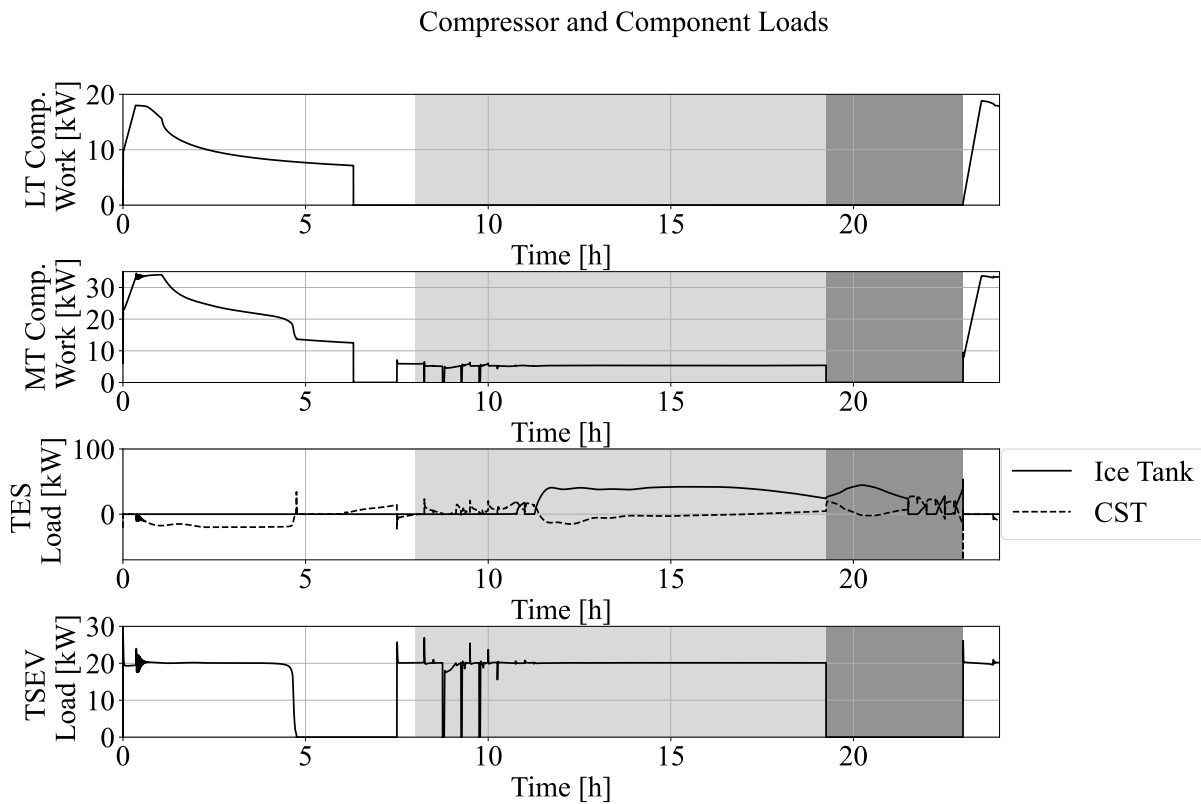
Figure 5.7: Results from the Improvement of Indoor Air Temperature Stability 2/3. On-peak Period is marked in grey, Minimal Use of TES in light grey and Maximal Use of TES in dark grey

Subplot 2 of Figure 5.7 shows the MT compressor work $\dot{W}_{MT,comp}$, which increases approximately linearly from $t = 0 - 0.34\,\text{h}$ to $\dot{W}_{MT,comp} = 33.68\,\text{kW}$. From $t = 0.34\,\text{h}$, the MT compressor work shows a slow increase up to $\dot{W}_{MT,comp} = 33.87\,\text{kW}$ $t = 1.01\,\text{h}$. The MT compressor work $\dot{W}_{MT,comp}$ decreases until the SOC_{IT} is at $SOC_{IT} > 0.95$ at $t \approx 6.31\,\text{h}$, with a sharp decrease at $t = 4.5\,\text{h}$ where $SOC_{CST} > 0.99$. During $t = 6.3 - 7.5\,\text{h}$, the MT compressor remains off, and is re-activated at $t = 7.5\,\text{h}$ and operates until the end of the min. use of storage operation strategy period during the on-peak period at $t = 19.25\,\text{h}$.

During the min. use of storage period (marked in light grey), the MT compressor load is approximately constant at $\dot{W}_{MT,comp} = 5.45\,\text{kW}$. During the maximum use of storage period within the on-peak period (marked in dark-grey), the MT compressor remains off, until the end of the on-peak period.

The water side thermal energy storage load is shown in Figure 5.7 in the third subplot. During $OM = 4$ within the off-peak period, the TES load on the CST is negative, as they are charged by the TSEV. During the off-peak period, no load on the ice tank is set. Within the on-peak period, the load on the TES fluctuates, with both the ice tank and CST being discharged until $t = 11.64\,\text{h}$, where the CST is charged during $OM = 13$. During the max. use of storage period, the load on the ice tank and CST remains positive until the end of the off-peak period.

The TSEV load is, shown in the fourth subplot of Figure 5.7, if in operation, operating at/near the setpoint of $\dot{Q}_{TSEV,SP} = 20\,\text{kW}$.

The first subplot of Figure 5.8 shows the volume flow of air $\dot{V}_{air}$. The volume flow of air $\dot{V}_{air}$ is smaller than $\dot{V}_{air} = 2\,\text{m}^3\,\text{s}^{-1}$ during the off-peak period and peaks during the on-peak period at $t = 16.29\,\text{h}$ with $\dot{V}_{air} = 3.8\,\text{m}^3\,\text{s}^{-1}$
The second subplot shows the room temperature, which was already presented in Figure 5.6, but is included in Figure 5.8 for a better overview.

The third subplot of Figure 5.8 shows the $LMTD$. The $LMTD$ is below $LMTD < 2.5\,\text{K}$ during the off-peak period and peaks with $LMTD = 8.62\,\text{K}$ at $t = 16.31\,\text{h}$ during the on-peak period.

The fourth subplot of Figure 5.8 shows the supply air temperature from the AHU and the supply water temperature to the AHU. For most periods, except times where the operation mode shows large fluctuations, the supply air temperature is near its setpoint of $T_{s,air,SP} \approx 9\,°\text{C}$. During the off-peak period is the water temperature entering the AHU at $T_{w,AHU,in} = 4\,°\text{C}$. During the on-peak period is the supply water temperature besides fluctuations within the beginning ($t = 8 - 12.8\,\text{h}$) and the end ($t = 19.25 - 23\,\text{h}$) lower than $T_{w,AHU,in} = 4\,°\text{C}$ with a minimum supply temperature of $T_{w,AHU,in} = 2.45\,°\text{C}$ at $t = 16.68\,\text{h}$.

Air Handling Unit
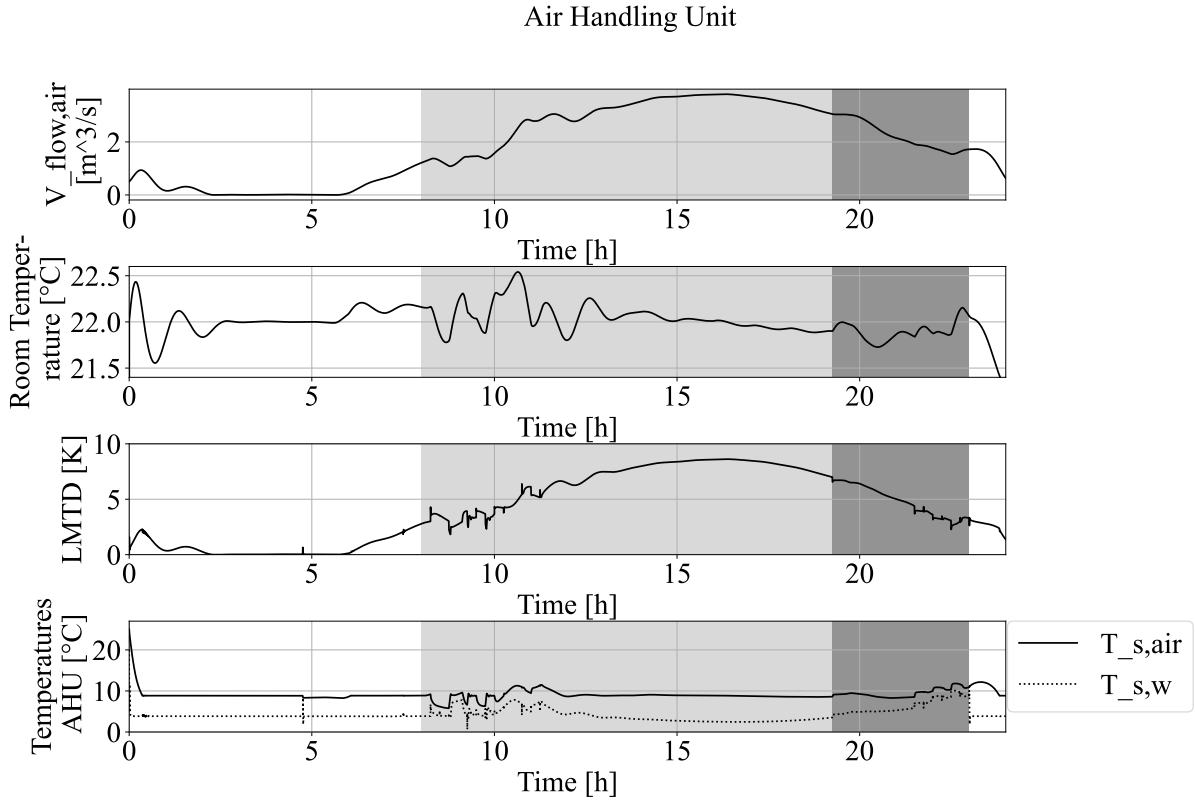
Figure 5.8: Results from the Improvement of Indoor Air Temperature Stability 3/3. On-peak Period is marked in grey, Minimal Use of TES in light grey and Maximal Use of TES in dark grey

5.3.2 Discussion of the Stability Improvement of Control Volume Air Temperature

As described in chapter 3.3, the volume flow of air through the AHU is now controlled by a PI-controller to meet the setpoint indoor temperature, with the changes implied during the charging phase.

TES Charging Phase:

Within the charging phase ($t = 0 - 8\,\text{h}$), the charging process starts immediately of the ice tank, as well as the CST. Due to the initial temperature of the CST of $T_{CST,init} = 14.85\,°\text{C}$, the SOC_{CST} shows a delayed response to the charging process, since the initial temperature is above the maximum temperature set for operation of $T_{CST,init} = 12\,°\text{C}$. Once the SOC_{CST} reached the setpoint while charging, the TSEV would only cover the AC load, which is within this period at low - very low demands (compare subplot 1 of Figure 5.6). Hence, the operation of the heat pump is not energy efficient, as the heat pump would operate outside its design point. Therefore, as described previously, the OM is changed to CST discharge, which covers the AHU load during these periods. The set limit to switch

back to $OM = 4$ of $SOC_{CST} < 0.8$, results in not entirely charged water tanks at the beginning of the on-peak period. However, since the capacity of the ice tank outweighs the capacity by the CST is a not entirely charged CST acceptable at the beginning of the on-peak period.

Since no load-limiting component is implemented into the system, the system charges the ice tank with rather large capacities, without the adaption of the evaporation pressure. Hence, large mass flow rates of CO_2 within the ice tank lead to large LT and consequentially MT compressor loads. Therefore, as mentioned in the previous chapter, a compressor capacity limit should be set, that reduces the peak power demands of the compressors, especially since the TES is fully charged well before the off-peak period ends. Therefore, charging the TES at lower capacity rates would be interesting to investigate further.

The room temperature T_{room} of the control volume stays during the off-peak period within $\pm 0.5\,\text{K}$ of the setpoint temperature (subplot four of Figure 5.6) to a satisfactory level. Furthermore, as presented in Figure 5.8 in the fourth subplot, the supply air temperature $T_{s,air}$ meets the setpoint of $T_{s,air,SP} = 9\,^{\circ}\text{C}$ for a major share of the 8 h off-peak period.

On-Peak Period - Min. Use of Storage:

As within the previous, initial simulation, the OM changes in the beginning of the on-peak period between $OM = 10, 15, 13$, depending on the required capacity. Due to the interaction between the change of OMs, the changing volume flow rate of air $\dot{V}_{air}$ and the changing load on the control volume, the indoor temperature fluctuates and breaches once the upper setpoint temperature condition. Since no further adaption was done to counteract the unintentional recharging of the CST during the on-peak min. use of storage period, the SOC_{CST} shows similarly an increase during $OM = 13$. Once the OM remains constant during the min. use of storage period, the room temperature T_{room} approaches the setpoint room temperature as desired. One could discuss on the speed of the adaption, but since the changes in temperature within the control volume are rather small, and therefore the speed of approaching the set point temperature is seen to be sufficient.

Since the RS FlipFlop block was removed by the PI controller to regulate the volume flow of air through the AHU, the load onto the TSEV is more continuous compared to the initial simulation, as the fourth subplot of Figure 5.7 shows. Small fluctuations can be seen once the operation mode is changed, but as discussed previously, system inertia of an actual heat pump system would show slower system responses, and thereby, less

fluctuations. Due to the steady TSEV operation, the MT compressor load in the second subplot of Figure 5.7 is more stable compared to the initial simulation. This improves the CO_2 heat pump system operation. The LMTD showed a slight decrease compared to the initial simulation from $LMTD = 8.7\,\mathrm{K}$ to $LMTD = 8.6\,\mathrm{K}$, which is related to the lower indoor air temperature compared to the initial simulation.

On-Peak Period - Max. Use of Storage:

Since only the room temperature control was changed within the simulation, the period of the on-peak period - Max. use of storage period remains similar, since the total AC load is unchanged. The max. use of storage period shows similarly the trend that the SOC of the CSTs increases or remains constant during parts of the first half of the max. use of storage period due to the previously discussed reasons.

Within the max. use of storage period, the TES achieves to maintain the control volume air temperature within $\pm 0.5\,\mathrm{K}$ of the setpoint temperature (subplot four of Figure 5.6).

5.4   LT Compressor Model

As presented in the results of the previous simulations (Figure 5.4 and 5.7), the LT and MT compressor work show high peak loads during the charging period. Furthermore, the evaporation pressure of the CO_2 charging the ice tank is not adapted to the SOC_{IT}. However, an adapting evaporation pressure of the ice tank is advantageous for several reasons. If the evaporation temperature is very low, the transferred heat is larger due to the larger temperature difference and thereby the superheat of the CO_2 exiting the ice tank increases, which can cause high discharge temperatures. A larger superheat decreases furthermore the effectiveness of the evaporator, since the superheat decreases the driving temperature difference for heat transfer and thereby is the area reduced, in which heat is transferred using a higher temperature difference. Besides the changes in the heat transfer characteristics, the pressure ratio Π changes and consequently the required LT and MT compressor work.

Hence, the previous control of the ice tank charging, which consists of a PI controller controlling the mass flow rate at a fixed inlet pressure, is replaced by a simplified LT compressor model.

The setup of the LT compressor model is shown in Figure 5.9, which shows the flow-chart that determines the mass flow of CO_2 through the ice tank. The compressor model takes two boundaries into account, the maximum compressor work $\dot{W}_{comp,max}$ and the maximum volume flow rate $\dot{V}_{comp,max}$. The PI controller controls the evaporation pressure such that the outlet of the CO_2 exits the ice tank at $x = 1$. Based on the set evaporation pressure,

the specific compressor work Δh_{comp} is calculated based on eq. 5.4.

$$\Delta h_{comp} = \frac{(h_{2s} - h_1)}{\eta_{is}} \tag{5.4}$$

Based on the specific compressor work Δh_{comp}, the maximum mass flow of CO_2 is calculated with the max. compressor work $\dot{W}_{comp,max}$, as Eq. 5.5 shows.

$$\dot{m}_{lim,\dot{W}_{max}} = \frac{\dot{W}_{comp,LT,max}}{\Delta h_{comp}} \tag{5.5}$$

$$\dot{m}_{lim,\dot{V}} = \dot{V}_{comp,LT,max} \cdot \rho(p_{evap,LT}, h_{R,out}) \tag{5.6}$$

If the mass flow of CO_2 calculated based on the max. compressor work is larger than the mass flow of CO_2 , which could be compressed based on the swept volume (calculated in Eq. 5.6), the mass flow of the swept volume is taken as the output of the compressor model. This represents the boundary of the max. rotational speed of the compressor.

If the mass flow of CO_2 calculated using the swept volume ($\dot{m}_{lim,\dot{V}}$) is larger than the mass flow calculated based on the max. compressor work ($\dot{m}_{lim,\dot{W}_{max}}$), the mass flow based on the maximum compressor work ($\dot{m}_{lim,\dot{W}_{max}}$) is taken as the output of the LT compressor model. This represents the limitation of the maximum allowable compressor work.
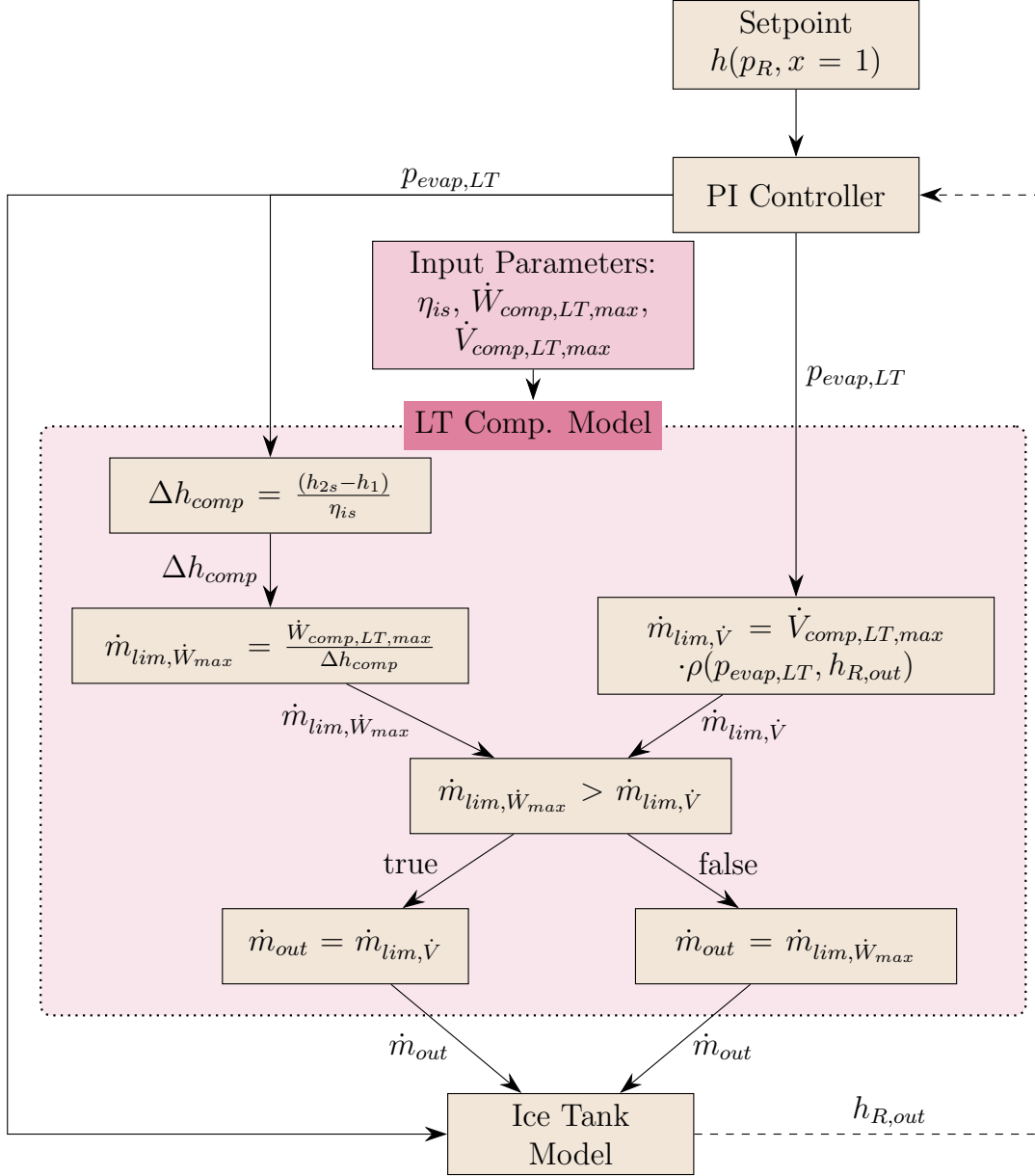
Figure 5.9: LT compressor model

5.4.1 Results of the LT Compressor Model Change

The following results only present the charging / off-peak period of the system, since the change in the LT compressor model does not affect the on-peak period. Hence, Figure 5.10 shows the result of the LT compressor model update.

The first subplot of Figure 5.10 shows the operation mode of the system, which changes from $OM = 4$ to $OM = 12$ at $t = 4.75\,\text{h}$. At $t = 7.5\,\text{h}$, the operation mode OM is changed back to $OM = 4$.

The second subplot of Figure 5.10 shows the LT and MT compressor work. The LT compressor operates during the off-peak period at the setpoint of the maximum compressor work, except for the time $t = 0.81\,\text{h} - 1.5\,\text{h}$, where the compressor work reduces to a

minimum of $\dot{W}_{LT,comp,max} = 8.51\,\text{kW}$ at $t = 1.38\,\text{h}$. At $t = 6.97\,\text{h}$, the LT compressor is turned off, as soon as the SOC_{IT} reaches $SOC_{IT} = 0.95$ (third subplot of Figure 5.10). The MT compressor work (second subplot Figure 5.10) increases during the charging process up to $\dot{W}_{MT,comp} = 30.39\,\text{kW}$ at $t = 1.44\,\text{h}$. Afterwards, the MT compressor work $\dot{W}_{MT,comp}$ decreases steadily until $t = 4.65\,\text{h}$, where a sharp decline occurs. At $t = 6.97\,\text{h}$, the MT compressor is turned off, and turned back on at $t = 7.5\,\text{h}$.
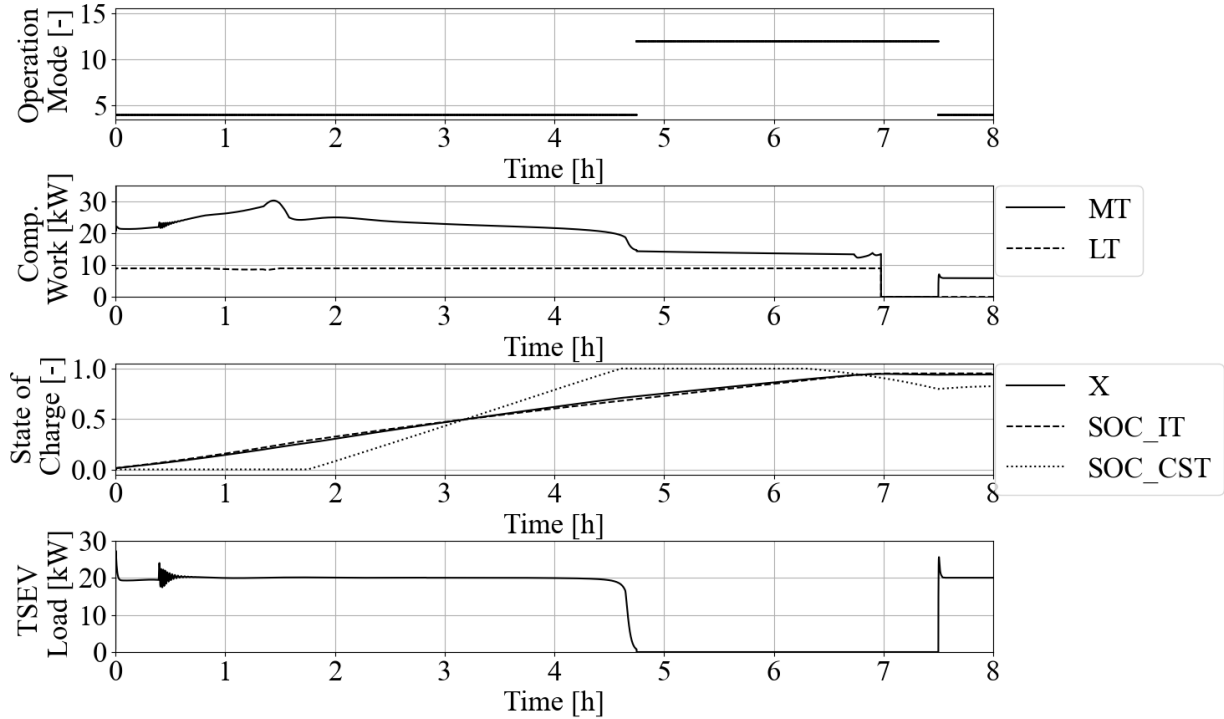
Figure 5.10: Results from the Improvement of the LT Compressor Model

The third subplot of Figure 5.10 shows the state of charge of the TES X, the ice tank SOC_{IT} and the cold water storage tanks SOC_{CST}. As mentioned previously, the SOC_{IT} increases steadily from $t = 0\,\text{h}$ and reaches $SOC_{IT} = 0.95$ at $t = 6.97\,\text{h}$. The SOC_{IT} remains constant afterwards during the charging period. The SOC_{CST} increases between $t = 1.75 - 4.61\,\text{h}$ from $SOC_{CST} = 0 - 1$. It remains at $SOC_{CST} = 1$ until $t = 6.29\,\text{h}$, where the SOC_{CST} decreases until $SOC_{CST} = 0.8$ at $t = 7.5\,\text{h}$. Between $t = 7.5 - 8\,\text{h}$, the SOC_{CST} increases to $SOC_{CST} = 0.82$ at $t = 8\,\text{h}$. The state of charge X follows the SOC_{IT} line closely and reaches $X = 0.94$ at $t = 8\,\text{h}$.

The TSEV load is shown in the fourth subplot of Figure 5.10. The TSEV load remains, besides an oscillation phase between $t = 0.4 - 0.65\,\text{h}$ at $\dot{Q}_{TSEV} \approx 20\,\text{kW}$. The load on the TSEV is sharply decreased to $\dot{Q}_{TSEV} \approx 0\,\text{kW}$ at $t = 4.75\,\text{h}$ and the TSEV load $\dot{Q}_{TSEV}$ shows a jump at $t = 4.5\,\text{h}$.

5.4.2 Discussion of the LT Compressor Model Change

The implementation of the LT compressor control works as intended, since the ice tank is charged at an adaptive CO_2 evaporation pressure and always at the maximum possible LT compressor work within the set boundaries. The limitation by the maximum swept volume takes effect at $t = 0.81\,\mathrm{h} - 1.5\,\mathrm{h}$, since the compressor work reduces from its setpoint value, as the second subplot of Figure 5.10 shows.

Since the mass flow rate of CO_2 changes within the ice tank, the MT compressor load changes accordingly and peaks at a rather high MT compressor demand. Considering that the MT compressor is dependent on the load of the TSEV and the ice tank, it would be interesting for further simulations to investigate if it is possible to operate the TSEV at part load conditions and thereby decrease the peak load of the MT compressor and maintain a more stable MT compressor load.

Furthermore, the adaption of CO_2 evaporation pressure in the ice tank combined with the lower, maximum LT compressor load of $\dot{W}_{LT,comp,max} = 9\,\mathrm{kW}$ does increase the charging time of the ice tank slightly from $t = 6.31\,\mathrm{h}$ to $6.97\,\mathrm{h}$ compared to the ventilation-updated simulation from chapter 5.3. However, the LT compressor can operate almost at all times at a constant capacity, which would ideally be the design point of the compressor and thereby create an efficient compressor operation.

One could argue that it would be beneficial to operate at even lower ice tank charging rates, since within this simulation, the charging requires $t = 6.97\,\mathrm{h}$ of the 9 h off-peak time. This should be determined based on the individual case, to accommodate a certain buffer time as a backup.

The oscillations of the TSEV load can occur due to the interaction of the different PI controllers, however, due to the limited appearance, no immediate action is required.

6 Experimental Work

The novel two-stage evaporator configuration requires besides its simulational investigations an experimental validation. Therefore, an experimental test facility is set up in the laboratories of the NTNU / SINTEF energy engineering lab. It consists of a multifunctional CO_2 test rig delivered by ENEX, which offers different possibilities to extend the system for individual research purposes. The following chapter 6.1 introduces the delivered test unit by ENEX, and chapter 6.2 the test rig setup of the two stage evaporator configuration, which is connected in parallel to the expansion valve.

As part of this work, a re-build of the two stage evaporator was accompanied and a test campaign should have been carried out. However, due to difficulties during the commissioning of the test rig and occurring system failures, it was only possible to conduct limited, preliminary tests. Hence, a full test campaign is required to present fully matured results, which was not possible due to the given time-frame of the thesis and the emerging delays. Hence, the later on presented results can only be treated as preliminary results.

6.1 Multifunctional CO_2 Test Rig

The multifunctional CO_2 test rig by ENEX is delivered as a pre-assembled unit, that is connected to the instrumentation devices, electrical power and local water network. The cold water supply exchanges heat within an additional gas cooler to control the CO_2 gas cooler exit temperature and to maintain a steady-state energy balance of the system.
The ENEX system consists of two evaporation temperature levels with an LT compressor to cover the LT cooling load and compress CO_2 to the suction pressure level of the MT compressor. The evaporator loads are generated by a closed glycol loop that is connected to the gas cooler. The process diagram is attached in Appendix A.1 in Figure A.1. The dashed box in Figure A.1 shows the two stage evaporator extension, which will be presented in detail in the next chapter 6.2.

6.2 Two Stage Evaporator Test Setup

The two stage evaporator extension is connected to the ENEX part in parallel to the expansion valve. The process and instrumentation diagram is shown in Figure 6.1. A low pressure, multi cartridge ejector by Danfoss of type CTM 6 acts as the expansion device and discharges into the tank. The dimensions of the tubes are, unless indicated differently, $d_i = 14$mm and $d_o = 21$mm. The dimensions of the two-stage evaporator, which is a brazed plate heat exchanger, are presented in Table 6.1. The liquid volume of the tank are $V_{r,tank} = 210$L.

Table 6.1: Two-Stage Evaporator Dimensions

Parameter	Value	Parameter	Value
Number of plates [−]	40	Wall Thickness [mm]	0.5
Plate Length [mm]	400	Pattern Amplitude [mm]	2.9
Plate Width [mm]	155	Pattern Wavelength [mm]	6
Pattern Angle [°]	22.5		
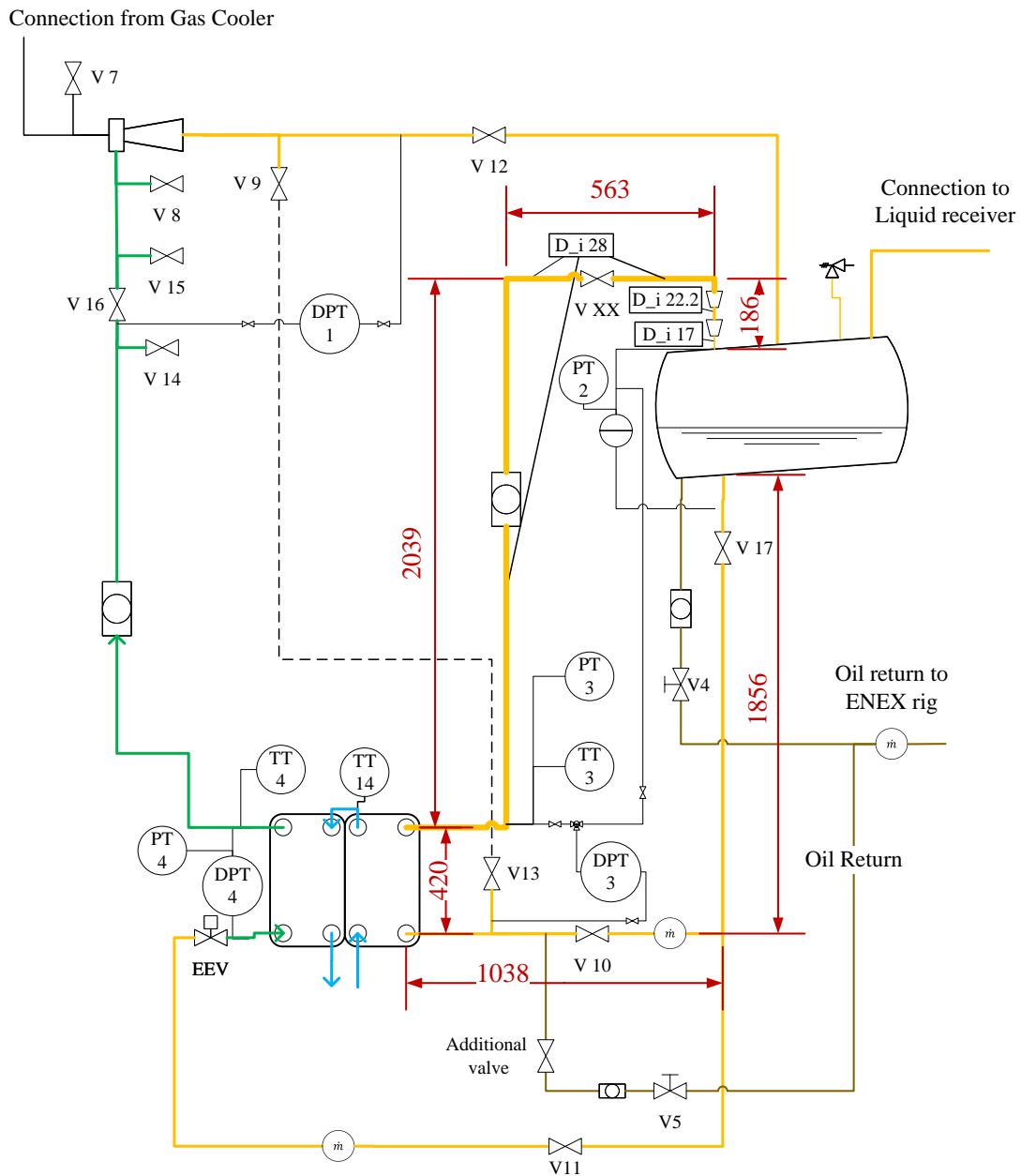
Figure 6.1: Process and Instrumentation Diagram of the Two Stage Evaporator Extension. Measurements are in mm

7 Results

The following chapter presents firstly results from the ice tank model to determine differences in the energy balance. Afterwards are results of the proposed system presented, which include the changes from the previous chapter 5. Chapter 7.3 presents results gained through the limited, preliminary tests of the experimental test rig.

7.1 Ice Tank Energy Balance

As the ice tank model is created from scratch, it requires ideally a verification against experimental test data. Due to the unavailability of such data, the ice tank model will be tested comparing the energy balance between the fluid flows to the change in internal energy. Therefore, a test simulation is carried out with the following test conditions of Table 7.1.

Table 7.1: Input Parameters for the Test of the Ice Tank Model Energy Balance

Discharging Conditions	
Water mass flow rate	$\dot{m}_w = -0.2 \text{ kg s}^{-1}$
Water inlet temperature	$T_w = 293 \text{ K}$
Initial ice layer	$\delta_{i,init} = 0.1 \text{ m}$
Charging Conditions	
Inlet enthalpy CO_2	$h_{CO_2} = 170 \text{ kJ kg}^{-1}$
Inlet pressure CO_2	$p_{CO_2} = 21 \text{ bar}$
Mass flow rate CO_2	$\dot{m}_{CO_2} = 0.005 \text{ kg s}^{-1}$
Initial ice layer	$\delta_{i,init} = 0 \text{ m}$
Tank Geometry	
Volume (Width x Depth x Height)	$V = 1\text{m} \cdot 1\text{m} \cdot 1\text{m} = 1 \text{ m}^3$
Diameter of CO_2 tubes	$d_{tubes,CO_2} = 0.02 \text{ m}$
Number of tubes	$n_{tubes} = 15$
Initial water temperature	$T_{w,init} = 0 \text{ °C}$
Thickness tubes	$\delta_{tube} = 0.002 \text{ m}$
Number of cells	$n_{cells} = 5, 20, 40, 60$

Based on the test parameters from Table 7.1, Figure 7.1a shows the result of the deviation in energy balance between the refrigerant and the ice tank after a charging cycle for a different number of cells. Negative results express a higher transferred energy onto the refrigerant than on the ice formation. The deviation in energy balance is within -0.08% at $n_{cells} = 60$ and -0.104% at $n_{cells} = 5$. Furthermore, the lowest number of cells $n_{cells} = 5$ shows a larger deviation with -0.104% than higher cell numbers.

Figure 7.1b shows similarly the deviation in energy balance for the discharge conditions. Negative results express that the energy transferred from the ice to the water is smaller
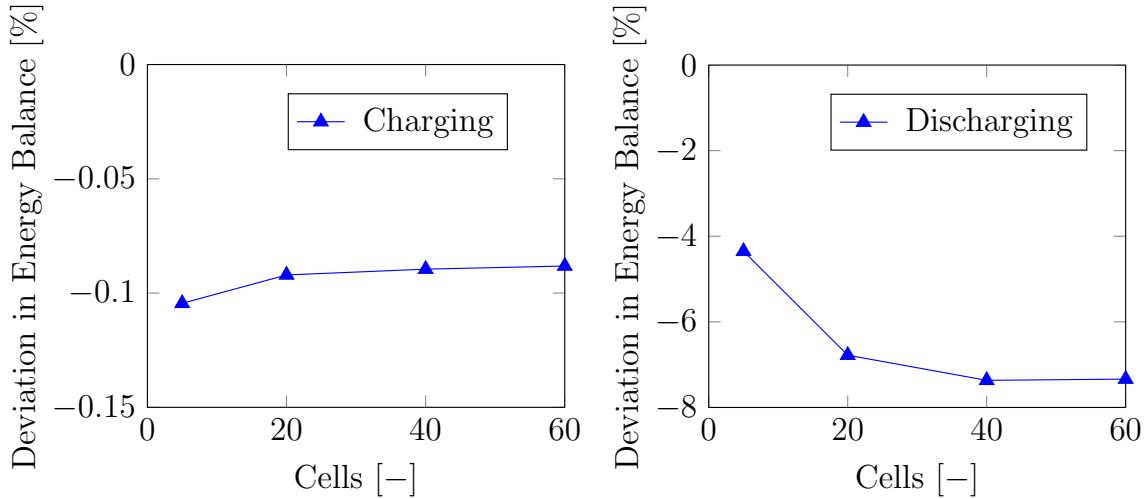
(a) Deviation in the Energy Balance between Refrigerant and Ice Formation during Charging

(b) Deviation in the Energy Balance between Water Flow and Ice Reduction during Discharging

Figure 7.1: Deviation in Energy Balance during Charging and Discharging

than the energy change which is measured within the water. The deviation in energy balance shows an asymptotically course with a higher deviation towards higher cell numbers. The energy balance deviation ranges from $-4.35\,\%$ at $n_{cells} = 5$ to $-7.36\,\%$ at $n_{cells} = 40$.

7.2 System Performance for Exemplary Data

Throughout chapter 5 is the system improved by the presented measures. Therefore, Table 7.2 shows an overview over the parameters and sub-models used for the concluding simulation. In addition, the chapter that describes the specific parameter or component is included in Table 7.2. Alternatively, a brief overview over the utilized model provides the attached draft scientific article in chapter A.4. The following Figures 7.2 - 7.4 show the results for the system configuration with the input parameters from Table 7.2. Within all of the presented results, the off-peak period is marked in white, the on-peak - min. use of storage period is marked in light grey and the on-peak - max. use of storage period is marked in dark grey. By the sizing of the cold water storage tank and ice tank contains the cold water storage tank 8.77 % of the total TES capacity.

The AC load on the control volume, presented in the first subplot of Figure 7.2, remains unchanged compared to the initial simulation from 5.2.2. Hence, during the off-peak period from $t = 23 - 8\,\mathrm{h}$, the AC load remains lower and shows high loads during the on-peak period from $t = 8 - 23\,\mathrm{h}$. The AC load peaks during the on - peak period at $t = 16\,\mathrm{h}$ with $\dot{Q}_{AC,load} = 60.1\,\mathrm{kW}$.

The operation mode deviates between $OM = 4$ and $OM = 12$ during the off-peak period

Table 7.2: Overview of Selected Parameters and System Components and their Description within the Thesis

Component	Model Type	Selected Parameters	Chapter
TSEV	Non-linear regression model		4.3.3.1
		$\dot{Q}_{TSEV,design} = 20\,\text{kW}$	5.2.1
LT compressor	Simplified Compressor Model		5.4
		$\dot{V}_{LT,comp,max} = 0.005\,\text{m}^3\,\text{s}^{-1}$	5.4
		$\dot{W}_{LT,comp,max} = 9\,\text{kW}$	5.4
		$\eta_{is} = 0.7$	4.3.3.1
Ice Tank	Simplified Ice Tank Model		4.3.2
		Ice Tank size	5.1
		$\alpha_{\text{CO}_2} = 8000\,\text{W}\,\text{m}^{-2}\,\text{K}^{-1}$	5.2.1
		$\alpha_{\text{CO}_2} = 500\,\text{W}\,\text{m}^{-2}\,\text{K}^{-1}$	5.2.1
		$h_{R,in} = h(x = 0, p = 39\,\text{bar}) = 210.7\,\text{kJ}\,\text{kg}^{-1}$	
Cold Storage Tanks	Modeled as tube		4.3.4
		$n_{cells} = 30$	5.2.1
		$V_{tank} = 3\,\text{m}^3$	5.2.1
		$D_{CST,tank} = 1\,\text{meter}$	5.2.1
		$V_{exp.Tank} = 100\,\text{L}$	5.2.1
AHU	Air - water heat exchanger		
		$\alpha_{air} = 65\,\text{W}\,\text{m}^{-2}\,\text{K}^{-1}$	5.2.1
		$\alpha_{w} = 1000\,\text{W}\,\text{m}^{-2}\,\text{K}^{-1}$	5.2.1
		AHU size	5.2.1
		$T_{room,sp} = 22\,°\text{C}$	5.2.1
		$\dot{V}_{fan,max} = 4\,\text{m}^3\,\text{s}^{-1}$	5.3
Pumps	Modellica Class Simple Pump		
		$\dot{m}_{MP} = 4\,\text{kg}\,\text{s}^{-1}$	5.2.1
		$\dot{m}_{MP} = 3\,\text{kg}\,\text{s}^{-1}$	5.2.1
Initialization / External Inputs			
		$T_{w,init} = 5\,°\text{C}$	5.2.1
		$T_{CST,init} = 15\,°\text{C}$	5.2.1
		$t_{on-peak,start} = 8\,\text{h}$	5.2.1
		$t_{on-peak,start} = 23\,\text{h}$	5.2.1
		downshift threshold $= 0.3$	
		$\dot{Q}_{ch,min} = 2\,\text{kW}$	5.2.1
		$X_{min} = 0.0001$	5.2.1
		AC Load Profile	5.2.2

and is shown in the second subplot of Figure 7.2. At $t = 4.75\,\mathrm{h}$, the operation changes from $OM = 4$ to $OM = 12$ and at $t = 7.5\,\mathrm{h}$ back to $OM = 4$. During the on-peak - min. use of TES period, the OM remains initially at $OM = 4$ within $t = 8 - 8.25\,\mathrm{h}$, and changes afterwards between $OM = 10, 15, 13$ until $t = 19.25\,\mathrm{h}$. Within the on-peak max. use of storage period ($t = 19.25-23\,\mathrm{h}$), the operation mode changes between $OM = 11, 14$.

The State of Charge (SOC) of the TES is shown in the third subplot of Figure 7.2. The SOC_{CST} remains at $SOC_{CST} = 0$ initially and increases between $t \approx 1.75 - 4.6\,\mathrm{h}$ to $SOC_{CST} = 1$. It remains at $SOC_{CST} = 1$ until $t = 6.29\,\mathrm{h}$. Afterwards, the SOC_{CST} decreases until $SOC_{CST} = 0.4$ at $t = 11.39\,\mathrm{h}$, and shows an increasing trend until a plateau, subsequently. During the on-peak - max. use of storage period, the SOC_{CST} decreases onto a plateau and shows a sharp decrease at $t \approx 21.5\,\mathrm{h}$.
The SOC_{IT} increases from $t = 0\,\mathrm{h}$ until it reaches $SOC_{IT} = 0.95$ at $t = 7.77\,\mathrm{h}$. Within the on-peak period, the SOC_{IT} decreases gradually until it reaches $SOC_{IT} = 0.15$ at $t = 23\,\mathrm{h}$. The combined state of charge of the TES X follows the SOC_{IT} closely within the 24 h period.

The room temperature T_{room} stays within $\pm 0.5\,\mathrm{K}$ of the setpoint of $T_{room,SP} = 22\,°\mathrm{C}$, as it can be seen in the fourth subplot fo Figure 7.2. T_{room} shows the highest fluctuations during the beginning of the on-peak period, when the OM's fluctuate between $OM = 10, 13, 15$. If the OM remains constant over a certain period of time, approx. 3-4 h, the system steadily approaches the setpoint temperature.

Figure 7.3 shows the compressor and system loads. The first subplot of Figure 7.3 shows the LT and MT compressor work $\dot{W}_{LT,comp}$ and $\dot{W}_{MT,comp}$, respectively. During the off-peak period, the LT compressor operates at $\dot{W}_{LT,comp} = 9\,\mathrm{kW}$, except between $t = 0.79 - 1.91\,\mathrm{h}$. At $t = 7.6\,\mathrm{h}$, the LT compressor shuts off and remains inactive until the end of the on-peak period.
The MT compressor peaks at $\dot{W}_{MT,comp} = 29.98\,\mathrm{kW}$ at $t = 1.72\,\mathrm{h}$ during the off-peak period. Prior to the $\dot{W}_{LT,comp}$ showing a load of $\dot{W}_{LT,comp} = 0\,\mathrm{kW}$ at $t = 7.6\,\mathrm{h}$, the $\dot{W}_{MT,comp}$ peaks at a local maximum of $\dot{W}_{MT,comp} = 25.46\,\mathrm{kW}$ at $t = 7.51\,\mathrm{h}$. During $t = 7.6 - 19.25\,\mathrm{h}$ stays the $\dot{W}_{MT,comp}$ at $\dot{W}_{MT,comp} = 5.3 - 5.9\,\mathrm{kW}$, depending on the operating conditions. Within the maximal use of storage period ($t = 19.25 - 23\,\mathrm{h}$), both compressors remain inactive.

The second subplot of Figure 7.3 shows the temperature of water entering and exiting the TSEV, and the third subplot shows the TSEV load. During off-peak periods, when the TSEV is active, hence a load is posed onto the TSEV, the temperature difference

General System Overview
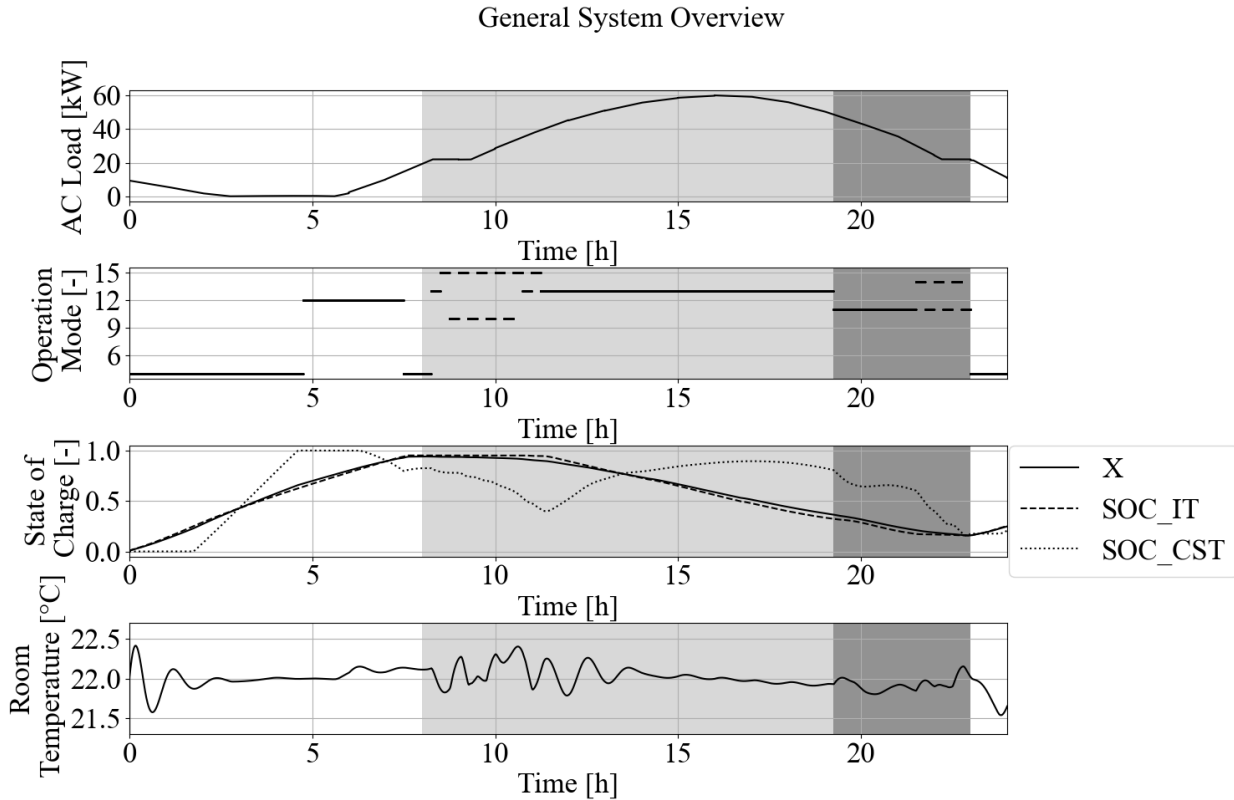
Figure 7.2: Results from the Concluding Simulation 1/3. On-peak Period is marked in grey, Minimal Use of TES in light grey and Maximal Use of TES in dark grey

of water across the TSEV is higher, as the inlet temperature $T_{TSEV,w,in}$ is higher (up to $T_{TSEV,w,in} = 15\,°C$). During the on-peak period, at times where a load is applied on the TSEV, the $T_{TSEV,w,in}$ reads lower values (up to $T_{TSEV,w,in} = 10\,°C$). The TSEV load in the third subplot remains at approx. $\dot{Q}_{TSEV} = 20\,kW$, in the case that the TSEV is active. Between $t = 8.5 - 10\,h$ shows the TSEV load some unsteadiness to a certain extent. During the on-peak - max. use of storage period remains the load on the TSEV at $\dot{Q}_{TSEV} = 0\,kW$. Furthermore, the TES achieves that 65 % of the required on-peak capacity is being produced within the off-peak period.

The fourth subplot of Figure 7.3 shows the predicted load during the on-peak period and the TES capacity over the 24 h period. During the off-peak period stays the predicted load constant and shows a continuous decrease to $Q_{load,predicted} = 0\,GJ$ until the end of the on-peak period. At the beginning of the on-peak period at $t = 8\,h$, the predicted load during the on-peak period is $Q_{load,predicted} = 3.05\,GJ$.

The TES capacity increases during the off-peak period and reaches $Q_{TES,stored} = 1.64\,GJ$. From the on-peak period on, the TES capacity $Q_{TES,stored}$ decreases intersects with the predicted load $Q_{load,predicted}$ at $t = 19\,h$. The remaining TES capacity at the end of the

on-peak period is $Q_{TES,stored} = 0.27\,\text{GJ}$.

Compressor and System Loads
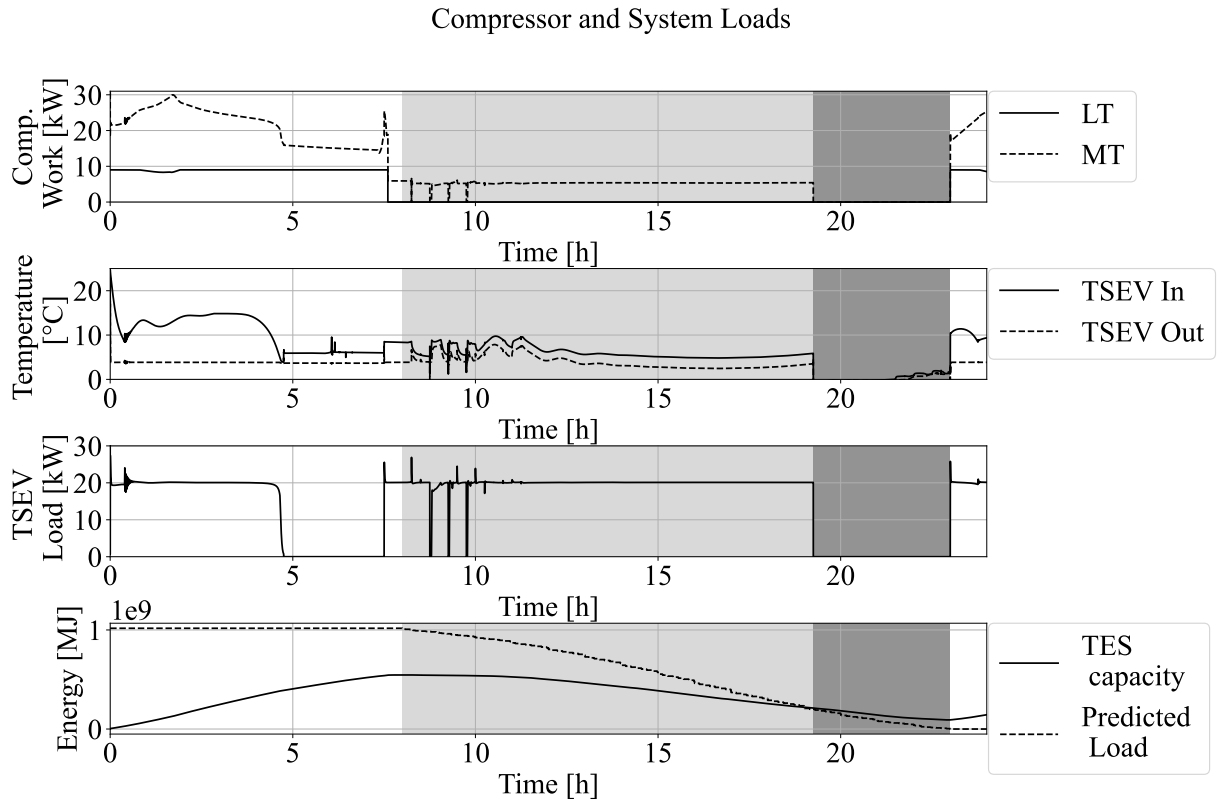
Figure 7.3: Results from the Concluding Simulation 2/3. On-peak Period is marked in grey, Minimal Use of TES in light grey and Maximal Use of TES in dark grey

The first subplot of Figure 7.4 shows the volume flow of air $\dot{V}_{air,AHU}$ through the AHU. During the on-peak period, $\dot{V}_{air,AHU}$ is lower than $\dot{V}_{air,AHU} \leq 2\,\text{m}^3\,\text{s}^{-1}$. During the on-peak period, the volume flow $\dot{V}_{air,AHU}$ increases and peaks at $t = 16.31\,\text{h}$ at $\dot{V}_{air,AHU} = 3.79\,\text{m}^3\,\text{s}^{-1}$

The second subplot of Figure 7.4 shows the logarithmic mean temperature difference $LMTD$. During the off-peak period, the $LMTD$ is below $LMTD \leq 4\,\text{K}$. The $LMTD$ increases during the on-peak period and peaks at $t = 16.35\,\text{h}$ with $LMTD = 8.61\,\text{K}$.

The third subplot of Figure 7.4 shows the air temperatures of air entering and exiting the AHU. The entering air is within $T_{air,AHU,in} = 22 \pm 0.5\,°\text{C}$ during the 24- h period. The exiting air of the AHU is during the off-peak period between at $T_{air,AHU,out} = 8.85\,°\text{C}$, besides the fluctuations occuring at $t = 4.75-6.04\,\text{h}$, where $T_{air,AHU,out}$ fluctuates between $T_{air,AHU,out} = 8.5 \pm 0.5\,°\text{C}$. During the on-peak period fluctuates $T_{air,AHU,out}$ initially and approaches $T_{air,AHU,out} \approx 8.56\,°\text{C}$, until the max. use of storage period is reached, where

Air Handling Unit
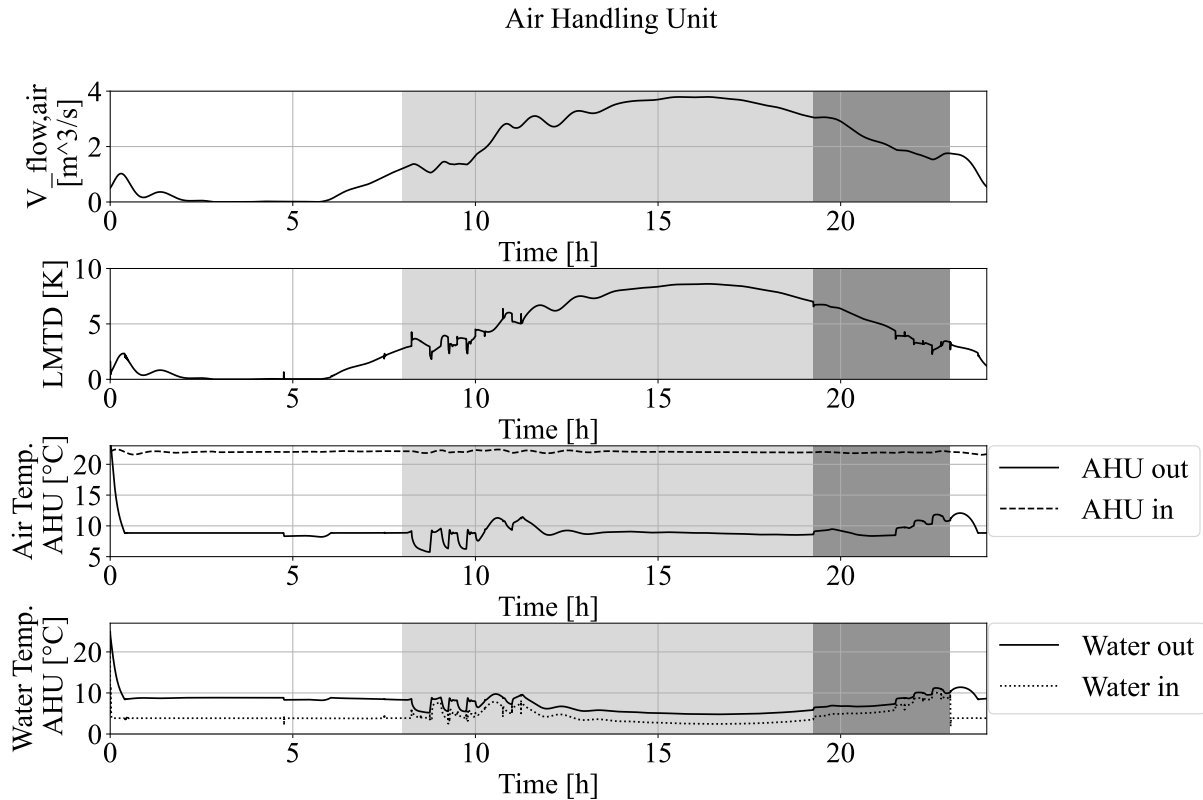
Figure 7.4: Results from the Concluding Simulation 3/3. On-peak Period is marked in grey, Minimal Use of TES in light grey and Maximal Use of TES in dark grey

towards the end smaller fluctuations are observed.

The fourth subplot of Figure 7.4 shows the water inlet and exit temperature of the AHU. The inlet temperature is during the the off-peak period $T_{w,AHU,in} = 4\,°C$ with $T_{w,AHU,in} \approx 8.85\,°C$. During the on-peak - min. use of storage period fluctuates the supply and return water initially and stabilises towards $t \approx 12\,h$. During the constant $OM = 13$ reaches the inlet and exit water flow a local minima of $T_{w,AHU,in} = 2.45\,°C$ and $T_{w,AHU,in} = 4.8\,°C$ between $t = 16.6 - 16.7\,h$. During the on-peak period with max. use of storage operation increase the water temperatures and show further smaller fluctuations.

7.3   Experimental Work

Preliminary tests on the two stage evaporator configuration were carried out for the following test parameters:

- Water inlet temperature $T_{w,in} = 15\,°\text{C}$

- Liquid receiver pressure $p_{rec} = 44\,\text{bar}$

- Water mass flow $\dot{m}_w = 24,\ 30,\ 36,\ 42\,\text{kg min}^{-1}$

- Electronic expansion valve (EEV) opening $EEV = 20, 30, 40\,\%$

To determine the repeatability of the experiments is the test condition of $T_{w,in} = 15\,°\text{C}$, $p_{rec} = 44\,\text{bar}$, $\dot{m}_w = 30\,\text{kg min}^{-1}$ and $EEV = 30\%$ repeated three times. The resulting loads on the gravity fed and ejector fed part of the two stage evaporator are presented in Table 7.3. Evaporator loads are determined through an energy balance on the secondary fluid. Through Table 7.3 one obtains that the gravity fed evaporator load $\dot{Q}_{GFE}$ deviates between $\dot{Q}_{GFE} = 7.09 - 8.95\,\text{kW}$ and the ejector fed evaporator load between $\dot{Q}_{EFE} = 9.44 - 11.63\,\text{kW}$ for test 1 - 3.

Table 7.3: Results obtained by Experiments for the Test Conditions of $T_{w,TSEV,in} = 15\,°\text{C}$, $p_{TSEV,GFE} = 15\,\text{bar}$, $\dot{m}_{w,TSEV,in} = 30\,\text{kg min}^{-1}$ and $EEV = 40\,\%$ through three measured Test Points

	Test 1	Test 2	Test 3
$T_{w,TSEV,in}\ [°\text{C}]$	15.00	15.07	15.04
$p_{TSEV,tank}\ [\text{bar}]$	43.99	43.97	43.91
$\dot{m}_{w,in}\ [\text{kg min}^{-1}]$	30.19	30.16	30.06
$EEV\ [\%]$	40	40	40
$\dot{Q}_{TSEV,GFE}\ [\text{kW}]$	8.95	7.09	8.11
$\dot{Q}_{TSEV,EFE}\ [\text{kW}]$	9.44	11.63	11.14
$\dot{Q}_{TSEV,total}\ [\text{kW}]$	18.39	18.72	19.24

Figure 7.5 shows the deviation per test point from the mean value of the data set for the gravity fed evaporator $\dot{Q}_{GFE}$ in Figure 7.5a and the entire two-stage evaporator $\dot{Q}_{TSEV}$ in Figure 7.5b. The mean value of the gravity fed evaporator load of the test points 1 - 3 is $\dot{Q}_{GFE,Mean} = 8.05\,\text{kW}$ and of the TSEV is the determined mean value $\dot{Q}_{TSEV,Mean} = 18.79\,\text{kW}$. The load on the gravity fed evaporator deviates, as Figure 7.5a shows, between $\pm 12\,\%$ and the total load on the TSEV $\pm 2.5\,\%$, as Figure 7.5b shows.

Figure 7.6 shows the experimental result of three additional test series. Figure 7.6a shows the two-stage evaporator load over the water mass flow $\dot{m}_{w,in} = 24 - 42\,\text{kg min}^{-1}$. The two-stage evaporator load increases approximately linear from $\dot{Q}_{TSEV} = 15.29\,\text{kW}$ at $\dot{m}_{w,in} = 24\,\text{kg min}^{-1}$ to $\dot{Q}_{TSEV} = 24.21\,\text{kW}$ at $\dot{m}_{w,in} = 42\,\text{kg min}^{-1}$.
Figure 7.6b shows the two-stage evaporator load $\dot{Q}_{TSEV}$ over the electronic expansion valve
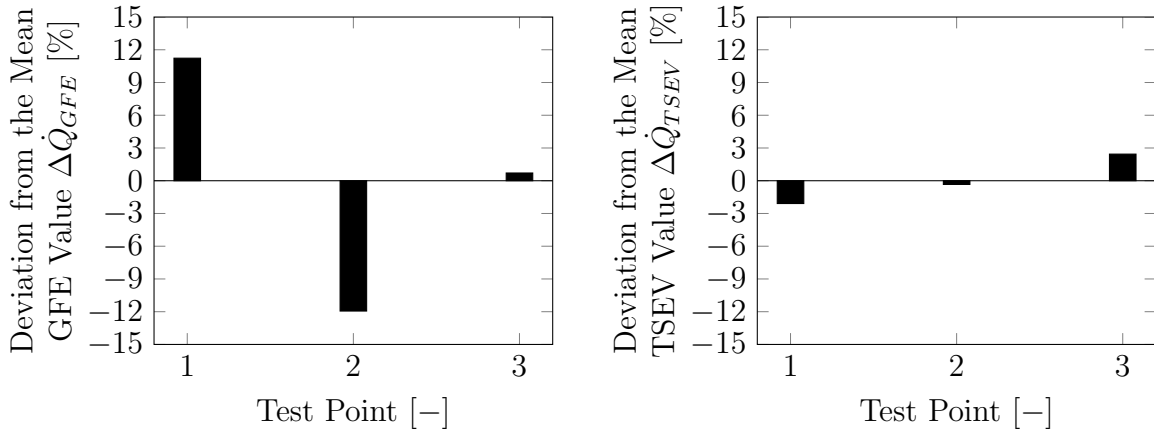
(a) Deviation of the Gravity Fed Evaporator Load $\dot{Q}_{GFE}$ from the Mean Value of Test 1 -3

(b) Deviation of the Two-Stage Evaporator Load $\dot{Q}_{TSEV}$ from the Mean Value of Test 1 -3

Figure 7.5: Deviation of the TSEV Load of the Gravity Fed Part and entire Heat Exchanger from the Mean Value of the respective Load $\dot{Q}$

(EEV) opening. For a mass flow rate of $\dot{m}_{w,in} = 24\,\mathrm{kg\,min^{-1}}$, the two-stage evaporator load $\dot{Q}_{TSEV}$ decreases for an increasing opening of the EEV from $\dot{Q}_{TSEV} = 15.78\,\mathrm{kW}$ at $EEV = 20\%$ to $\dot{Q}_{TSEV} = 15.29\,\mathrm{kW}$ at $EEV = 40\%$. At a higher water mass flow rate of $\dot{m}_{w,in} = 30\,\mathrm{kg\,min^{-1}}$, the two-stage evaporator load shows a local maxima at $EEV = 30\%$ with $\dot{Q}_{TSEV} = 19.2\,\mathrm{kW}$.
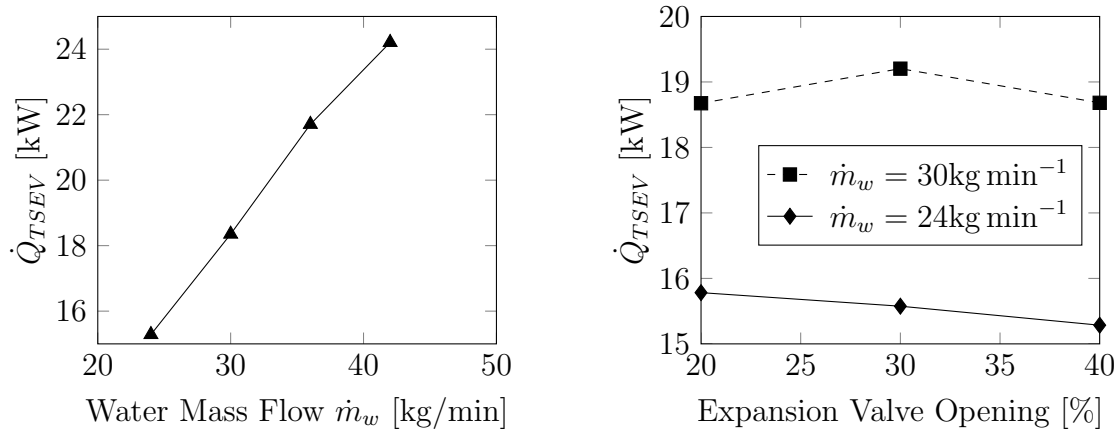
(a) Two-Stage Evaporator Load $\dot{Q}_{TSEV}$ over the Water Mass Flow Rate of $\dot{m}_w = 24 - 42\,\mathrm{kg\,min^{-1}}$ and $T_{w,in} = 15\,°\mathrm{C}$, $p_{rec} = 44\,\mathrm{bar}$ and $EEV = 40\%$

(b) Two-Stage Evaporator Load $\dot{Q}_{TSEV}$ over the Electronic Expansion Valve (EEV) Opening of $EEV = 20 - 40\%$ and $\dot{m}_w = 24\&30\,\mathrm{kg\,min^{-1}}$, $T_{w,in} = 15\,°\mathrm{C}$ and $p_{rec} = 44\,\mathrm{bar}$.

Figure 7.6: Further Preliminary Experimental Results for different Test Conditions

8 Discussion

The discussion of the gained results is divided into the discussion of the ice tank energy balance results, the dicussion of the entire system results and a discussion of the experimental results.

8.1 Ice Tank Energy Balance

To investigate on the accuracy of the ice tank model is a comparison between the stored energy and energy transferred to the fluid carried out, with the results presented in chapter 7.1.
Within the charging process, the energy balance between the stored energy and the refrigerant flow showed deviations smaller than 0.15%. This result is regarded as sufficiently accurate, since the effects imposed by the made assumptions outweigh the charging energy balance deviation. In detail:
The impact on the overall system characteristics and charging time by the made assumptions, such as constant heat transfer coefficients or the unhindered expansion of the ice fronts (see chapter 4.3.2) would outweigh the impact that results from the deviation in energy balance while charging.

During the investigated discharging cycle rises the deviation of the energy balance to higher numbers (up to -7.36 %), as presented in Figure 7.1b. Even though the deviation in energy balance during discharging approaches shows smaller increases and reaches somewhat steady values for high cell numbers, a deviation of up to -7.36 % cannot be disregarded. A possible cause could not be found within the time frame of the master thesis, but it is expected that the cause lies within the Modelica code rather than the utilized governing equations.

For further work, a comparison of the energy imbalance under different charging and discharging conditions could provide insights into the cause of the imbalance. Besides investigating further into the deviation of the energy balance, a verification of the model against experimental data would be advantageous. Thereby, uncertainties of the ice tank model would be determined and the credibility of the ice tank model be solidified.

8.2 CO_2 Heat Pump and Hydronic System Performance for Exemplary Data

Generally should the presented results on the simulation be regarded as a proof of concept instead of a finished simulation due to the made assumptions, uncertainties regarding the

energy balance of the ice tank and exemplary tube sizes. Therefore, if the results from the simulations indicate that the benefits of the proposed system outweigh the system complexity (and for actual scenarios the additional investment costs), further investigations are required.

Since the simulation offers plenty of possibilities for discussions, the discussion is divided into two parts. The first part in chapter 8.2.1 is an in-depth model-based discussion of the performance of the system during the on- and off-peak period. Afterwards discusses chapter 8.2.2 overall topics, which occur during the 24-h period.

8.2.1 Parameter Based Discussion

The following chapters provide an in-depth model based discussion of the gained results from chapter 5.2.

8.2.1.1 Off-Peak Period TES Charging

Prior to going into detail of the compressor and TSEV operation, it should be noted that the implemented system regulation is capable of keeping the control volume / room temperature within ± 0.5K of the setpoint condition, which ensures sufficient indoor thermal comfort.

During TES charging operates the LT compressor constantly at its design / maximum compressor capacity (see first subplot of Figure 7.3) whiles the evaporation pressure is adapted. Furthermore, the implemented LT compressor boundaries work as intended, as previously discussed in chapter 5.4. It can therefore be concluded that the LT compressor model operates as intended within the simulation.

The current simulation does not consider the change in volumetric and isentropic efficiency due to the increase of the pressure ratio Π while ice tank charging. This change in volumetric and isentropic efficiency affects the required LT compressor work and pressure ratio dependent functions of the volumetric and isentropic efficiency should be included for further simulations. Especially if the target of the simulations shift from the current proof of concept state towards a specific application state.

The MT compressor work shows a high peak during the TES charging period, as presented in the first subplot of Figure 7.3. Since the MT compressor unit covers the load by the ice tank and the TSEV, an increase in mass flow of CO_2 in one of those results in an increased MT compressor unit work. To avoid high peak loads of the MT compressor unit could the main pump potentially regulate the charging speed of the cold storage tanks within the TES charging period. Thereby, the load on the TSEV is reduced and consequently the MT compressor load related to the CST charging as well. If the main

pump is in communication with the MT compressor unit, a constant MT compressor load could be eventually achieved, if further investigations determine this as a potential for cost-savings. Not only could a load regulation on the TSEV be implemented during CST charging, but also on the ice tank, since both TES are fully charged before the start of the on-peak period. Slower TES charging rates would decrease the required (maximum) compressor work, but on the other hand increase the operating time. Hence, an evaluation would be required to determine an ideal TES charging speed depending on operating costs, equipment costs and electricity prices. Within the day-to-day operation, an AC load prediction would be additionally required to ensure that the TES is fully charged at the end of the off-peak period. Currently, the SOC_{CST} is between $SOC_{CST} = 0.8 - 1$ (third subplot Figure 7.2) due to the implemented charging boundaries (see chapter 5.3). However, since the current sizing of the CST results in 8.77 % of the total TES capacity, the effect of not entirely charge CST on the general performance of the system can be regarded low. This surely changes once the storage capacity of the CST is increased.

As presented in Figure 7.3, the TSEV load is besides a minor oscillation phase near the design condition of $\dot{Q}_{TSEV} = 20kW$ and therefore, one can conclude that the regulation of water flow through the pump / V2 is successful. During the charging phase of the CSTs is the return temperature to the TSEV generally higher than the return temperature during the on-peak period. Higher return temperatures are due to a higher initial temperature within the CSTs charging period.

Because of the reduced AC load during the charging phase, the volume flow of air is also reduced and thereby the $LMTD$ as well. Hence, with the current assumptions on the AHU, lower volume flow rates result in lower $LMTD$s. However, the constant heat transfer coefficient of the AHU should be exchanged by a heat transfer correlation, to represent the heat transfer coefficient changes due to fluid flow changes.

8.2.1.2   TES Discharge - Min. Use of Storage

Within the discharging - min. use of storage period, the peak AC demand of $\dot{Q}_{AC,peak} = 60.1kW$ occurs. Due to the high AC demands, the system operates with the OM, which offers the highest system capacity within this discharge strategy, $OM = 13$ (see Figure 7.2 fourth subplot). Hence, the operation mode control during discharge - min. use of storage operates correctly to the extent that the OM with the highest system capacity is chosen and maintains the room temperature within $\pm 0.5K$ of the setpoint indoor temperature (Figure 7.2).

Within the time where $OM = 13$ is active, as presented in Figure 7.2 (third subplot), the

SOC_{CST} increases, even though the CSTs are discharged. Because the setpoint condition for the air exiting the AHU is set to $T_{s,AHU} = 9°C$ leads to low water return temperatures to the ice and cold storage tanks. Hence, the cold storage tanks are charged, even though they are discharged simultaneously. This would change once the setpoint of the supply air is changed to higher values, which would be dependent on the present load, since high AC loads with higher supply air temperatures require higher air volume flow rates. Hence, the fan work would be increased.

The system is capable to maintain the supply air temperature setpoint, except at the beginning of the discharge - min. use of storage period (light grey area in third subplot of Figure 7.4). The deviation of the setpoint of the air supply temperature is caused by the fluctuations in the operation mode (second subplot of Figure 7.2). These fluctuations are observed during AC loads between $\dot{Q}_{AC,load} = 20 - 40\text{kW}$ within the discharge-min. use of storage period. Within the period of $t = 8.5 - 11.25$, the operation mode fluctuates in the beginning between $OM = 10$ and $OM = 15$, which corresponds to TSEV active, CST discharge and ice tank inactive for $OM = 10$ and ice tank active for $OM = 15$. Hence, the activation of the ice tank discharge increases the system capacity by a large step, which leads to the up- and downshift in the operation modes. Later within this period changes the OM between $OM = 15$ and $OM = 13$, which corresponds to TSEV active, CST discharge and ice tank discharge by either the main pump ($OM = 15$) or the ice tank pump ($OM = 13$).
The fluctuations indicate that the steps in system capacity due to the different operation modes are too large, since the higher system capacity operates below the set downshift-threshold value (see chapter 5.2.1), which leads to a downshift in system capacity and consequently a change in OM. The downshift in system capacity however is not sufficient to maintain the indoor temperature levels, which triggers the up-shift in system capacity and consequently a change in operation mode, leading to the observed fluctuations.

Solutions to the operation mode fluctuations could be to investigate the system discharge capacities and adapt the flow rates of the main pump and ice pump for more equal steps in system capacities when changing the OM. Alternatively, a change in the downshift threshold value could lead to an improvement if the downshift value is set to lower values. Thereby, operation modes with high system capacities compared to the present AC load would have a greater operation range, which makes a downshift in system capacity and change OM less likely, which would arguably improve the system stability.

Within the period of the operation mode fluctuations, the TSEV adapts rather quickly,

as the third subplot of Figure 7.3 shows. The fast adaption rate is due to the TSEV and CO_2 heat pump model, since no physical process, but an idealized process is modelled. Hence, system inertia due to fluid mass, heat transfer characteristics and system control is neglected, which results in the sharp TSEV capacity changes. Furthermore, the TSEV load shows adaption phases ($t = 8.82 - 9.13$h) until it reaches the design evaporator load. The cause for those slower adaptions is found in the PI controller. If the operation mode changes, and the PI controller of the main pump is required to actively regulate the mass flow, the regulated pump mass flow starts at $\dot{m}_{w,MP} = 0\,\mathrm{kg\,min^{-1}}$, which leads to low / zero TSEV evaporator load.

During the TES Discharge - min. use of storage period operates the MT compressor nearly constant at $\dot{W}_{MT,comp} = 5.3$kW due to the nearly constant load of the TSEV (first subplot of Figure 7.3). This is beneficial, since the compressor sizing can be adapted to the load, and the compressor can operate thereby at or near its design conditions, which gives a basis for high compressor efficiencies during operation. As the third subplot of Figure 7.3 indicates, the TSEV operates within the TES discharge - min. use of storage period at the design evaporator capacity of $\dot{Q}_{TSEV,Design} = 20$kW,

The increase of the $LMTD$ during the discharge-min. use of storage period (second subplot of Figure 7.4) is due to the increased mass flow rates, since the UA value remains constant due to the constant heat transfer coefficient. Hence, the $LMTD$ should be regarded carefully, since a change in volume flow rate does not affect the air side heat transfer coefficient $\alpha_{air,AHU}$ and the previously presented improvements to the AHU should be carried out. It is furthermore visible that the volume flow rate can cover the required AC load, since $\dot{V}_{air,AHU}$ does not reach the maximum setpoint of $\dot{V}_{air,AHU,max} = 4\mathrm{m^3\,s^{-1}}$. Volume flow rates of air of $\dot{V}_{air,AHU} = 4\mathrm{m^3\,s^{-1}}$ are high. Hence, within the application of the system within a building is the AHU most likely split into several smaller air handling units that require lower air volume flow rates.

As presented in the fourth subplot of Figure 7.3, once the predicted on-peak load meets the remaining TES capacity, a change from min. to max discharge of the TES is initiated. This indicates that the rule-based discharge control strategy operates accordingly, since the condition from Equation 3.1 is fulfilled.

8.2.1.3 TES Discharge - Max. Use of Storage

Similar to the previous periods is the TES in capable of maintaining the indoor temperature within ±0.5K of its setpoint, as the fourth subplot of Figure 7.2 shows.

Ideally, at the end of the on-peak period would the SOC of the TES system be $X = 0$. This is especially relevant for the ice tank, since the ice layer that forms around the refrigerant tubes creates an isolation layer, which requires lower evaporation pressure. In

return, lower evaporation pressures lead to lower COPs of the CO_2 heat pump system due to the increased pressure ratio. At the end of the TES Discharge - Max use of storage period and thereby at the end of the on-peak period, as presented in the third subplot of Figure 7.2, a $SOC_{CST} = 0.18$ and $SOC_{IT} = 0.15$ remains. Hence, even though the change from min. to max. use of storage is initiated correctly, as discussed in the previous chapter does X not reach $X = 0$ at the end of the on-peak period. This has two possible reasons. For one, the unintentional recharge of the CST provides additional capacity that was not accounted for (see Figure 7.2 third subplot). Furthermore, the energy imbalance of the ice tank influences, which was presented in chapter 7.1 and chapter 8.1, the SOC_{IT}. Hence, this energy balance deviation causes most likely the SOC_{IT} to not be fully discharged at the end of the off-peak period. Furthermore, inaccuracies in the load prediction and TES capacity measurement could potentially cause additional inaccuracies. Therefore, further investigations are required to determine the cause(s) of the remaining SOC of the ice tank and cold water storage tanks.

Similar to the min. use of storage operation shows the max. use of storage operation fluctuations in the OM between $\dot{Q}_{AC,load} = 20 - 30$kW. Within this period, the OM fluctuates between $OM = 11 - 14$. The operation modes correspond to CST and ice tank discharge with and without the ice tank pump, respectively. Therefore, the previously mentioned step in system capacity is too large or the downshift threshold value too high. The solutions are proposed as within the TES Discharge - Min. Use of Storage Period.

8.2.2 General Discussion

Generally, the system and system control is able to maintain the indoor setpoint temperature within an acceptable deviation of ±0.5K for the applied load profile. Furthermore, the system achieves to shift load from the on-peak period to the off-peak period, as well as peak load limiting operation, since the load during the on-peak period in the system does not exceed $\dot{Q}_{HP,evap} \approx 20$kW at AC loads of up to $\dot{Q}_{AC} \approx 60.1$kW, as it can be seen in the first subplot of Figure 7.3. Hence, since the main compressor work is carried out during the off-peak period, as presented in Figure 7.3 in the second subplot, the system would make us of dynamic electricity pricing if electricity prices during the off-peak period are lower than during the on-peak period. The cost savings are therefore dependent on the general electricity pricing and the fluctuation of it, since the rule based implementation assumes low electricity prices during the night and high prices during the day. A deviation of the cost profile reduces the cost savings and requires a different rule set, which was also concluded during the study by Selvnes et al.[21]. It is also necessary to investigate how much more compressor work is required to charge the ice tank compared to normal heat pump operation to cover the AC load.

Besides the system improvements, an economical evaluation is necessary to determine

whether cost savings due to the thermal energy storage operation outweigh the additional expenditures and operational costs within a reasonable time frame.

Influence of Input Parameters:

Besides the model-building, the component sizes and input parameters have a significant influence onto the results. Since the current simulation is carried out for exemplary data with exemplary sizes of the TES, AHU, tubes, etc., the current simulation provides preliminary insights into the system performance. Hence, a "real-life" application connected with a thorough analysis is required to determine optimized components sizes under the variety of different aspects, such as energy efficiency, operational cost savings, additional expenditures, operation complexity, etc.

Compressor / TSEV Unit:

During the charging period would a parallel compressor setup in the MT compressor unit be advisable, such that one compressor can cover the near constant load of the TSEV, and one adapts to the surplus load due to charging of the ice tanks, or other cooling loads from e.g. a freezer, cold storage room, etc.

The implemented non-linear regression model of the TSEV (presented in chapter 4.3.3.1) provides arguably acceptable results of the MT compressor work $\dot{W}_{comp}$. However, due to the limited amount of 30 test points for the regression model and the boundaries of the input parameters of the simulations by Bengsch[29] require to treat the result of the MT compressor work with care. Especially since the gas cooler pressure is set by Bengsch[29] to $p_{GC} = 120$bar.

For further simulations, a non-linear regression model based on a larger data set with a wider range of parameters would be advisable. Alternatively, an entire CO_2 heat pump model could be implemented in Dymola and provide additional insights on the system performance and dynamic behaviour, since the non-linear regression model does not consider effects due to the inertia of the system.

Generally, system inertia of the CO_2 heat pump is neglected in the calculated values of the TSEV load, and the LT and MT compressor work, which can be seen in sharp declines and jumps within those parameters. It is to be assumed that a physical system would have slower system responses, hence, those parameters should be treated as an ideal case.

If further (experimental) research finds optimal operating conditions for the TSEV setup, the system provides the ability to adapt. For instance, if a higher return temperature to the TSEV is desired to make use of the potential of a larger water temperature glide, the setpoint of the air exiting the AHU could be increased, since the return water temperature to the TSEV is dependent on it. But only under the condition that a higher supply air setpoint temperature does not affect the system capability of maintaining the indoor air

temperature setpoint. The limitation in this scenario would be the volume flow of air, since higher volume flow rates are required to transfer the same amount of heat at lower temperature differences.

Hence, the proposed system offers a flexible system setup to implement the two stage evaporator.

System Control:

Within the current simulation, the system control operates as intended, besides the required fine-tuning of the downshift threshold value. The system control strategy should however be adapted to the individual use-case and a thorough analysis should be carried out for the optimal control parameters.

Besides adapting the implemented control strategy, the system provides opportunities for further adaption of the operation strategy. For example, the current simulation takes only the latent phase change of water as an energy storage within the ice tank into account. However, even if the ice tank is fully discharged, the cold water within the ice tank can still be utilized to cover an AC load. Hence, the system control would need to recognize this state and adapt the operation strategy accordingly. Once the water within the ice tank would be entirely discharged and at temperatures that cannot cover AC loads (e.g. $T_{w,icetank} > 15°C$), water could be pumped from the ice tank directly to the TSEV for recharging. Thereby, the TSEV setup would cover the recharging until close to the freezing point and the LT compressor section continue until the ice tank is entirely re-charged. Hence, this requires once more an adaption of the control strategy to recognize, assess and act accordingly within those situations.

Intelligent system control by artificial intelligence controllers, which are trained on a representative data set, could facilitate such an advanced system control. However, a thorough consideration is required if the additional effort and complexity outweighs the cost savings. The implementation of intelligent system controls could potentially allow to offer possibilities for the stabilization of the electricity grid by the TES.

8.3 Experimental Work

As presented in chapter 7.3 in Table 7.3 and Figure 7.5, the load of the gravity fed evaporator $\dot{Q}_{GFE}$ deviates by $\Delta \dot{Q}_{GFE} \approx \pm 11\%$ of the mean value for the same test parameters. Since the test conditions of test 1-3 are similar, and the deviation reduces if instead of the gravity fed evaporator load the total two-stage evaporator load is regarded, the assumption lies close that the thermocouple between the two stages of the two-stage evaporator causes the inconsistencies. Especially since the evaporator loads are calculated based on the secondary fluid energy balance.

The two-stage evaporator is manufactured as a back to back plate heat exchanger with an internal secondary fluid side connection and the thermocouple being inserted within the internal secondary fluid side connection. The positioning of the thermocouple could lead to the assumption that the gravity fed evaporator inconsistencies are due to a missing entry region or insufficient mixing at the thermocouple measurement point, which could potentially lead to measuring temperature strands rather than a uniform flow temperature. Therefore, a mixing element prior to the thermocouple measurement point should be installed. The mixing element could consist of a disc that acts as a nozzle or a perforated disc, for example. Hence, the cross-section reduction leads to a higher pressure drop and higher mixing rates. Alternatively, several thermocouples could be installed, within each quadrant for example, and the mean value be taken. Thereby, a more trustworthy temperature reading is obtained. Prior to changing the experimental setup, a horizontally movable bearing of the thermocouple could help to identify if temperature strands are present. Additionally, a calibration of the thermocouple helps to ensure a correct temperature reading.

The thermocouples at the inlet and exit of the TSEV are inserted to have a minimum of 130 mm of an entrance region prior to their measurement point. Hence, their positioning makes their temperature reading more trustworthy, which is confirmed by the presented lower deviation of the total TSEV load between test 1-3 in Figure 7.5b. Consequentially, only the total two-stage evaporator load is presented within the results and discussion chapters.

The increase in two stage evaporator load, which is presented in Figure 7.6a, is congruent to the determined results within the publication by Hafner et al.[9], even though the investigated water mass flow rates by Hafner et al.[9] are lower than $\dot{m}_{w,in} \leq 24 \text{kg min}^{-1}$.

Based on Figure 7.6b, one could assume a peak in the TSEV load $\dot{Q}_{TSEV}$ at or around $EEV = 30\%$ for a water mass flow rate of $\dot{m}_{w,in} = 30 \text{kg min}^{-1}$. Behind this peak could be the following explanation: At lower EEV openings, the pressure lift increases, but the refrigerant mass flow decreases. Hence, the total transferred heat decreases. At higher openings of the EEV, the pressure lift is lower, and therefore, the driving temperature difference lower which leads to a lower transferred heat, even though the refrigerant mass flow may be higher. The assumption is supported by the ejector pressure lift, which is shown in appendix A.3, but it requires furthermore a comparison with the refrigerant flow, which was within this work not possible due to an error of the coriolis mass flow meter.

Under the assumption that the above explanation is correct could one assume that the

peak for the lower water mass flow rate is at lower *EEV* openings, which are yet to be tested.

Concluding on the experimental work is that prior to further investigations should the proposed actions be taken to ensure a correct temperature reading and to gain insights into operation characteristics between the gravity fed part and ejector fed part.

9 Conclusion

The present work investigates the application of a novel two stage evaporator (TSEV) to be used in CO_2 heat pumping systems within air conditioning applications.

The first stage of the two stage evaporator operates using the thermosyphon principle as a gravity fed evaporator. The gravity fed evaporator operates therefore in a flooded evaporator configuration, which features increased heat transfer rates and thereby higher evaporation pressures, leading to lower pressure ratios of the compressor, and hence a higher coefficient of performance. The second stage of the evaporator is driven by the suction flow of an ejector, which is used as an expansion device within the CO_2 heat pump system. The usage of the ejector allows to operate the second stage at lower pressures and thereby lower evaporation temperatures compared to the first stage. Hence, the two stage evaporator configuration is capable of providing large temperature glides of the secondary fluid and thereby increasing the system performance.

The implementation of the two stage evaporator is done using an advanced hydronic system that connects the air handling unit (AHU) with the two stage evaporator and CO_2 heat pump. It includes besides the TSEV and the AHU the implementation of cold thermal energy storages in the form of sensible and latent heat storage, by means of cold water storage tanks and an ice tank, respectively. The system setup allows to operate the system in 15 different hydronic operation modes. An adapted, rule-based control logic based on the American Society of Heating, Refrigerating and Air-Conditioning Engineers[24] is implemented to determine the optimal operation mode and whether the thermal energy storage should be charged or discharged. The two stage evaporator is implemented using a non-linear regression model based on experimentally verified simulations by Bengsch[29], and an ice tank model was created.

The performance of the system is investigated for an exemplary AC load curve of up to $\dot{Q}_{AC,load} = 60.1\,\text{kW}$ using exemplary component sizes. The system achieves that the production of 65 % of the required on-peak AC demand is shifted to off-peak periods. Furthermore, the load on the CO_2 heat pump system is kept constant at $\dot{Q}_{TSEV} = 20\,\text{kW}$. Hence, the system in its current configuration can achieve the aim of the implementation of the TES to shift on-peak loads towards the off-peak period and reduce the peak load onto the CO_2 heat pump system. Hence, the proposed system achieves good preliminary results, which require further investigations due to the assumptions and simplifications made within the work. Therefore, the result from the simulational work should be regarded as a proof of concept.

Besides the simulational work, initial experiments of the TSEV were conducted. The initial results show inconsistencies due to presumably a thermocouple placement, which requires further investigation with the proposed measures.

10 Further Work

The following chapter presents firstly the proposed actions within the simulational part of the work in chapter 10.1, followed by the proposed measures regarding the two-stage evaporator test rig in chapter 10.2.

10.1 Simulational Work

Since the simulational work, that has been carried out, only serves as a proof of concept rather than a final simulation, a "real-life" application should be found and the assumptions within the system be adapted onto the application. Furthermore, the following remarks should be investigated:

The geometry and heat transfer within the air handling unit requires further investigation, since the air handling unit has a major effect on the water return temperatures and required water mass flow rates. Furthermore, the implementation of suitable heat transfer correlations based on the fluid flows within the air handling unit is evidently important. Besides the improvement within the air handling unit, a closer investigation on the cause of the energy imbalance on the water side of the ice tank is required, since more energy is discharged within the water stream than is discharged by the phase change of ice to water.

Arguably the largest effect on the simulation would have the implementation of the two-stage evaporator setup as a dynamic CO_2 heat pump model within the simulation environment. The current non-linear regression model of the CO_2 heat pump provides indications of the MT compressor work, since the gas cooler pressure is fixed at $p_{GC} = 120\,\text{bar}$ and therefore, a dynamic model would allow more accurate predictions depending on the heat sink conditions. Additionally, the system response changes due to the inertia of the system by a dynamic model. An economical evaluation would be furthermore required to determine whether the additional expenditures can be covered by the systems energy efficiency improvements.

10.2 Experimental Work

An extensive test series should be carried out to ensure the repeatability of the experiments as well as characterising the system performance under different test conditions. Obtaining experimental results does not only allow to assess the system performance, but also to provide a basis to implement precise two stage evaporator characteristics within numerical simulations.

However, prior to the test series should a verification of the accuracy of the thermocouple on the secondary fluid between the evaporator stages side be carried out. Such a verification allows trustworthy conclusions on the individual performance of the evaporators.

References

[1] H.-O. Pörtner, D.C. Roberts, E.S. Poloczanska, K. Mintenbeck, M. Tignor, A. Alegría, M. Craig, S. Langsdorf, S. Löschke, V. Möller, and A. Okem (eds.). Summary for policymakers, 2022. URL `https://www.ipcc.ch/report/ar6/wg2/downloads/report/IPCC_AR6_WGII_SummaryForPolicymakers.pdf`. Accessed: 2022-10-10.

[2] Yabin Dong, Marney Coleman, and Shelie A. Miller. Greenhouse Gas Emissions from Air Conditioning and Refrigeration Service Expansion in Developing Countries. *Annu. Rev. Environ. Resour.*, 46(1):59–83, October 2021. ISSN 1543-5938, 1545-2050. doi: 10.1146/annurev-environ-012220-034103. URL `https://www.annualreviews.org/doi/10.1146/annurev-environ-012220-034103`.

[3] M. Eckert, M. Kauffeld, and V. Siegismund. *Natural Refrigerants: Applications and Practical Guidelines*. VDE Verlag GmbH, 2022. ISBN 9783800753314. URL `https://www.vde-verlag.de/books/495330/natural-refrigerants-applications-and-practical-guidelines.html`.

[4] Brian T. Austin and K. Sumathy. Transcritical carbon dioxide heat pump systems: A review. 15(8):4013–4029, October 2011. ISSN 13640321. doi: 10.1016/j.rser.2011.07.021. URL `https://linkinghub.elsevier.com/retrieve/pii/S1364032111002607`.

[5] Yulong Song, Ce Cui, Xiang Yin, and Feng Cao. Advanced development and application of transcritical CO2 refrigeration and heat pump technology—a review. 8:7840–7869, November 2022. ISSN 23524847. doi: 10.1016/j.egyr.2022.05.233. URL `https://linkinghub.elsevier.com/retrieve/pii/S2352484722010794`.

[6] Anas F.A. Elbarghthi, Armin Hafner, Krzysztof Banasiak, and Vaclav Dvorak. An experimental study of an ejector-boosted transcritical r744 refrigeration system including an exergy analysis. 238:114102, June 2021. ISSN 01968904. doi: 10.1016/j.enconman.2021.114102. URL `https://linkinghub.elsevier.com/retrieve/pii/S0196890421002788`.

[7] Dazhang Yang, Yang Li, Jing Xie, and Jinfeng Wang. Exergy destruction characteristics of a transcritical carbon dioxide two-stage compression/ejector refrigeration system for low-temperature cold storage. 8:8546–8562, November 2022. ISSN 23524847. doi: 10.1016/j.egyr.2022.06.066. URL `https://linkinghub.elsevier.com/retrieve/pii/S2352484722012069`.

[8] Stefan Elbel. Historical and present developments of ejector refrigeration systems with emphasis on transcritical carbon dioxide air-conditioning applications. 34(7):

1545–1561, November 2011. ISSN 01407007. doi: 10.1016/j.ijrefrig.2010.11.011. URL `https://linkinghub.elsevier.com/retrieve/pii/S0140700710002720`.

[9] HAFNER A, HAZARIKA M. M, LECHI F, ZORZIN A, PARDIÑAS A. A, and BANASIAK K. Experimental investigation on integrated two-stage evaporators for CO2 heat-pump chillers., June 2022. URL `https://iifiir.org/datacite_notices/145436`. Type: dataset.

[10] HAZARIKA M. M, BENGSCH J, HAFSAS J, HAFNER A, SVENDSEN E. S, and YE Z. Integration of gravity-fed evaporators in CO2 based heat-pump chillers., June 2022. URL `https://iifiir.org/datacite_notices/145337`. Type: dataset.

[11] Emanuele Zanetti, Marco Azzolin, Riccardo Conte, Sergio Girotto, and Davide Del Col. Experiments and dynamic modelling of dry expansion and flooded evaporators in a CO2 solar assisted heat pump. 217:118964, November 2022. ISSN 13594311. doi: 10.1016/j.applthermaleng.2022.118964. URL `https://linkinghub.elsevier.com/retrieve/pii/S1359431122009024`.

[12] Lixin Cheng, Gherhardt Ribatski, and John R. Thome. New prediction methods for CO2 evaporation inside tubes: Part II—an updated general flow boiling heat transfer model based on flow patterns. 51(1):125–135, January 2008. ISSN 00179310. doi: 10.1016/j.ijheatmasstransfer.2007.04.001. URL `https://linkinghub.elsevier.com/retrieve/pii/S0017931007002840`.

[13] Giacomo Tosato, Sergio Girotto, Silvia Minetto, Antonio Rossetti, and Sergio Marinetti. An integrated CO $_2$ unit for heating, cooling and DHW installed in a hotel. data from the field. 1599(1):012058, August 2020. ISSN 1742-6588, 1742-6596. doi: 10.1088/1742-6596/1599/1/012058. URL `https://iopscience.iop.org/article/10.1088/1742-6596/1599/1/012058`.

[14] Guruprasad Alva, Yaxue Lin, and Guiyin Fang. An overview of thermal energy storage systems. *Energy*, 144:341–378, February 2018. ISSN 03605442. doi: 10.1016/j.energy.2017.12.037. URL `https://linkinghub.elsevier.com/retrieve/pii/S036054421732056X`.

[15] Sepehr Sanaye and Mohammad Hekmatian. Ice thermal energy storage (ITES) for air-conditioning application in full and partial load operating modes. *International Journal of Refrigeration*, 66:181–197, June 2016. ISSN 01407007. doi: 10.1016/j.ijrefrig.2015.10.014. URL `https://linkinghub.elsevier.com/retrieve/pii/S0140700715003096`.

[16] A. Hafner, S. Silje, and Y. Allouche. Demonstration of the next generation standardised integrated cooling and heating packages for commercial and pub-

lic buildings based on environment-friendly carbon dioxide vapour compression cycles, 2021. URL `https://www.ntnu.edu/documents/1272037961/0/723137_Deliverable_16_%28Educational+e-book+about+MULTIPACK+No+2%29.pdf/b544d606-c41e-390f-5be6-c82512af7318?t=1616766385953`. Accessed: 2022-12-07.

[17] Rami Zeinelabdein, Siddig Omer, and Guohui Gan. Experimental performance of latent thermal energy storage for sustainable cooling of buildings in hot-arid regions. *Energy and Buildings*, 186:169–185, March 2019. ISSN 03787788. doi: 10.1016/j.enbuild.2019.01.013. URL `https://linkinghub.elsevier.com/retrieve/pii/S0378778818319042`.

[18] M.A. Said and Hamdy Hassan. An experimental work on the effect of using new technique of thermal energy storage of phase change material on the performance of air conditioning unit. *Energy and Buildings*, 173:353–364, August 2018. ISSN 03787788. doi: 10.1016/j.enbuild.2018.05.041. URL `https://linkinghub.elsevier.com/retrieve/pii/S0378778818310326`.

[19] Chengchu Yan, Wenxing Shi, Xianting Li, and Yang Zhao. Optimal design and application of a compound cold storage system combining seasonal ice storage and chilled water storage. *Applied Energy*, 171:1–11, June 2016. ISSN 03062619. doi: 10.1016/j.apenergy.2016.03.005. URL `https://linkinghub.elsevier.com/retrieve/pii/S0306261916303166`.

[20] Mohamed Elhelw and Wael M. El-Maghlany. Thermodynamic analysis of two air conditioning systems with ice thermal storage in Egypt. *J Therm Anal Calorim*, 140(5): 2563–2573, June 2020. ISSN 1388-6150, 1588-2926. doi: 10.1007/s10973-019-08999-8. URL `http://link.springer.com/10.1007/s10973-019-08999-8`.

[21] Håkon Selvnes, Ángel A Pardiñas, and Armin Hafner. Cold thermal energy storage for air conditioning in a supermarket CO2 booster refrigeration system. 2023. doi: 10.18462/iir.nh3-co2.2023.0021.

[22] Zhun (Jerry) Yu, Gongsheng Huang, Fariborz Haghighat, Hongqiang Li, and Guoqiang Zhang. Control strategies for integration of thermal energy storage into buildings: State-of-the-art review. *Energy and Buildings*, 106:203–215, November 2015. ISSN 03787788. doi: 10.1016/j.enbuild.2015.05.038. URL `https://linkinghub.elsevier.com/retrieve/pii/S0378778815300116`.

[23] Silje Smitt, Ignat Tolstorebrov, and Armin Hafner. Integrated CO2 system with HVAC and hot water for hotels: Field measurements and performance evaluation. 116:56–59, 2020. ISSN 0140-7007. URL `https://doi.org/10.1016/j.ijrefrig.2020.03.021`.

[24] American Society of Heating, Refrigeration and Air-Conditioning Engineers. *2015 ASHRAE handbook: heating, ventilating, and air-conditioning applications, Inch - Pound Edition*. ASHRAE 2015, i-p edition edition, 2015. ISBN 978-1-68015-792-5. OCLC: 921242601.

[25] Kirk Drees and James Braun. Development and Evaluation of a Rule-Based Control Strategy for Ice Storage Systems. *HVAC&R Res.*, 2(4):312–334, October 1996. ISSN 1078-9669. doi: 10.1080/10789669.1996.10391352. URL `http://www.tandfonline.com/doi/abs/10.1080/10789669.1996.10391352`.

[26] Dassault Systems. What is dymola?, 2019. URL `https://www.3ds.com/fileadmin/PRODUCTS/CATIA/DYMOLA/PDF/What-is-Dymola-2020x.pdf`. Accessed: 2023-05-13.

[27] TLK Thermo GmbH. Til suite - simulates thermal systems. URL `https://www.tlk-thermo.com/index.php/en/til-suite`. Accessed: 2023-05-13.

[28] Frank P Incropera, David P DeWitt, Theodore L Bergman, Adrienne S Lavine, et al. *Fundamentals of heat and mass transfer*, volume 6. Wiley New York, 1996.

[29] J. Bengsch. Investigation and analysis of a co2 heat pump chiller with novel two-stage evaporator. 2022. URL `https://ntnuopen.ntnu.no/ntnu-xmlui/handle/11250/3030759`.

[30] A. Hafner and T. M. Eikevik. *TEP 4255 Compendium*. NTNU, 2023.

[31] S.A. Klein. EES-Engineering Equation Solver. URL `https://fchartsoftware.com`. Accessed: 2023-06-05.

[32] Danfoss. Thermoclean®, 2018. URL `https://assets.danfoss.com/documents/73483/AI135086459010en-010601.pdf`. Accessed: 2023-05-21.

[33] A.S. Pamitran, Kwang-Il Choi, Jong-Taek Oh, and Nasruddin. Evaporation heat transfer coefficient in single circular small tubes for flow natural refrigerants of C3H8, NH3, and CO2. *International Journal of Multiphase Flow*, 37(7):794–801, September 2011. ISSN 03019322. doi: 10.1016/j.ijmultiphaseflow.2011.02.005. URL `https://linkinghub.elsevier.com/retrieve/pii/S0301932211000504`.

[34] Technical Committee ISO/TC 159 and Technical Committee CEN/TC 122. Ergonomics of the thermal environment – analytical determination and interpretation of thermal comfort using calculation of the pmv and ppd indices and local thermal comfort criteria. Standard NS-EN ISO 7730:2005, European Committee for standardization, Brussels, BE, 2006. URL `https://www.standard.no/no/Nettbutikk/produktkatalogen/Produktpresentasjon/?ProductID=123455`.

[35] X.Y. Sun, Y.J. Dai, T.S. Ge, Y. Zhao, and R.Z. Wang. Heat and mass trans-

fer comparisons of desiccant coated microchannel and fin-and-tube heat exchangers. *Applied Thermal Engineering*, 150:1159–1167, March 2019. ISSN 13594311. doi: 10.1016/j.applthermaleng.2019.01.071. URL `https://linkinghub.elsevier.com/retrieve/pii/S1359431118361258`.

A Apppendix

A.1 Process and Instrumentation Diagram of the Multifunctional CO_2 Test Rig
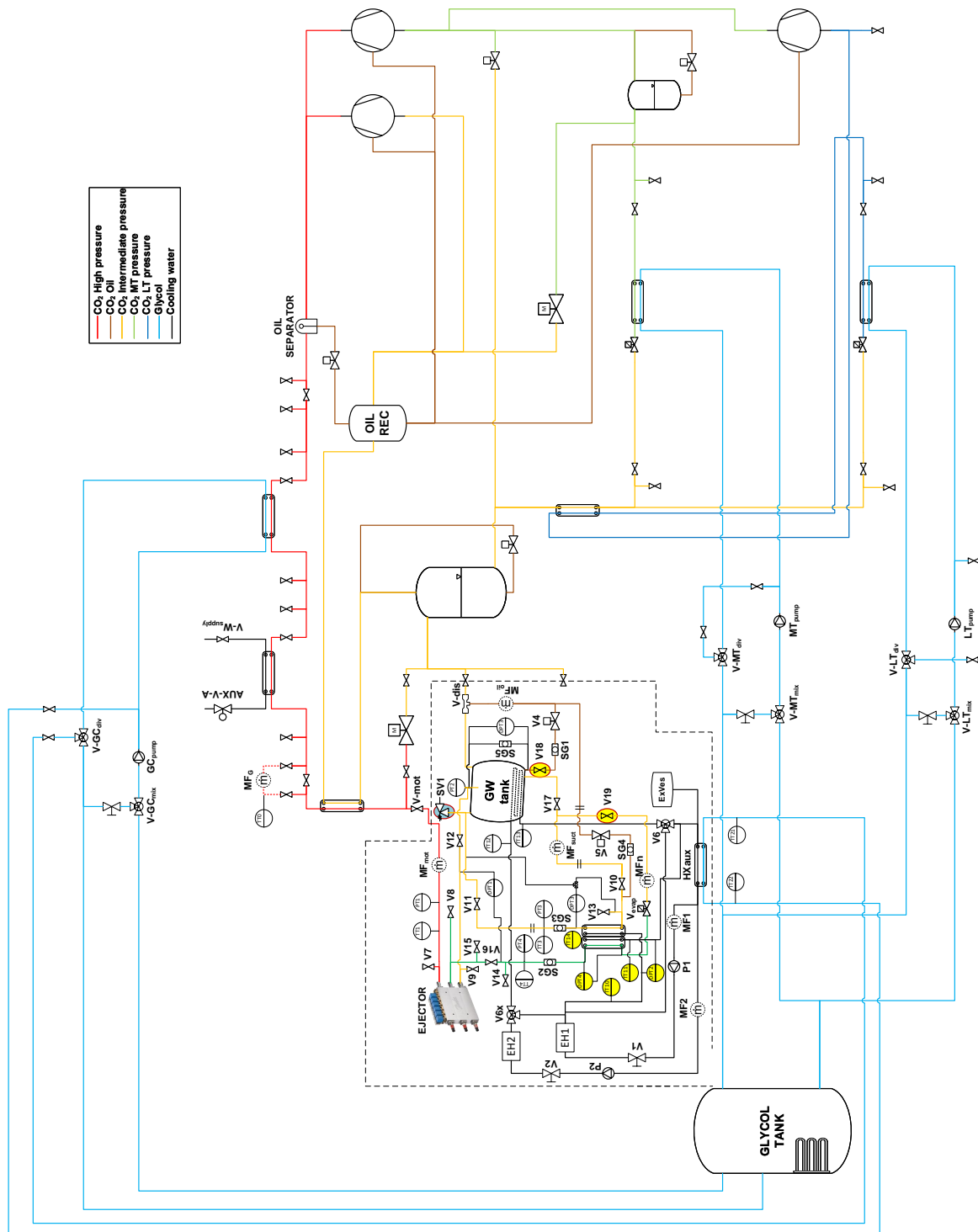
Figure A.1: Process Diagram Multifunctional CO_2 Test Rig

A.2 Modelica Code of Ice Tank Model

```
block CTES_Model_v15
"Ice Tank Model with water in and out flow, as well as refrigerant,
    ↪ discretized into n-layers, upward flow refrigerant"

parameter Integer nCells=1 "Number of vertical Cells";
parameter Real d_pipe=0.02 "Outer pipe diameter of tubes [m]";
parameter Real n_tubes=2 "Number of tubes";
parameter Real T_init_w = 273+5 "Initial Water Temperature";
parameter Real delta_tube=0.002 "Thickness tube";
parameter Real D_tank=1 "horizontal depth of tank";
parameter Real W_tank=1 "horizontal width of tank";
parameter Real H_tank=1 "vertical height of tank";
parameter Real delta_ice_init = 0.0;


public
Modelica.Blocks.Interfaces.RealOutput h_R_out "Enthalpy Refrigerant
    ↪ out"
annotation (Placement(transformation(extent={{96,50},{116,70}})));

Modelica.Blocks.Interfaces.RealOutput T_w_out "Temperature water out
    ↪ "
annotation (Placement(transformation(extent={{96,-10},{116,10}})));

Modelica.Blocks.Interfaces.RealInput m_flow_r "Mass flow refrigerant
    ↪ "
annotation (Placement(transformation(
extent={{-20,-20},{20,20}},
rotation=270,
origin={0,110})));


parameter Real k_ice=0.65 "Thermal Conductivity Ice {W/m-K}"
    ↪ annotation (Dialog(tab="Advanced"));
parameter Real htc_R=10 "HTC R-pipe [W/m^2-K]"annotation (Dialog(tab
    ↪ ="Advanced"));
parameter Real htc_W=10 "HTC water-ice [W/m^2-K]"annotation (Dialog(
    ↪ tab="Advanced"));
parameter Real dh_fus=333.55e3  "J/kg"annotation (Dialog(tab="
    ↪ Advanced"));
parameter Real rho_ice=916 "kg/m^3"annotation (Dialog(tab="Advanced"
    ↪ ));
parameter Real H_cell = H_tank/nCells "cell height" annotation (
    ↪ Dialog(tab="Advanced"));
parameter Real T_0[nCells] = {273.15 for i in 1:nCells} "K"
    ↪ annotation (Dialog(tab="Advanced"));
```

```
Real r_1(start = d_pipe/2);
Real h_w_cell_N[nCells](start = {sub_w.h_Txi(T_init_w,zeros(0)) for
    ↪ i in 1:nCells});
Real delta[nCells];
Real m_flow_w_cell[nCells];
Real Q_st[nCells](start = {(dh_fus*rho_ice*Modelica.Constants.pi*
    ↪ H_cell*((r_1+delta[i])^2 - (r_1)^2)) for i in 1:nCells});
Real T_w_cell[nCells](start = {T_init_w for i in 1:nCells});
Real m_w_cell[nCells](start = {((H_cell*D_tank*W_tank - n_tubes*
    ↪ Modelica.Constants.pi*((r_1+delta[i])^2)*H_cell)*sub_w.d_Txi(
    ↪ T_w_cell[i],zeros(0))) for i in 1:nCells});
Real h_w_cell[nCells](start = {sub_w.h_Txi(T_w_cell[i],zeros(0)) for
    ↪  i in 1:nCells}) " initialized further down ";
Real T_R_in[nCells](start = {vleFluid.T_phxi(p_R_in,h_R_in,zeros(0))
    ↪  for i in 1:nCells}) " intiliazed further down";
Real h_R_cell[nCells];
Real HT_ice_cmp[nCells];
Real HT_w_cmp[nCells];
Real m_flow_r_cell[nCells];
Real h_R_cell_S[nCells];

/* Real E_int[nCells]; */

Real m_R_cell[nCells];
Real T_R[nCells];
Real HT_ice[nCells];
Real HT_w[nCells];
Real h_iwc "Enthalpy initial water cell";
Real SOC_IT "State of charge of ice tank";
Real delta_max "max ice layer";
Integer State[nCells](start = {0 for i in 1:nCells});
Integer State_HT[nCells](start = {0 for i in 1:nCells});
Real SOC_cell[nCells];

Modelica.Blocks.Interfaces.RealInput m_flow_w
"Mass flow of water into the CTES" annotation (Placement(
    ↪ transformation(
extent={{-20,-20},{20,20}},
rotation=90,
origin={-40,-108})));
Modelica.Blocks.Interfaces.RealInput T_w_in "Inlet water temperature
    ↪ "
annotation (Placement(transformation(
extent={{-20,-20},{20,20}},
rotation=90,
origin={40,-108})));
```

112

```
    Modelica.Blocks.Interfaces.RealInput h_R_in "Enthalpy Refrigerant in
        ↪ "
    annotation (Placement(transformation(
    extent={{-20,-20},{20,20}},
    rotation=270,
    origin={60,110})));
    Modelica.Blocks.Interfaces.RealInput p_R_in "Temperature Refrigerant
        ↪  in "
    annotation (Placement(transformation(
    extent={{-20,-20},{20,20}},
    rotation=270,
    origin={-60,110})));
    TILMedia.Liquid sub_w(redeclare TILMedia.LiquidTypes.TILMedia_Water
    liquidType)
    annotation (Placement(transformation(extent={{20,-62},{40,-42}})));

    Modelica.Blocks.Interfaces.RealOutput der_m_w_out "Temperature water
        ↪  out"
    annotation (Placement(transformation(extent={{96,-70},{116,-50}})));

    TILMedia.VLEFluid vleFluid(redeclare TILMedia.VLEFluidTypes.
        ↪ TILMedia_CO2
    vleFluidType)
    annotation (Placement(transformation(extent={{-60,40},{-40,60}})));
    Modelica.Blocks.Interfaces.RealOutput SOC_IT_out "Temperature water
        ↪ out"
    annotation (Placement(transformation(extent={{-96,-10},{-116,10}})))
        ↪ ;
    Modelica.Blocks.Interfaces.RealOutput E_int_w "Temperature water out
        ↪ "
    annotation (Placement(transformation(extent={{-96,-50},{-116,-30}}))
        ↪ );
    initial equation
    delta = {delta_ice_init for i in 1:nCells};
    /* E_int = {(m_w_cell[i]*sub_w.h_Txi(T_w_cell[i],zeros(0))) for i in
        ↪  1:nCells}; */
    h_w_cell = {(sub_w.h_Txi(T_w_cell[i],zeros(0))) for i in 1:nCells};

    if (n_tubes*Modelica.Constants.pi*(r_1+delta_ice_init) ^2 >= D_tank*
        ↪ W_tank) then
    terminate("Intial ice coverage larger than cross sectional surface")
        ↪ ;
    end if;

    h_R_cell = {h_R_in for i in 1:nCells};

    /* m_flow_w_cell = {m_flow_w for i in 1:nCells};*/
```

```
equation
/* Cell independent equations */
h_iwc = sub_w.h_Txi(T_w_in,zeros(0)) "Enthalpy of initial water cell
    ↪ ";
r_1 = d_pipe/2;
for i in 1:nCells loop
/* ---------------- Water cell calculations
    ↪ ----------------------------*/
/* h_w_cell[i] = E_int[i]/m_w_cell[i];*/
T_w_cell[i] = sub_w.T_hxi(h_w_cell[i],zeros(0));

/* Communication in water cells */
if i ==1 then
h_w_cell_N[i] = h_iwc;
m_flow_w_cell[i] = m_flow_w;
else
h_w_cell_N[i] = h_w_cell[i-1];
m_flow_w_cell[i] = m_flow_w_cell[i-1] + ((sub_w.d_Txi(T_w_cell[i],
    ↪ zeros(0)) - rho_ice)*(der(Q_st[i])/(dh_fus*rho_ice)));
end if;

/* Mass water cell */
m_w_cell[i] = ((H_cell*D_tank*W_tank - n_tubes*Modelica.Constants.pi
    ↪ *((r_1+delta[i])^2)*H_cell)*sub_w.d_Txi(T_w_cell[i],zeros(0)))
    ↪ ;
/* m_flow_w_cell[i] = ((sub_w.d_Txi(T_w_cell[i],zeros(0)) - rho_ice)
    ↪ *(der(Q_st[i])/(dh_fus*rho_ice))); */

/* Energy balance of water cell */
der(h_w_cell[i])*m_w_cell[i] = -HT_w[i] + m_flow_w_cell[i]*(
    ↪ h_w_cell_N[i] - h_w_cell[i]);

/* ---------------Ice cell calculations:
    ↪ ------------------------------*/
Q_st[i] = noEvent((dh_fus*rho_ice*Modelica.Constants.pi*H_cell*((r_1
    ↪ +delta[i])^2 - (r_1)^2))*n_tubes);
/* Ice Surface Energy Balance */
if (HT_ice[i] > HT_w[i]) then
/* Ice formation occurs, ice layer growing */
der(Q_st[i]) = (HT_ice[i] - HT_w[i]);
State[i] = 4;
elseif (HT_ice[i] <= HT_w[i] and delta[i] > 0) then
/* Ice layer larger 0, ice is melting */
der(Q_st[i]) = (HT_ice[i] - HT_w[i]);
State[i] = 2;
else
der(Q_st[i]) = 0;
```

```
    State[i] = 3;
    end if;

    /* ------------------Refrigerant Calculation
        ↪ --------------------------- */
    T_R_in[i] = vleFluid.T_phxi(p_R_in,h_R_cell[i],zeros(0));
    /* Handling of the refrigerant mass flow dependent calculation" */
    T_R[i] = noEvent(if m_flow_r > 0 then T_R_in[i] else T_0[i]);
    der(h_R_cell[i])*m_R_cell[i] = HT_ice[i] + m_flow_r_cell[i]*(
        ↪ h_R_cell_S[i]-h_R_cell[i]);
    m_R_cell[i] = (n_tubes*H_cell*Modelica.Constants.pi*(r_1-delta_tube)
        ↪ ^2)*vleFluid.d_phxi(p_R_in,h_R_cell[i],  zeros(0));

    /* m_flow_r_cell[i] = der(m_R_cell[i]);*/

    if i == nCells then
    h_R_cell_S[i] = h_R_in;
    m_flow_r_cell[i] = m_flow_r;
    else
    h_R_cell_S[i] = h_R_cell[i+1];
    m_flow_r_cell[i] = m_flow_r_cell[i+1] - der(m_R_cell[i+1]);
    end if;

    /* -----------------Heat Transfer calculation
        ↪ ---------------------------*/
    HT_ice_cmp[i] = ((T_0[i]-T_R[i])/( (1/(2*Modelica.Constants.pi*r_1*
        ↪ H_cell*htc_R)) + ( log((r_1+delta[i])/r_1)/(2*Modelica.
        ↪ Constants.pi*k_ice*H_cell))))*n_tubes;
    HT_w_cmp[i] = htc_W*2*Modelica.Constants.pi*(r_1+delta[i])*H_cell*(
        ↪ T_w_cell[i] - T_0[i])*n_tubes;

    /* Heat transfer ice ..................... */
    if (n_tubes*Modelica.Constants.pi*(r_1+delta[i])  ^2 >= D_tank*
        ↪ W_tank*0.999) then
    /* Checks if the tank is full, if yes, no change in enthalpy made */
    HT_ice[i] = 0;
    State_HT[i]=10;
    elseif HT_ice_cmp[i] > 0 then
    HT_ice[i] = HT_ice_cmp[i];
    State_HT[i] = 1;
    elseif delta[i] <= 0 and HT_ice_cmp[i] <= HT_w_cmp[i] and m_flow_r
        ↪ >0 then
    HT_ice[i] = ((T_w_cell[i]-T_R[i])/( (1/(2*Modelica.Constants.pi*r_1*
        ↪ H_cell*htc_R)) + ( log((r_1+delta[i])/r_1)/(2*Modelica.
        ↪ Constants.pi*k_ice*H_cell)) + 1/(2*Modelica.Constants.pi*(r_1+
        ↪ delta[i])*H_cell*htc_W)))*n_tubes + m_flow_r_cell[i] *(
        ↪ h_R_cell_S[i] - h_R_cell[i]);
```

```
State_HT[i] = 2;
else
HT_ice[i] = 0;
State_HT[i] = 3;
end if;

/* Heat transfer water:.....................  */
if HT_w_cmp[i] >0 and delta[i] > 0 then
/* Heat transfer with ice layer there */
HT_w[i] = HT_w_cmp[i];
elseif delta[i] <= 0 and HT_ice_cmp[i] <= HT_w_cmp[i] and m_flow_r
    ↪ >0 then
/* Heat transfer with no ice layer there , but refrigerant flow */
HT_w[i] = ((T_w_cell[i]-T_R[i])/( (1/(2*Modelica.Constants.pi*r_1*
    ↪ H_cell*htc_R)) + ( log((r_1+delta[i])/r_1)/(2*Modelica.
    ↪ Constants.pi*k_ice*H_cell)) + 1/(2*Modelica.Constants.pi*(r_1+
    ↪ delta[i])*H_cell*htc_W)))*n_tubes + m_flow_w_cell[i] *(
    ↪ h_w_cell_N[i] - h_w_cell[i]);
else
HT_w[i] = 0;
end if;


SOC_cell[i] = (n_tubes*Modelica.Constants.pi*(delta[i]+r_1)^2   -(
    ↪ n_tubes*Modelica.Constants.pi*(r_1)^2))/(W_tank*D_tank -(
    ↪ n_tubes*Modelica.Constants.pi*(r_1)^2));
end for;
/* Output of calculated properties */
h_R_out = h_R_cell[1];
if m_flow_w > 0 then
T_w_out = T_w_cell[nCells];
else
T_w_out = T_w_cell[1];
end if;
der_m_w_out = -(m_flow_w - m_flow_w_cell[nCells]);
SOC_IT = sum(SOC_cell)/nCells
"(sum(delta[1:nCells]))/(delta_max*nCells)   sum(Q_st)/((dh_fus*
    ↪ rho_ice*H_tank*(D_tank*W_tank - n_tubes*Modelica.Constants.pi
    ↪ *(r_1)^2)))";
delta_max = sqrt(D_tank*W_tank/(n_tubes*Modelica.Constants.pi))-r_1;

E_int_w = sum(m_w_cell*h_w_cell);
SOC_IT_out = SOC_IT;
annotation (Line(points={{42,110},{42,110}}, color={0,0,127}),
Documentation(info="This block represents an ice tank."),
Icon(coordinateSystem(preserveAspectRatio=true, extent
    ↪ ={{-100,-100},{100,
```

```
        100}}), graphics={
    Polygon(
    points
        ↪ ={{-100,-100},{-100,100},{100,100},{100,-100},{-100,-100}},
        ↪
    lineColor={0,0,127},
    fillColor={255,255,255},
    fillPattern=FillPattern.Solid),
    Text(
    extent={{-150,20},{150,-20}},
    textString="CTES",
    textColor={0,0,255})})));
  end CTES_Model_v15;
```

A.3   Ejector Pressure Lift

Table A.1 shows the pressure lift of the ejector for the test conditions of $\dot{m}_w = 24 \,\&\, 30\,\mathrm{kg\,min^{-1}}$, $T_{w,in} = 15\,°\mathrm{C}$, $p_{rec} = 44\,\mathrm{bar}$ and $EEV = 20,\ 30,\ 40\%$.

Table A.1: Ejector Pressure Lift for $\dot{m}_w = 24 \,\&\, 30\,\mathrm{kg\,min^{-1}}$, $T_{w,in} = 15\,°\mathrm{C}$, $p_{rec} = 44\,\mathrm{bar}$ and $EEV = 20,\ 30,\ 40\,\%$

EEV [%]	Δp_{lift} for $\dot{m}_w = 24\,\mathrm{kg\,s^{-1}}$ [bar]	Δp_{lift} for $\dot{m}_w = 30\,\mathrm{kg\,s^{-1}}$ [bar]
20	4.19	5.17
30	4.08	5.01
40	3.95	4.69

A.4   Draft Scientific Article

The following draft scientific article is written in a conference paper style and presents the main findings from the simulational work.

APPLICATION OF A NOVEL TWO STAGE EVAPORATOR WITHIN AIR CONDITIONING APPLICATIONS

Lukas Köster[(a)]

[(a)] Norwegian University of Science and Technology, 7020 Trondheim, Norway
lukaskos@stud.ntnu.no

ABSTRACT

The present study investigates the application of a novel two stage evaporator into air conditioning (AC) applications. The proposed system includes latent and sensible thermal energy storage by means of an ice tank and cold-water storage tank. A rule-based optimal control strategy is implemented, which determines whether the thermal energy storage should be charged or discharged. The model is built within the Dymola environment using Modelica as the programming language. Dynamic simulations are carried out for a 24-h period for an exemplary air conditioning demand and exemplary component sizes. The implementation of the thermal energy storage covers 65 % of the on-peak air conditioning demand. Hence, 65 % of the energy required to cover the AC demand can be produced during the off-peak period. Furthermore, the implementation of the thermal energy storage achieves load shifting and peak load limiting and provides due to the system setup great operational flexibility.

1. INTRODUCTION

Global warming is an undisputable fact, and the consequences are not entirely foreseeable. It is already known that by not reaching the 1.5 °C climate goal, a significant increase in climate hazards and risks onto ecosystems emerges (Pörtner et al., 2022). The refrigeration and space cooling sector accounts for 10 % of the total greenhouse gas emissions (GHG) emissions (Dong et al., 2021) and is therefore regarded as an important contributor. The GHG-emissions differentiate between GHG emissions due to refrigerant leakage and emissions related to the energy consumption. According to Dong et al. (2021), GHG-emissions from space cooling are more than double compared to the GHG emissions from refrigeration. Within the GHG emissions related to space cooling, GHG emissions due to energy consumption account for 69.3 % and 30.7 % due to refrigerant leakage (Dong et al., 2021). Hence, an increase in energy efficiency of space cooling systems and a replacement of refrigerants with high global warming potential by natural refrigerants shows great potential to reduce GHG emissions.

CO_2 is a natural refrigerant with unique thermophysical properties and a low global warming potential (GWP $=1$) and has therefore gained attention within recent years in covering the heating and cooling demand of buildings. Implementing thermal energy storage into heat pump systems offers the ability to utilize load-shifting, load levelling and load limiting strategies and potentially make use of dynamic electricity prices.

Therefore, this work investigates an advanced CO_2 heat pump system, which covers an exemplary air conditioning demand by utilizing cold thermal energy storage by means of an ice tank and cold water storage tanks.

2. SYSTEM DESCRIPTION

The system consists of a CO_2 heat pump system with a two-stage evaporator setup, and the hydronic AC system configuration connected to the two stage evaporator, as Figure 1 shows. The first stage of the two-stage evaporator makes use of the thermosyphon principle, where refrigerant is circulated due to density differences as a result from the evaporation. The direct connection between the liquid receiver and the evaporator leads to a flooded operation of the two-stage evaporator and thereby enhancing heat transfer coefficients and increasing the receiver pressure level, hence decreasing the compressor work. The second stage of the two-stage evaporator is driven by the suction port of the ejector and operates at lower pressures (and lower temperatures) than the first evaporator stage. An additional low temperature stage is implemented in the system to charge the ice tank.

The hydronic sub-system consists of four main components, the two-stage evaporator, the cold water storage tanks (CST), the ice tanks and the air handling unit. It can be additionally extended by heat sources, such as a

borehole or an ambient heat exchanger, if the heat source has a suitable temperature range for the utilization with water as a working fluid.
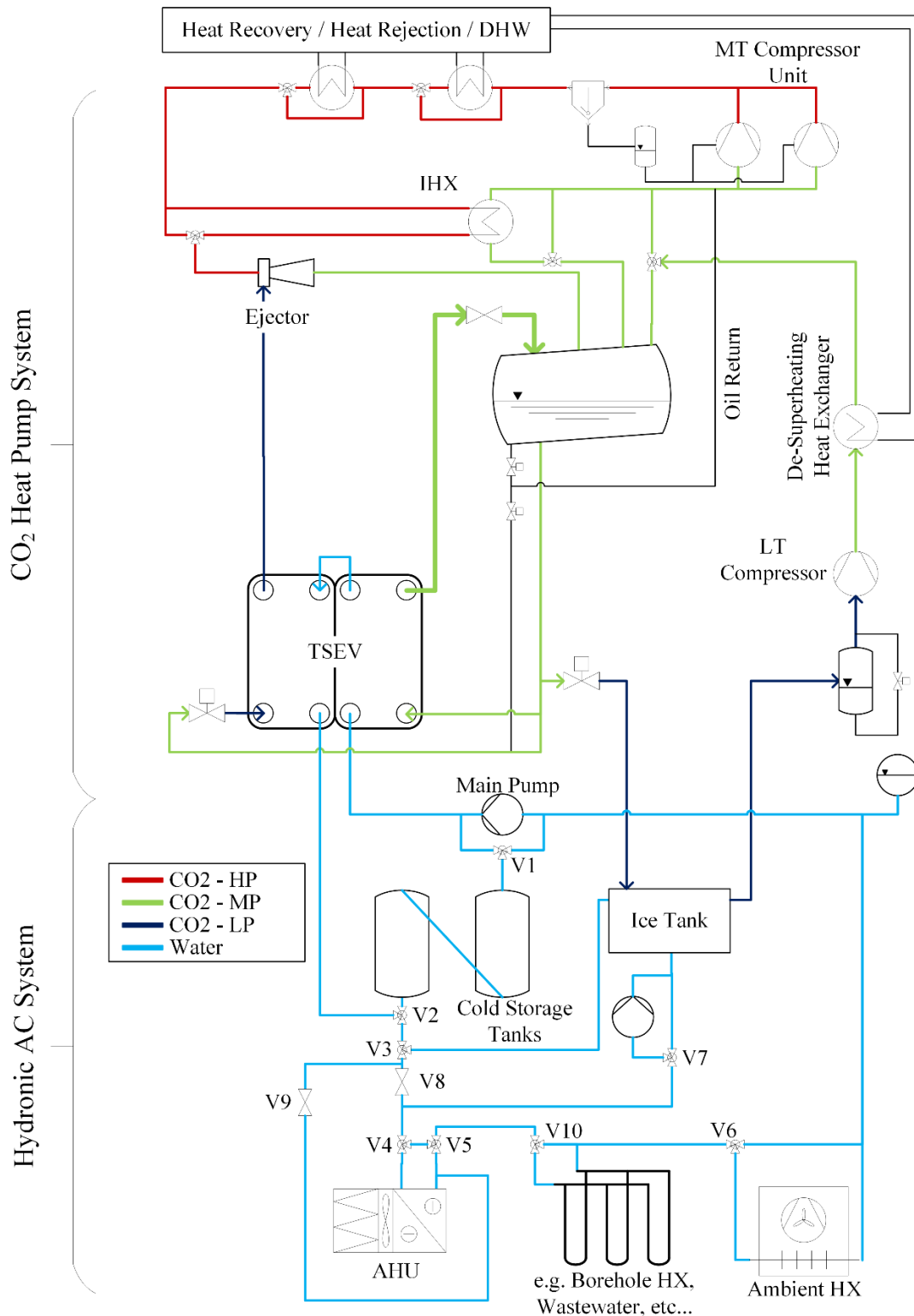
Figure 1: Schematic Drawing of the CO2 Heat Pump and Hydronic Subsystem

The hydronic system components are arranged such that the system can operate with a high degree of flexibility regarding the heat pump and thermal energy storage utilization. Therefore, Table 1 presents possible operation modes of the system classified after the cold storage tank operation mode. The operation of the ambient heat exchanger and additional heat sources is disregarded within the present study.

Table 1: Operation Modes of the Hydronic Sub-System ordered after the Cold Water Storage Tank (CST) Operation

	Operation Mode	Two Stage Evaporator	Cold Water Storage Tank	Main Pump	Ice Tank Pump	Air Handling Unit	Operation of Ambient HX possible
CST charging + AHU off	1	ON	ON	ON	OFF	OFF	(Yes)
	2	OFF	ON	OFF	ON	OFF	No
	3	ON	ON	ON	ON	OFF	No
CST Charging + AHU on	4	ON	ON	ON	OFF	ON	Yes
	5	OFF	ON	OFF	ON	ON	No
	6	ON	ON	ON	ON	ON	Yes
CST neutral + AHU on	7	ON	OFF	ON	OFF	ON	Yes
	8	OFF	OFF	OFF	ON	ON	No
	9	ON	OFF	ON	ON	ON	Yes
CST Discharging +AHU on	10	ON	ON	ON	OFF	ON	Yes
	11	OFF	ON	ON	ON	ON	No
	12	OFF	ON	ON	OFF	ON	Yes
	13	ON	ON	ON	ON	ON	Yes
	14	OFF	ON	ON	OFF	ON	No
	15	ON	ON	ON	OFF	ON	Yes

If the two-stage evaporator is active and additional capacity is required by means of thermal energy storage discharge, then a constant two stage evaporator load at its design capacity is aspired. For dynamic operation of the hydronic system, a system control is required that determines whether the thermal energy storage should be charged, remain inactive or be discharged, as well as whether the CO_2 heat pump should be operated. Therefore, a rule-based optimal control strategy is implemented, which was first proposed by Drees & Braun (1996) and was later on adapted within the 2015 ASHRAE Fundamentals Handbook by the American Society of Heating, Refrigerating and Air-Conditioning Engineers (2015). The proposed operation strategy is adapted to the system setup and assumes an off- and on-peak period during AC operation:

Generally, during the off-peak period, the thermal energy storage is charged, with the presumption that lower AC loads are present compared to the on-peak period. Figure 2 shows the general setup of the rule-based control system, which is adapted from the 2015 ASHRAE handbook control strategy (American Society of Heating, Refrigerating and Air-Conditioning Engineers, 2015). The charging of the ice tank is not represented as an operation mode since it is independent of the hydronic system, as Figure 1 shows.

If the time is within the on-peak period, Block 1 is activated. Block 1 asks whether the Energy-Cost-Ratio (ECR) is larger than the fraction of the COP during discharging (COP_d) and the COP during charging (COP_c). If the condition is true, Block 1 additionally requires that the current thermal energy storage can meet the predicted, accumulated demand $Q_{load,acc}$. C_s refers to the maximum thermal energy storage capacity and X to the state of charge of the TES. If the condition of Block 1, which is shown in Eq. (1) (American Society of Heating, Refrigerating and Air-Conditioning Engineers, 2015), is true, then Block 2 is activated, otherwise Block 3 is used.

$$ECR > \left(\frac{COP_d}{COP_c}\right) \ \&\& \ (X - X_{min}) \cdot C_s \ \geq Q_{load,acc} \tag{1}$$
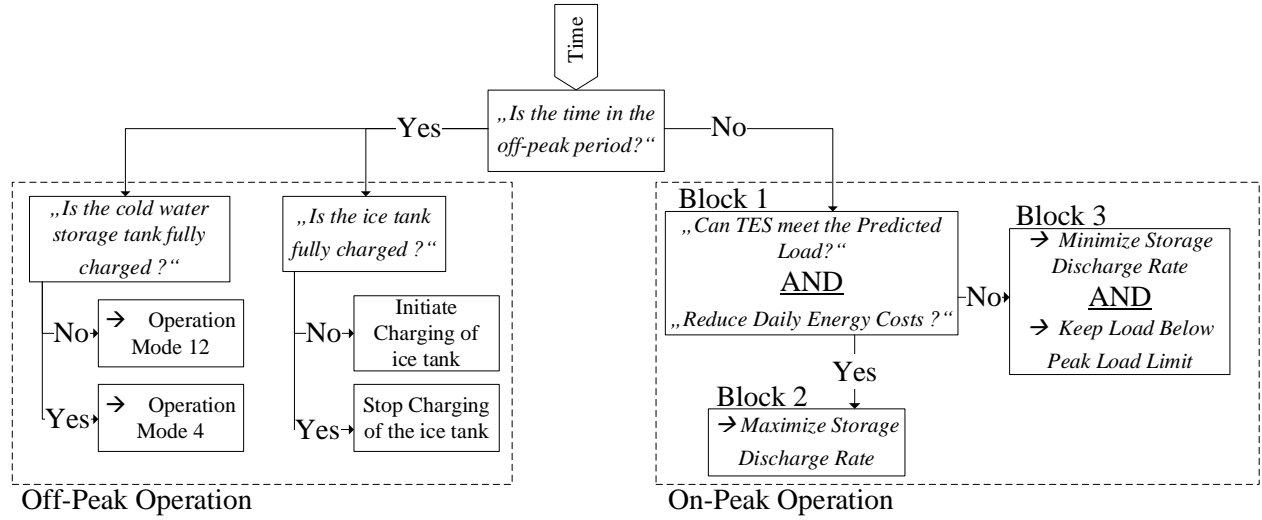
Figure 2: Adapted Rule-Based Control Strategy based on the American Society of Heating, Refrigerating and Air-Conditioning Engineers (2015)

Block 2 consists of the maximum use of storage and the CO_2 heat pump should remain off. Therefore, Block 2 contains the following operation modes: OM 8, OM 12, OM 14, OM 11. The operation modes are ordered in increasing capacity and are activated depending on the required capacity. An operation mode with higher capacity is chosen, if the moving average of the indoor temperature of the past seven minutes is larger than the indoor setpoint temperature. An operation mode with lower system capacity is chosen, if the component, which is currently controlling the air exit temperature of the air handling unit, is below 30 % of its operating range. The parameter is called downshift threshold value.

Block 3 minimizes the use of the thermal energy storage and operates the two-stage evaporator at full capacity, if required. In case that the capacity of the two-stage evaporator is not sufficient, the thermal energy storage is discharged. The following operation modes are therefore implemented within Block 3 and sorted after increasing system capacity: OM 7, OM 10, OM 15, OM 13. Their activation is dependent on the logic described in the previous paragraph. If the cold-water storage tanks run dry, OM 9 is activated.

Within Block 3 is the chilled water setpoint temperature leaving the TSEV calculated based on Eq. (2) - (4) by the American Society of Heating, Refrigerating and Air-Conditioning Engineers (2015).

$$\dot{Q}_{LLC} = max\left(\frac{Q_{load,occ} - (X - X_{min}) \cdot C_s}{\Delta t_{on}}, \dot{Q}_{ch,min}\right) \tag{2}$$

$$\dot{Q}_{ch} = min\left(\dot{Q}_{load}, max(\dot{Q}_{LLC}, \dot{Q}_{ch,peak})\right) \tag{3}$$

$$T_{chws} = max\left(T_{chwr} - \frac{\dot{Q}_{ch}}{c_{p,w} \cdot \dot{m}_{w,ch}}, T_{coil}\right) \tag{4}$$

$\dot{Q}_{LLC}$ marks the load limiting chiller load, $Q_{load,occ}$ the accumulated load within the on-peak period, Δt_{on} the time remaining in the on-peak period, C_s the thermal energy storage capacity, X the state of charge of the TES, $\dot{Q}_{ch,min}$ the minimum allowable chiller load, $\dot{Q}_{ch,peak}$ the maximum occurred peak load within a certain time period, $\dot{Q}_{load}$ the current chiller load, T_{chwr} the chilled water return temperature, $c_{p,w}$ the specific heat capacity of water, $\dot{m}_{w,ch}$ the chilled water mass flow and T_{coil} the temperature at the air handling unit.

The operation modes OM 2, 3, 5 & 6 are not intended to be used by the currently implemented control strategy. Since the ice tank is charging the CSTs within those OMs, it only makes sense to utilize these OMs if it is known that a large load will occur that cannot be solely handled by the ice tank, and a fast recharge of the CST is required. It is otherwise preferred to charge the CST through the TSEV due to the higher CO_2 evaporation temperature and therefore lower required compressor work.

3. MODELLING PROCEDURE

A model in the programming language Modelica was built utilizing the TIL-library. Additionally, the following sub-models are programmed to represent the individual components.

3.1. Ice Tank Sub-Model

The ice tank consists of vertical tubes running through a water tank, with evaporating CO_2 within the tubes. Due to the heat transfer between the CO_2 and water, ice formation and CO_2 evaporation occurs. The simplified ice tank model follows the following setup, as Figure 3 and Figure 4 shows.
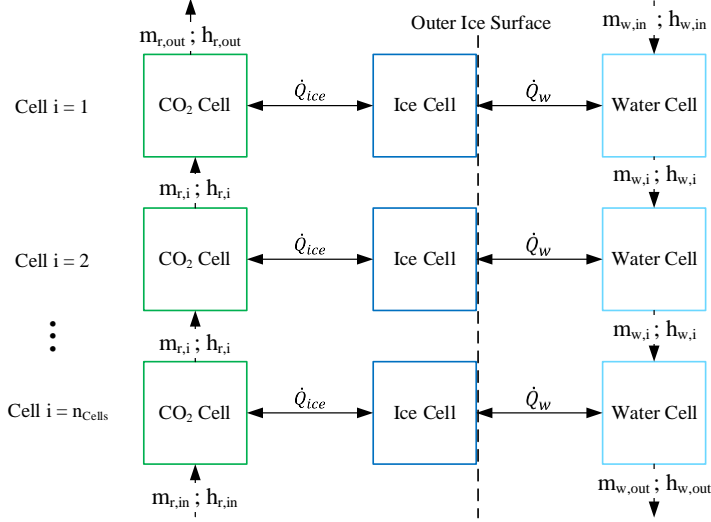
Figure 3: Ice Tank Cell Setup
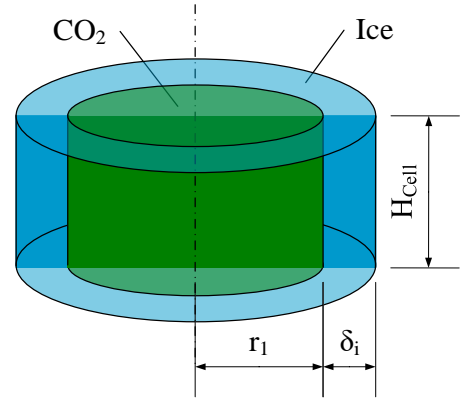
Figure 4: Ice Tank Pipe Detail

The simplified ice tank model discretizes the ice tank into horizontal cells. Within each horizontal cell is a CO_2, ice and water sub cell, which represents the entire fluid of each type within the horizontal cell. For dynamic simulations, the heat transfer is calculated to the outer ice surface, since the temperature on the ice surface is assumed to be $T_{ice,surface} = 0°C$. The following assumptions are made: The fluid flows and temperatures are assumed to be uniform within each sub-cell and the heat transfer coefficient α is constant. Furthermore, vertical conduction within the ice is neglected, as well as buoyancy forces within water and CO_2 due to density changes. The ice front of each pipe is assumed to not interfere with adjacent ice fronts, and the energy is stored as latent phase change energy solely. Furthermore, the thermal resistance of the tube is disregarded. The governing equations of the heat transfer calculation are calculated according to Eq. (5) - (8). $\alpha_{r,i}$ & $\alpha_{w,i}$ is the heat transfer coefficient that corresponds to the refrigerant and water, k_{ice} is the thermal conductivity and Δh_{fus} is the fusion enthalpy of water. n marks the total number, W_{tank} and D_{tank} the width and depth of the ice tank, and ρ_{ice} the density of ice. Eq. (5) & (6) are based on Incropera et al. (2017).

$$\dot{Q}_{w,i} = \alpha_{w,i} \cdot 2\pi \cdot ((r_1 + \delta_i)^2 - r_1^2) \cdot H_{cell} \cdot (T_{w,cell,i} - T_0) \tag{5}$$

$$\dot{Q}_{ice,i} = \frac{T_0 - T_{r,i}}{\dfrac{1}{2\pi \cdot r_1 \cdot H_{cell} \cdot \alpha_{r,i}} + \dfrac{\log\left(\dfrac{r_1 + \delta_i}{r_1}\right)}{2\pi \cdot k_{ice} \cdot H_{cell}}} \tag{6}$$

$$\dot{Q}_{st} = \dot{Q}_{w,i} - \dot{Q}_{ice,i} \tag{7}$$

$$\dot{Q}_{st} = \Delta h_{fus} \cdot \rho_{ice} \cdot \pi \cdot H_{cell} \cdot n_{tubes}((r_1 + \delta_i)^2 - r_1^2) \tag{8}$$

The state of charge of the ice tank is calculated based on the following Equation (9).

$$SOC_{IT} = \left(\sum_{i=1}^{n_{cells}} \frac{n_{tubes} \cdot \pi \cdot (\delta_i + r_1)^2 - n_{tubes} \cdot \pi \cdot r_1^2}{W_{tank} \cdot D_{tank} - n_{tubes} \cdot \pi \cdot r_1^2}\right)/n_{cells} \tag{9}$$

3.2. CO2 Heat Pump Sub-Model

The performance characteristics of the two-stage evaporator are approximated by a non-linear regression, which is based on data from experimentally verified simulations by Bengsch (2022) and contains 30 data points. The inlet and exit temperature of water $T_{TSEV,in}$ and $T_{TSEV,out}$ of the two-stage evaporator and the transferred heat $\dot{Q}_{TSEV}$ are used as predictor variables for the compressor work $\dot{W}_{comp}$. The gas cooler pressure p_{GC} is set to $p_{GC} = 120 \ bar$ within the simulations performed by Bengsch (2022). The non-linear regression is carried out in Matlab by using the in-built function *fitnlm*. The non-linear regression results in Equation (10), which predicts the compressor work with a root mean square error of $227 \ W$ and an adjusted R-value of $R = 0.99$.

$$\dot{W}_{MT,comp,1} = \frac{\dot{Q}_{TSEV}^{0.7988}}{\left(0.80206 \cdot T_{TSEV,in}^{-0.32896} - \left(-0.0012037 \cdot T_{TSEV,out}^{1.2483}\right)\right)} \tag{10}$$

The LT compressor model uses a constant isentropic efficiency of $\eta_{is} = 0.7$ and contains two limitations: The maximum allowable compressor work $\dot{W}_{comp,max}$ and the maximum swept volume $\dot{V}_{comp,max}$. A PI-controller sets the evaporation pressure such that the exit quality of the ice tank is $x = 1$. The set evaporation pressure is used to calculate the refrigerant mass flow based on the maximum compressor work $\dot{W}_{comp,max}$ and maximum swept volume $\dot{V}_{comp,max}$, as Equation (11) and (12) show respectively.

$$\dot{m}_{\dot{W}_{max}} = \frac{\dot{W}_{comp,max,LT} \cdot \eta_{is}}{(h_{2s} - h_1)} \tag{11}$$

$$\dot{m}_{lim,\dot{V}_{max}} = \dot{V}_{comp,max,LT} \cdot \rho(p_{evap}, h_{R,ice \ tank,out}) \tag{12}$$

If the mass flow calculated based on the maximum compressor work $\dot{m}_{\dot{W}_{max}}$ is larger than the mass flow calculated based on the maximum swept volume $\dot{m}_{lim,\dot{V}_{max}}$, then the maximum swept volume limits higher mass flow rates and $\dot{m}_{lim,\dot{V}_{max}}$ is set as the refrigerant mass flow. Otherwise, $\dot{m}_{\dot{W}_{max}}$ is set as the refrigerant mass flow. The compressor work $\dot{W}_{comp,LT}$ is calculated based on Equation (13) under the assumption that the discharge pressure is constant at $p_{dis,LT \ comp} = 39 \ bar$. Indices 1 refers the suction port and 2 to the discharge port of the compressor. Equation (13) is used as well to model the compression from the liquid receiver to the gas cooler pressure by the MT compressors. It is assumed that CO_2 enters the MT compressor with a superheat of $\Delta T_{SH} = 5 \ K$ at $p_{suc,MT \ comp} = p_{dis,LT \ comp} = 39 \ bar$ with an isentropic efficiency of $\eta_{is} = 0.7$. Hence, the total MT compressor work is calculated by Equation (*14*).

$$\dot{W}_{comp} = \dot{m}_r \cdot \frac{h_{2s} - h_1}{\eta_{is}} \tag{13}$$

$$\dot{W}_{comp,MT} = \dot{W}_{MT,comp,1} + \dot{m}_{r,ice \ tank} \cdot \frac{h_{2s}(p = 120 \ bar, s = s_1) - h_1(p = 39 \ bar, \Delta T_{SH} = 5 \ K)}{\eta_{is}} \tag{14}$$

3.3. Cold Water Storage Tanks Sub-Model

The cold-water storage tanks are approximated by the TIL-library class "Tube". Hence, the cold-water storage tank model does not consider heat leakage due to heat conduction through the tank walls and buoyancy forces within the water due to density differences. Due to the "Tube" class, the inlet and exit ports are located at the top/ bottom of the tank and thereby no dead volume is present. The operating range of the cold-water storage tanks is set between $T_{CST} = 4 - 12 \ °C$. Furthermore, the state of charge is calculated based on the following Equation (15):

$$SOC_{CST} = \frac{\sum_{i=1}^{n_{cells,CST}} m_i \cdot c_{p,w} * (12 \ °C - T_i)}{m_{tank} \cdot c_{p,w} \cdot (12 \ °C - 4 \ °C)} \tag{15}$$

3.4. Control Volume Sub-Model

One air volume is set within the simulation to represent the air volume of e.g. HVAC applications with several rooms. Hence, the AC load is posed onto the control volume and air is circulated from the control volume through the air handling unit by a fan. An air boundary keeps the control volume at constant atmospheric pressure. The fan control is set to maintain a constant control volume temperature of $T_{room} = 22 \ °C$.

4. SIMULATION

The following Table 2 shows the key parameters utilized within the simulation. The simulation is carried out as a dynamic 24-h simulation. It is assumed that the ECR is always lower than COP_d/COP_c and thereby, the operation strategy is only dependent on the remaining thermal energy storage capacity. Details of the parameters are presented in the publication by Köster (2023).

Table 2: Selected Simulation Parameters

Two Stage Evaporator & Pump	LT Compressor	Ice Tank
$\dot{Q}_{TSEV,design} = 20\ kW$	$\dot{V}_{LT,comp,max} = 0.005\ m^3/s$	$\alpha_{CO_2} = 8000\ W/m^2K$
$\dot{m}_{main\ pump} = 4\ kg/s$	$\dot{W}_{LT,comp.max} = 9\ kW$	$\alpha_w = 500\ W/m^2K$
$\dot{m}_{ice\ tank\ pump} = 3\ kg/s$	$\eta_{is} = 0.7$	$h_{R,in} = 210.7\ kJ/kgK$
$T_{air,exit,AHU} = 9°C$		$d_{tube} = 0.04\ m$
		$W_{tank} = D_{tank} = 2.5\ m$
		$H_{tank} = 1\ m$
		$n_{tubes} = 625$
		$n_{cells} = 5$
Cold Water Storage Tanks	**Air Handling Unit**	**Valves & More**
$n_{Cells} = 30$	Fin and Tube Heat Exchanger	$A_{cross\ section\ valves} = 1\ m^2$
$V_{tank} = 6.1\ m^3$	$\alpha_{air} = 65\ W/m^2K$	$t_{on-peak\ period} = 8 - 23h$
$D_{tank} = 1\ m$	$\alpha_w = 1000\ W/m^2K$	
	$T_{room,setpoint} = 22\ °C$	
	$\dot{V}_{fan,max} = 4\ m^3/s$	
	$l_{finned\ tube} = 3\ m$	
	$n_{serial\ tubes} = 20$	
	$\Delta l_{serial\ tubes} = 0.022\ m$	

5. RESULTS AND DISCUSSION

Within the presented results in Figure 5 and Figure 6, the off-peak period is marked in white, the minimal use of storage period with active two stage evaporator is marked in light grey and the maximum use of storage period is marked in dark grey. The first subplot of Figure 5 shows the AC load on the control volume over the 24-h period with the AC load during the on-peak being above $\dot{Q}_{AC} = 20\ kW$. The AC load peaks at $t = 16\ h$ with $\dot{Q}_{AC} = 60.1\ kW$.

5.1. Off-peak Period/ Thermal Energy Storage Charging

During the off-peak period, the cold water storage tank is initially charged, which can be seen in the third subplot of Figure 5, since $OM = 4$ (second subplot of Figure 5) and the state of charge of the cold storage tanks SOC_{CST} is increasing. Once the cold-water storage tanks are fully charged, the operation mode is switched to $OM = 12$, which corresponds to covering the load of the air handling unit by the cold water storage tanks. This is intended, as it is believed to be beneficial to not operate the heat pump at low part loads, but to charge the cold storage tanks with the design evaporator capacity and then cover the AC load solely by the CST discharge. The control volume temperature levels off towards the setpoint, as the fourth subplot of Figure 5 shows.

Within the off-peak period, the ice tank is continuously charged (third subplot of Figure 5, SOC_{IT}) with a near constant LT compressor work of $\dot{W}_{LT,comp} \approx 9\ kW$, as the first subplot of Figure 6 shows. The decrease in LT compressor work $\dot{W}_{comp,LT}$ at $t = 0.79 - 1.91\ h$ is due to the set limitation of the maximum volume flow rate $\dot{V}_{comp,LT,max}$. At the end of the off-peak period, the ice tank is fully charged.

As the third subplot of Figure 6 shows, the load on the two stage evaporator is closely regulated to the setpoint load of $\dot{Q}_{TSEV,setpoint} = 20\ kW$ and it can be concluded that the pump regulation to obtain the setpoint load on the two stage evaporator during charging is working accordingly. The calculated MT compressor work $\dot{W}_{comp,MT}$ is dependent, as presented in Equation (14), on the TSEV load $\dot{Q}_{TSEV}$ and the

refrigerant mass flow through the ice tank $\dot{m}_{r,ice\ tank}$. The MT compressor work peaks at a local maximum of $W_{comp,MT} = 29.98\ kW$ at $t = 1.72\ h$, since the initialization pressure of the ice tank is set to $p_{r,IT,init} = 20\ bar$ and the PI controller increases the evaporation pressure initially to reach the setpoint condition of $x = 1$. Hence, higher evaporation pressures lead to higher mass flow rates and therefore to a peak in the MT compressor work.
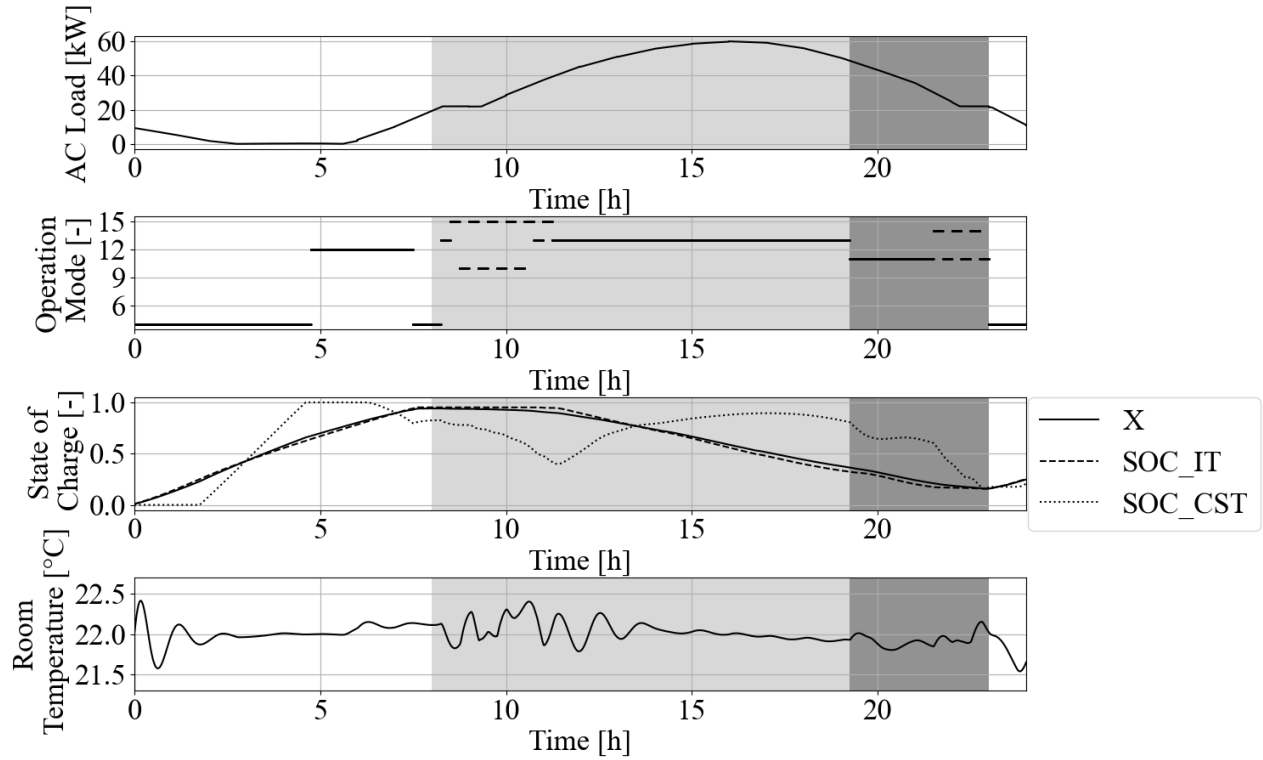
Figure 5: Key Performance Indicators of the System 1/2
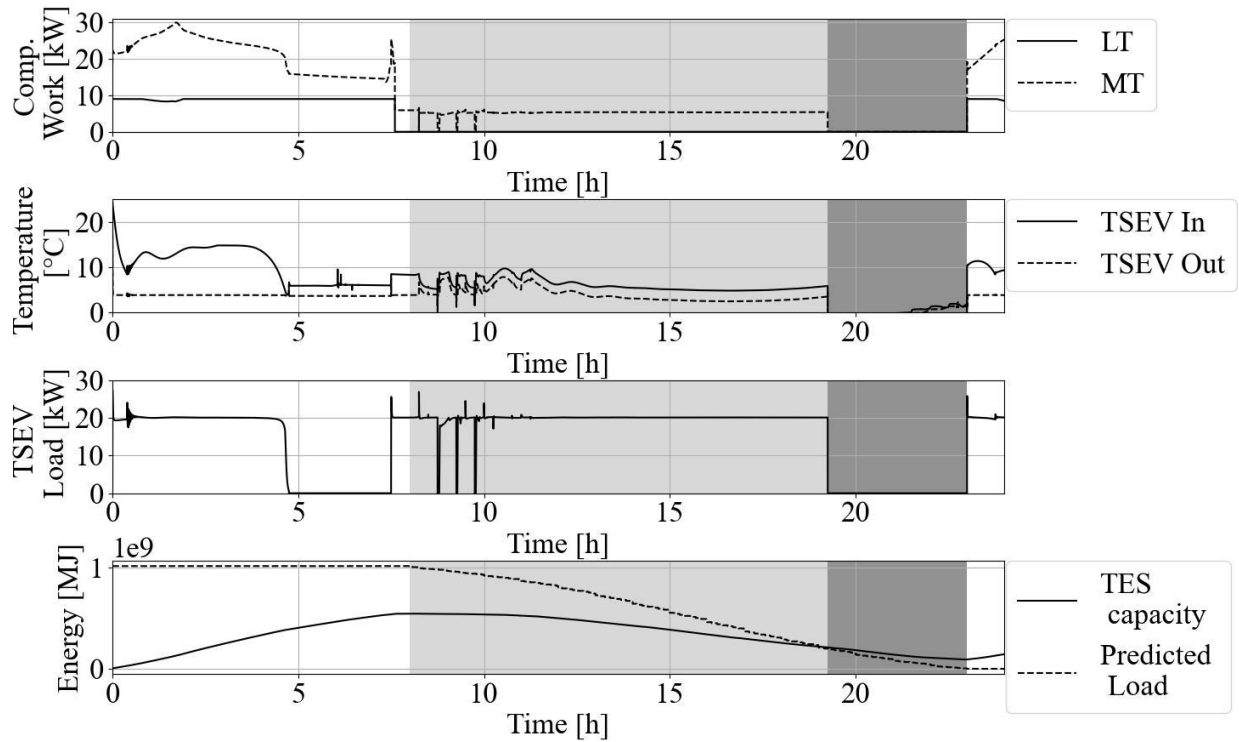
Figure 6: Key Performance Indicators of the System 2/2

5.2. On-peak Period/ Thermal Energy Storage Discharging – Minimal Use of Storage Period

During the on peak period, where the thermal energy storage utilization is minimised and the operation of the two stage evaporator is maximised, the operation modes show initially fluctuations between OM = 15, 13, 10 between AC loads of $\dot{Q}_{AC} = 20 - 40\ kW$ (Figure 5 second subplot). This indicates that the capacity gap between those OM's is too large or the downshift threshold value is set too high. These fluctuations evoke fluctuations in the TSEV load $\dot{Q}_{TSEV}$. Hence, further investigations with a lower downshift threshold value are required to assess the impact of on system stability. Besides the fluctuation in the operation mode, which lead to smaller room temperature fluctuations (see fourth subplot of Figure 5), the room temperature is kept within $\pm 0.5\ K$ of its setpoint. A remarkable trend can be seen during the beginning of OM = 11, since the SOC_{CST} increases (see Figure 5 third subplot), even though the cold-water storage tanks are discharged. The second subplot of Figure 6 provides further insights, since the temperature of return water to the tanks, which equals the two stage evaporator inlet temperature, is lower than 12 °C, and therefore, the tank charges or keeps the SOC_{CST} constant. This unintentional recharge of the CST is due to the low setpoint of the air exit temperature of the AHU. Besides the previously mentioned fluctuations, the TSEV operates approximately constant at its design capacity of $Q_{TSEV,design} = 20\ kW$ within this period, which results in a slightly decreasing MT compressor work of $\dot{W}_{comp,MT} = 5.9 - 5.3\ kW$.

The fourth subplot of Figure 6 shows the thermal energy storage capacity and the predicted AC load over the 24-h period. Once the thermal energy storage can cover the predicted remaining AC load, the operation strategy changes from min. use of thermal energy storage to max. use of thermal energy storage and deactivates the two-stage evaporator, which indicates a correct implementation of the control strategy.

5.3. On-peak Period/ Thermal Energy Storage Discharging – Maximal Use of Storage Period

Within the maximal use of storage period, which is marked in dark grey in Figure 5 and Figure 6, the heat pump system remains deactivated and the AC load is covered by the thermal energy storage. The operation of OM = 11 initially increases the SOC_{CST} and keeps it in the beginning on an approximately constant level. The effect is due to the already discussed low return water temperature to the cold-water storage tanks. Both OM = 11 and OM = 14 achieve to keep the room temperature within $\pm 0.5\ K$ of its setpoint.

At the end of the on-peak period, the remaining charge in the cold storage tanks is $SOC_{CST} = 0.18$ and the ice tank $SOC_{IT} = 0.15$. The SOC_{IT} should be ideally $SOC_{IT} = 0$ at the end of the on-peak period, since the ice layer forms an isolation layer around the tubes, which requires lower evaporation temperatures and thereby higher compressor loads. The remaining state of charge of the system X can have several reasons. For one, Köster (2023) reported an energy deviation between the stored energy of the ice tank and the energy transferred to the fluid stream of up to 7 %. Furthermore, the unintentional recharge of the cold-water storage tanks influences the remaining thermal energy storage capacity. Another influence could be an inaccurate load prediction. For further simulations, investigations should be carried out in the above-mentioned fields to eliminate the inaccuracy.

5.4. General Observations and Critical Remarks

By the implementation of the thermal energy storage into the hydronic system, the AC load can be shifted towards off-peak hours. The current simulation setup achieves to shift 65 % of the on-peak load to be covered during the off-peak period. Furthermore, the peak load on the two-stage evaporator is limited since it almost constantly operates at $\dot{Q}_{TSEV} = 20\ kW$ while in operation. Under the presumption of dynamic electricity pricing with lower electricity charges at night, the electricity costs could potentially be decreased. Due to the load limitation and regulation of the two-stage evaporator, a parallel MT compressor setup could be implemented, with one compressor operating at its design point for covering the two-stage evaporator load and an additional compressor to cover the higher TES charging demands. Hence, part load operation of the heat pump system would be reduced.

However, the gained results from this study only serve as a proof of concept considering the made assumptions. Especially, the entire CO_2 heat pump, including the two-stage evaporator model, should be implemented within Modelica, to represent a physical system with the system characteristics, inertia and regulation. Additionally, the ice tank requires, as well as the load prediction, further investigations to ensure the accuracy of the gained results. Hence, by defining a real-life application of the system within e.g. production facilities, hotels, etc. a more thorough analysis could be carried out. The analysis should include an economical evaluation to compare the increased investment costs against the cost savings that can be achieved.

6. CONCLUSION

The present study investigates a system proposal utilizing an advanced CO2 heat pump setup with a hydronic subsystem to cover an exemplary air conditioning demand. The CO2 heat pump consists of a two-stage evaporator configuration with one stage operating using the thermosyphon principle and the second stage being driven by the suction port of the ejector. The hydronic subsystem connects the two-stage evaporator to the air handling unit and implements a thermal energy storage by means of an ice tank and a cold-water storage tank. The hydronic system configuration allows great flexibility during operation to adapt to the corresponding demand. A rule-based optimal control strategy is implemented, which differentiates between off- and on-peak period and initiates charging and discharging of the thermal energy storage.

The proposed system configuration was able to maintain a room temperature at $T_{room} = 22°C \pm 0.5K$ during the simulated 24-h period. It was furthermore achieved that 65 % of the required on-peak load could be covered by the thermal energy storage, which was charged during the off-peak period. The implementation of the thermal energy storage is able to achieve load shifting and peak load limiting, which creates the basis for cost savings due to dynamic energy prices. The result from the study should be seen as a proof of concept and requires further investigations, such as a case study for a use-case scenario combined with an economical evaluation.

7. NOMENCLATURE

Abbreviations:

$COP_{c/d}$	Coefficient of performance during charging and discharging of the TES [-]
DHW	Domestic Hot Water
ECR	Energy-Cost-Ratio
HVAC	Heating, Ventilation and Air Conditioning
HX	Heat Exchanger
LT/ MT	Low Temperature / Medium Temperature
SOC	State of Charge
TES	Thermal Energy Storage
TSEV	Two-Stage Evaporator

Latin Letters:

C_s	Thermal Energy Storage Capacity [kJ]
$\dot{Q}$	Transferred Heat [kW]
T	Temperature [°C]

8. REFERENCES

American Society of Heating, Refrigerating and Air-Conditioning Engineers. (2015). *2015 ASHRAE Handbook: Heating, Ventilating, and Air-conditioning Applications* (I-P edition). ASHRAE 2015.

Bengsch, J. (2022). *Investigation and analysis of a CO2 heat pump chiller with novel two- stage evaporator* [Master Thesis]. https://ntnuopen.ntnu.no/ntnu-xmlui/handle/11250/3030759

Dong, Y., Coleman, M., & Miller, S. A. (2021). Greenhouse Gas Emissions from Air Conditioning and Refrigeration Service Expansion in Developing Countries. *Annual Review of Environment and Resources*, *46*(1), 59–83. https://doi.org/10.1146/annurev-environ-012220-034103

Drees, K., & Braun, J. (1996). Development and Evaluation of a Rule-Based Control Strategy for Ice Storage Systems. *HVAC&R Research*, *2*(4), 312–334. https://doi.org/10.1080/10789669.1996.10391352

Incropera, F. P., Bergman, D. P., Theodore, L., & Adrienne, S. (2017). *Fundamentals of heat and mass transfer* (Global Edition). John Wiley & Sons Inc.

Köster, L. (2023). *Application of a Novel Two Stage Evaporator within (H)VAC Applications*. NTNU.

Pörtner, H.-O., Roberts, D. C., Poloczanska, E. S., Mintenbeck, K., Tignor, M., Alegria, A., Craig, M., Langsdorf, S., Löschke, S., Möller, V., & Okem, A. (2022). Summary for Policymakers. *Climate Change 2022: Impacts, Adaptation, and Vulnerability. Contribution of Working Group II to the Sixth Assessment Report of the Intergovernmental Panel on Climate Change*, 3–33. https://doi.org/10.1017/9781009325844.001